Department of Physics and Astronomy
University of Heidelberg

Diploma thesis
in Physics

submitted by
Daniel Kiefhaber
born in Kaiserslautern

2010

Development of a Reflective Stereo Slope Gauge for the Measurement of Ocean Surface Wave Slope Statistics

This diploma thesis has been carried out by Daniel Kiefhaber
at the
Institute of Environmental Physics
under the supervision of

Prof. Dr. Bernd Jähne
and
Prof. Dr. Ulrich Platt

Abstract

An optical instrument for the measurement of surface ocean wave statistics has been developed and is presented in this thesis. Based on the *reflective stereo slope gauge* (RSSG) principle, it can simultaneously measure wave slope and height statistics. The instrument comprises a stereo camera setup and two light sources built from infrared LEDs (940 nm). Slope statistics are derived from the statistical distribution of the positions of specular reflections in images of the water surface. The parallax of the reflections in the stereo images gives the distance of the camera to the water surface which can be used to infer wave height statistics. A laboratory version of the instrument has been built, calibrated and tested in experiments at the Aeolotron wind wave facility. Two-dimensional slope probability distributions for slopes in the range of $-0.05 < s_{\mathrm{x,y}} < 0.05$ were obtained for a range of wind speeds and clean water as well as surface slick conditions. The mean square slope of the surface was derived and compared to data from simultaneous reference measurements. The two data sets are found to agree well for lower wind speeds, at higher wind speeds significant deviations occur. The causes for these deviations have been identified and taken into account in designing the instrument for field measurements. This ocean version of the instrument is ready to accompany heat exchange measurements aboard a research vessel in the Baltic Sea in June 2010.

Zusammenfassung

Ein optisches Instrument zur Messung von Wellenstatistiken von Ozean-Oberflächenwellen wurde entwickelt und wird in dieser Arbeit präsentiert. Es basiert auf dem *reflective stereo slope gauge* (RSSG) Prinzip und kann gleichzeitig die Statistik von Wellenneigungen und Wellenhöhen messen. Das Instrument umfasst ein Stereo-Kamera-System und zwei Lichtquellen, die aus Infrarot-LEDs (940 nm) aufgebaut sind. Neigungsstatistiken werden aus der statistischen Verteilung der Positionen von spiegelnden Reflexen in Bildern der Wasseroberfläche gewonnen. Die Parallaxe der Reflexe in den Stereo-Bildern ergibt die Entfernung der Kamera zur Wasseroberfläche, aus welcher auf Wellenhöhenstatistiken zurückgeschlossen werden kann. Eine Laborversion des Instruments wurde aufgebaut, kalibriert und in Experimenten am Aeolotron Wind-Wellen-Kanal getestet. Zweidimensionale Neigungsverteilungen wurden sowohl für sauberes Wasser, als auch unter Oberflächenfilm-Bedingungen für verschiedene Windgeschwindigkeiten in einem Neigungsbereich $-0.05 < s_{\mathrm{x,y}} < 0.05$ bestimmt. Die mittlere quadratische Neigung der Oberfläche wurde aus den Verteilungen abgeleitet und mit Daten aus simultanen Referenzmessungen verglichen. Die beiden Datensätze stimmen bei niedrigen Windgeschwindigkeiten gut überein, bei höheren Windgeschwindigkeiten treten signifikante Abweichungen auf. Die Gründe für diese Abweichungen wurden identifiziert und im Design des Instruments für Feldmessungen berücksichtigt. Diese Ozeanversion des Instruments steht bereit um im Juni 2010 Wärmeaustauschmessungen an Bord eines Forschungsschiffs in der Ostsee zu begleiten.

Contents

1 Introduction

More than two thirds of the surface of the Earth are covered with bodies of water. They play a prominent role in the global climate system, e.g. by solving and storing huge amounts of greenhouse gases, like CO_2. The fraction of fossil fuel CO_2 that is taken up by the oceans is estimated to be 30-40 % (Donelan and Wanninkhof, 2002; Sabine et al., 2004). Over longer, millenial timescales, the oceans are expected to eventually dissolve about 85 % of the anthropogenic CO_2 released into the atmosphere (Field and Raupach, 2004). Global climate models which are important tools to make predictions about future climate development need to account for this. Thus it is necessary to know how the greenhouse gases that are added to the atmosphere by burning of fossil fuel are dissolved in the oceans and which factors the transport rates depend on.

Although the oceans are a net sink for CO_2 in the global carbon cycle, figure 1.1 indicates that the situation is more complex. CO_2 transport between atmosphere and oceans is not unidirectional and shows high spatial variability on global scales. The situation becomes even more complicated when transfer is investigated on much smaller scales. The gas flux depends on many factors, such as concentration gradients, wind, air and sea temperature, surfactant coverage etc. Figure 1.2 illustrates the variety of interactions between the atmosphere and the oceans. Most of them are interconnected and many contribute to some extent to air-sea gas exchange rates (Wanninkhof et al., 2009).

The "bottleneck" for the transport of trace gases like CO_2, but also for heat, from the atmosphere to the ocean is the interface between air and sea. While the near surface atmosphere is well mixed by wind-induced turbulence, the turbulence cannot cross the gas-liquid phase boundary (Jähne, 1985). In the so-called aqueous boundary layer which has a thickness of 20 to 2000 micrometers, transport can only occur by the relatively slow molecular diffusion (Jähne, 2010). The exact processes that determine the rates of gas and heat transfer at the air-sea boundary are a topic of ongoing research. It is, however, well established that gas exchange rates are heavily dependent on surface roughness – constituted by waves (Jähne et al., 1987).

The ocean surface is practically never completely calm and flat. Even in the absence of wind – the generating and driving force behind most waves – one can usually observe a long wavelength swell, possibly coming from storms thousands of kilometers away. A remarkable feature of ocean waves is the huge spectrum of wavelengths that occur (see figure 1.3). From small so-called capillary waves with wavelengths of millimeters to centimeters, to the short

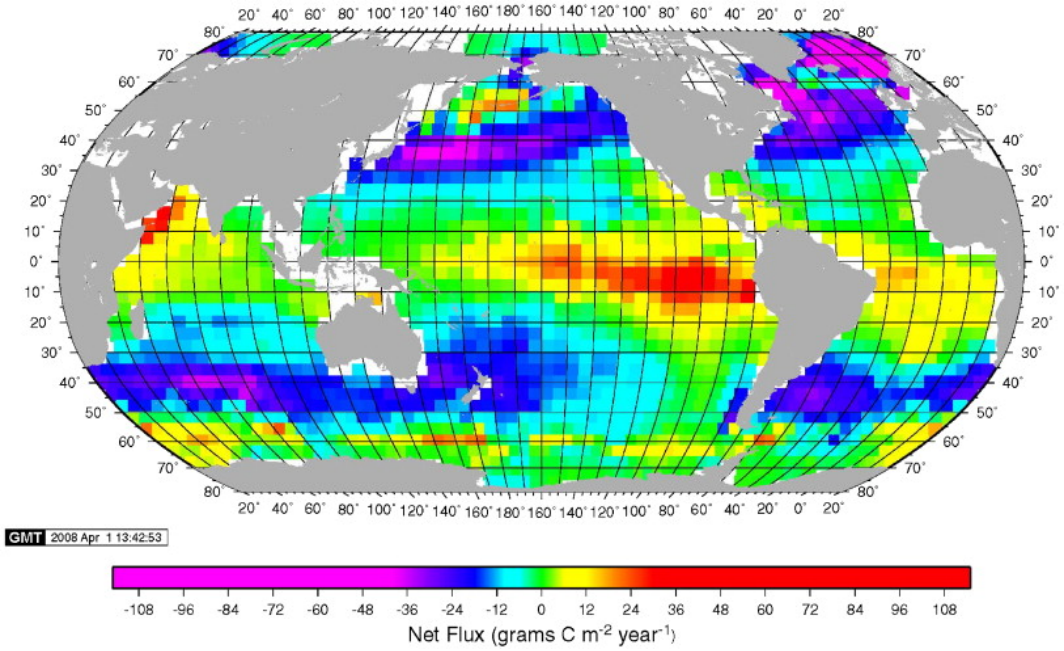

Figure 1.1: The oceans as a sink for CO_2: The map shows the spatial distribution of the mean annual net flux of CO_2 between the atmosphere and the ocean (year 2000). It is based on 3 million surface water measurements of CO_2 concentration. The resulting net global air-sea flux is $1.42 \cdot 10^{12}$ kg of Carbon per year. (Taken from Takahashi et al. (2009).)

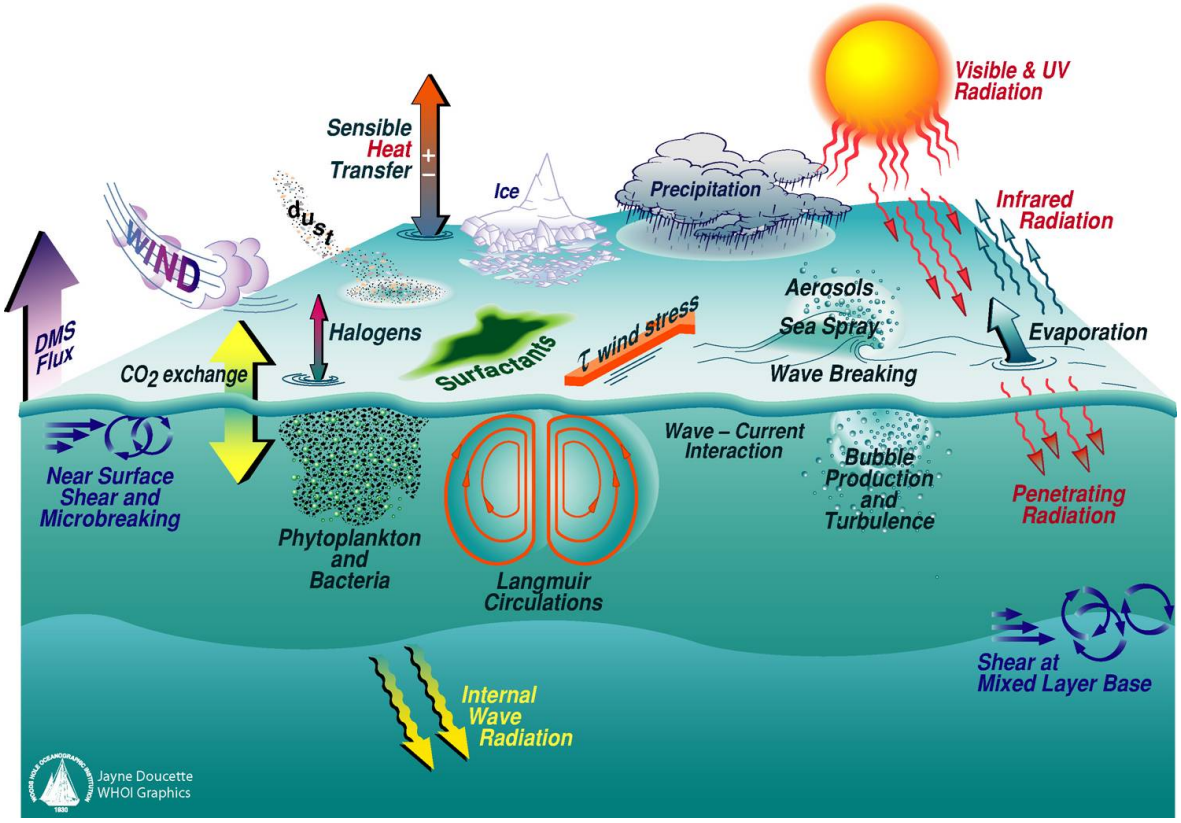

Figure 1.2: Interactions between the lower atmosphere and the upper oceans. Source: SOLAS International Project Office (http://www.solas-int.org/resources/downloads.html).

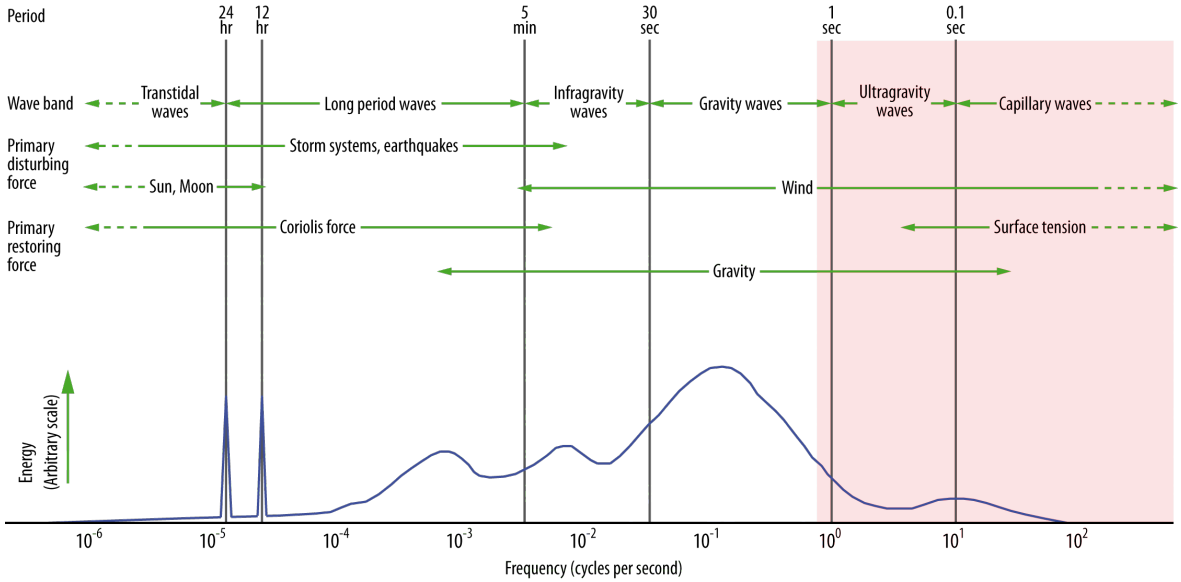

Figure 1.3: Schematic represenation of the energy contained in the surface waves of the oceans. The red box indicates the part of the spectrum this work is concerned with. Redrawn and modified after Kinsman (1965).

gravity waves that appear shortly after the onset of wind, with wavelengths in the order of decimeters to meters, to long swell with wavelengths of tens and hundreds of meters. The spectrum is extended even further if tides and tsunamis are included. The latter are generated not by wind but by submarine earthquakes and can practically not be observed on the open ocean, because their wavelengths are in the order of hundreds of kilometers while their amplitudes are mere centimeters.

While tsunamis and longer gravity waves may be dominant in the public perception of ocean waves, they are not as relevant to gas exchange. Two effects contribute to the enhancement of gas exchange: First, the total surface area is increased in the presence of waves, and second, breaking waves create turbulence and bring water from deeper layers to the surface. The increase in surface area is only 5 % for a relatively rough surface with a mean square slope of 0.1 (Cox and Munk, 1956). Turbulence induced by breaking waves is far more important and can triple gas transfer rates (Jähne et al., 1979). Not all breaking waves are producing spectacular whitecaps. Short waves can introduce turbulence in the boundary layer by so-called microscale wave breaking (Banner and Phillips, 1974). Since diffusion through the boundary layer is very slow, turbulence that renews the surface with fresh and unsaturated water from below strongly accelerates gas exchange (Zappa et al., 2001).

The wave field in the open ocean is not fully described by the local wind speed. For example, it can be significantly altered in the presence of surfactants. These surfactants may be anthropogenic, e.g. oil, but can just as well be biological, e.g. produced by phytoplankton. Surfactants effectively dampen capillary and short gravity waves and thus reduce the overall effect of wind stress on the water surface significantly. What is striking is that a mono molec-

ular layer of a surfactant can be sufficient to produce observable effects (Hühnerfuss et al., 1987; Jähne et al., 1987).

Gas exchange experiments are conducted both on the open ocean and in laboratory facilities. Laboratory facilities allow experiments to investigate dependencies on single environmental parameters that can be controlled in a closed facility (Jähne, 1980). On the other hand, since it is not trivial to scale all oceanic processes to laboratory size, field experiments are indispensable.

The goal of this work is the development of an improved measurement instrument to measure certain properties of surface waves in the field, i.e. on the open ocean. This instrument, the *Reflective Stereo Slope Gauge* (RSSG), will be installed on research vessels and able to measure statistics of the height and slope distribution of waves. In earlier realizations of the measurement principle, Waas and Jähne (1992) and Dieter (1998) showed that the RSSG can successfully measure wave height and slope statistics in the field. However, the technological development of the time limited the performance of the instrument. The new RSSG can measure partial slope probability distributions and derive slope and height statistics with unprecedented resolution. Statistical parameters that can be determined include the *mean square slope*, the variance of the slope probability distribution, which can be used to parameterize the influence of surface roughness on gas transfer rates (Jähne et al., 1987).

2 Theory

2.1 Fluid Mechanics Basics

2.1.1 Reference Frames

In fluid mechanics, two reference frames are commonly used and have been given special names. A *Eulerian reference frame* is at rest (with respect to the earth) and the velocity of the fluid is described by the vector field $\mathbf{u}(\mathbf{x}, t)$. In this specification, the rate of change of a given property[1]

$$\frac{D}{Dt} \equiv \frac{\partial}{\partial t} + \frac{\partial}{\partial x_j}\frac{\partial x_j}{\partial t} = \frac{\partial}{\partial t} + u_j \frac{\partial}{\partial x_j} = \frac{\partial}{\partial t} + \mathbf{u} \cdot \boldsymbol{\nabla}, \tag{2.1}$$

where the last conversion is only valid in Cartesian coordinates.

The total rate of change is composed of the local rate of change $\frac{\partial}{\partial t}$ and the advective rate of change $\mathbf{u} \cdot \boldsymbol{\nabla}$. The *material derivative* operator $\frac{D}{Dt}$ which is popularly used in fluid mechanics is fully equivalent to the $\frac{d}{dt}$ operator from elementary calculus. It is used to highlight the physical interpretation of local and advective change.

A *Lagrangian reference frame* is not at rest, but moving with the fluid's velocity $\mathbf{u}$. Here, the material derivative reduces to the (partial) time derivative

$$\frac{D}{Dt} \equiv \frac{\partial}{\partial t}, \tag{2.2}$$

since the velocity of the fluid relative to the reference frame is zero and there cannot be advection.

In laboratory studies of fluid mechanics, instruments are usually fixed to, say, wind-wave facilities, and thus measure fluid properties in a Eulerian reference frame. In open ocean experiments, drifting buoys can be deployed to follow the mean water flow and thus measure in a Lagrangian reference frame, while ship-borne measurements can also be conducted from a Eulerian frame, since GPS-based navigation permits holding a position accurately.

[1] Einstein's tensor summation convention notation is used.

2.1.2 Navier-Stokes Equation

Newton's second axiom – or law of motion – states that any force applied to a body produces a proportional acceleration, the constant of proportionality being the mass m. This law can be applied not only to point-like bodies, but also to a continuum, such as a body of water. There are four forces acting on water in the ocean, arising from pressure, gravitation, the Coriolis effect (i.e. the Earth's rotation), and friction. The acceleration $\mathbf{a}$ can therefore be written as the vector sum

$$\mathbf{a} = \mathbf{p} + \mathbf{g} + \mathbf{c} + \mathbf{m}\,, \tag{2.3}$$

where $\mathbf{p}$, $\mathbf{g}$, $\mathbf{c}$, and $\mathbf{m}$ are the pressure, gravitational, Coriolis, and frictional forces per unit mass, respectively. Since acceleration is the rate of change of velocity

$$\frac{D\mathbf{u}}{Dt} = \mathbf{p} + \mathbf{g} + \mathbf{c} + \mathbf{m}\,. \tag{2.4}$$

The fundamental equation of motion for fluids is the Navier-Stokes equation, which describes the forces acting on a unit volume of a fluid. For incompressible fluids ($\frac{\mathrm{d}\rho}{\mathrm{d}t} = 0$), it is obtained from (2.4) by multiplication with the fluid density ρ. In the special case of interest, i.e. oceanic surface wind waves, the Coriolis force can be neglected[2] and the Navier-Stokes equation reduces to

$$\rho\frac{D\mathbf{u}}{Dt} = \rho\,(\mathbf{p} + \mathbf{g} + \mathbf{m}\,) = -\boldsymbol{\nabla} p + \rho\mathbf{g} + \mu\nabla^2\mathbf{u}\,, \tag{2.5}$$

with the dynamic viscosity μ.

2.1.3 Potential Flow

Expanding the material derivative on left hand side of the Navier-Stokes equation (2.5) gives

$$\rho\frac{D\mathbf{u}}{Dt} = \rho\frac{\partial\mathbf{u}}{\partial t} + \rho(\mathbf{u}\cdot\boldsymbol{\nabla})\mathbf{u}. \tag{2.6}$$

Due to the nonlinear term $(\mathbf{u}\cdot\boldsymbol{\nabla})\mathbf{u}$, a general analytical solution to the Navier-Stokes equation, is not known. However, a number of special solutions exist and in many cases the equation can be linearized without introducing unreasonable error.

Using the vector identity

$$(\mathbf{u}\cdot\boldsymbol{\nabla})\mathbf{u} = (\boldsymbol{\nabla}\times\mathbf{u})\times\mathbf{u} + \frac{1}{2}\boldsymbol{\nabla}u^2 \tag{2.7}$$

and the definition of the vorticity $\boldsymbol{\omega} \equiv \boldsymbol{\nabla}\times\mathbf{u}$, the Navier-Stokes equation can then be rewritten as

$$\rho\frac{\partial\mathbf{u}}{\partial t} + \rho(\boldsymbol{\omega}\times\mathbf{u}) + \rho\frac{1}{2}(\nabla u^2) = -\boldsymbol{\nabla} p + \rho\mathbf{g} + \mu\nabla^2\mathbf{u}\,. \tag{2.8}$$

[2] This approximation holds as long as the frequencies of the considered motions are large compared to the Earth's angular frequency (see e.g. Kinsman, 1965).

As a consequence of *Kelvin's circulation theorem* (Kundu, 2007), an inviscid flow, upon which only conservative body forces act, remains irrotational if it was at some point irrotational. This applies to surface waves that were generated from rest. However, the circulation theorem requires that the last term in (2.8) vanishes. The effects of the small viscosity of water are confined to boundary layers and do not affect the propagation of waves significantly (Kundu, 2007).

For irrotational or *potential flow* with $\boldsymbol{\omega} = 0$, the fluid's motion is conservative, allowing for the definition of a velocity potential Φ in such a way that

$$\mathbf{u} \equiv \boldsymbol{\nabla}\Phi. \tag{2.9}$$

2.1.4 Bernoulli Equation

Although historically Bernoulli formulated his famous equation before the Navier-Stokes equation was found, it can be derived from the latter or, more precisely, from the Euler equation, which is the formulation for inviscid fluids. Dividing (2.8) by ρ, dropping the viscosity term and rearranging the others, substituting $\mathbf{g} = -\boldsymbol{\nabla}(gz)$,

$$\frac{\partial \mathbf{u}}{\partial t} + \boldsymbol{\nabla}(\frac{1}{2}u^2) + \frac{\boldsymbol{\nabla} p}{\rho} + \boldsymbol{\nabla}(gz) = -(\boldsymbol{\omega} \times \mathbf{u})\,. \tag{2.10}$$

For barotropic flow, where the fluid's density is a function of pressure only ($\rho = \rho(p)$),

$$\frac{1}{\rho}\boldsymbol{\nabla} p = \boldsymbol{\nabla} \int \frac{dp}{\rho} \tag{2.11}$$

and thus the Euler equation can be condensed to

$$\frac{\partial \mathbf{u}}{\partial t} + \boldsymbol{\nabla}\left[\frac{1}{2}u^2 + \int \frac{dp}{\rho} + (gz)\right] = -(\boldsymbol{\omega} \times \mathbf{u})\,. \tag{2.12}$$

This further simplifies for irrotational flows, with $\boldsymbol{\omega} = 0$ and (2.9), to finally yield the Bernoulli equation for inviscid and irrotational (unsteady) flows:

$$\boldsymbol{\nabla}\left[\frac{\partial \Phi}{\partial t} + \frac{1}{2}u^2 + \int \frac{dp}{\rho} + (gz)\right] = 0\,. \tag{2.13}$$

After this rather general introduction to some concepts of fluid dynamics, the next section will treat some special characteristics of surface waves.

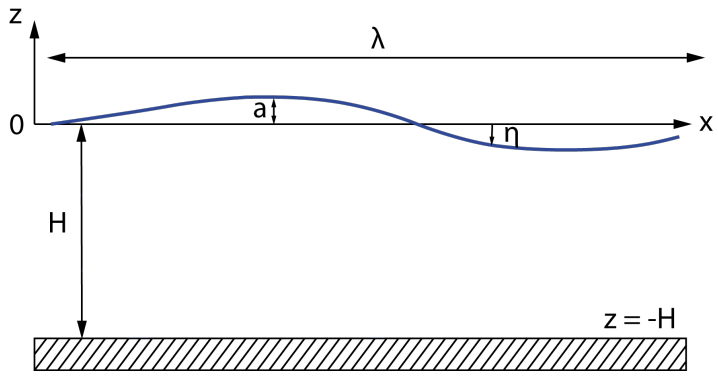

Figure 2.1: Coordinate system for the description of wave propagation.

2.2 Water Waves

2.2.1 Small Amplitude Waves

Surface wave propagation was already studied in the 19$^{\text{th}}$ century by Airy, Stokes, and Boussinesq (Airy, 1845; Boussinesq, 1872; Stokes, 1849). In this section, the dispersion relation for *small amplitude* or *Airy waves* is deduced for irrotational and incompressible flows. Making the assumption of plane waves, the three-dimensional problem can be reduced to a two-dimensional problem, with the wave propagating in the x-direction and the z-axis pointing in the direction opposite to gravity (see figure 2.1). The small amplitude constraint implies that the wave amplitude a is small compared to the wavelength λ, i.e. $a/\lambda \ll 1$. In an irrotational flow a velocity potential can be defined such that

$$u_{\mathrm{x}} = \frac{\partial \Phi}{\partial x}, \qquad u_{\mathrm{z}} = \frac{\partial \Phi}{\partial z}. \tag{2.14}$$

If the flow is incompressible, (2.14) can be combined with the equation of continuity $\boldsymbol{\nabla} \cdot \mathbf{u} = 0$ to yield the Laplace equation for the velocity potential

$$\frac{\partial^2 \Phi}{\partial x^2} + \frac{\partial^2 \Phi}{\partial z^2} = 0. \tag{2.15}$$

Certain boundary conditions have to be specified to obtain a unique solution of the Laplace equation. For surface waves, the *kinematic boundary conditions* state that fluid particles remain in the fluid and can never leave it. This implies that at the bottom of the water body (ocean, wind-wave facility, etc.)

$$\left.\frac{\partial \Phi}{\partial z}\right|_{z=-H} = u_{\mathrm{z}}(-H) = 0, \tag{2.16}$$

because fluid particles cannot flow into the bottom. At the free surface, a fluid particle's vertical velocity u_z has to be equal to the rate of change of the surface level:

$$\left.\frac{D\eta}{Dt}\right|_{z=\eta} = u_z(\eta) \tag{2.17a}$$

$$\left.\frac{\partial\eta}{\partial t} + u_x\frac{\partial\eta}{\partial x}\right|_{z=\eta} = \left.\frac{\partial\Phi}{\partial z}\right|_{z=\eta}. \tag{2.17b}$$

This second boundary condition is nonlinear. To obtain analytical solutions, (2.17) has to be linearized. Since $a/\lambda \ll 1$, the surface slope $\frac{\partial\eta}{\partial x}$ at $z = \eta$ is small. For small motions, also u_x is small (see Kundu, 2007), thus the second term on the left hand side of (2.17b) is quadratic in small quantities and can be neglected. The term on the right hand side of (2.17b) needs to be evaluated at the (unknown) water surface $z = \eta$. To a first order of accuracy, it can be evaluated at $z = 0$ instead. With these assumptions (2.17b) simplifies to

$$\left.\frac{\partial\eta}{\partial t} = \frac{\partial\Phi}{\partial z}\right|_{z=0}. \tag{2.18}$$

The third boundary condition, the *dynamic boundary condition* at the free surface takes into account that the pressure difference between the air above the surface and the water just below the surface is the pressure caused by the surface tension σ:

$$p\Big|_{z=\eta} = -\frac{\sigma}{r}. \tag{2.19}$$

Again, for small amplitude waves this condition can be evaluated at $z = 0$ instead of $z = \eta$ without unreasonable loss of accuracy.

The curvature $1/r$ of the water surface $\eta(x)$ in (2.19) can be approximated as

$$\frac{1}{r} = \frac{\partial^2\eta/\partial x^2}{[1 + (\partial\eta/\partial x)^2]^{3/2}} \approx \frac{\partial^2\eta}{\partial x^2}, \tag{2.20}$$

since $a/\lambda \ll 1$ implies that the surface slope $\partial\eta/\partial x$ is also small.

The velocity potential Φ needs to fulfill the Bernoulli equation (2.13), which can be linearized for small amplitude waves by omitting the u^2 factor as being of second order. The equation, evaluated at $z = \eta$ using (2.19) and (2.20) and absorbing the integration constant into Φ (for a more detailed discussion and complete derivation see Kundu (2007)), then transforms to

$$\left.\frac{\partial\Phi}{\partial t}\right|_{z=\eta} = \frac{\sigma}{\rho}\frac{\partial^2\eta}{\partial x^2} - g\eta \tag{2.21}$$

Again, using the small amplitude constraint, we can evaluate $\frac{\partial \Phi}{\partial t}$ at $z = 0$ rather than at $z = \eta$, so

$$\frac{\partial \Phi}{\partial t}\Big|_{z=0} = \frac{\sigma}{\rho}\frac{\partial^2 \eta}{\partial x^2} - g\eta. \tag{2.22}$$

The Laplace equation for Φ (2.15) needs to be solved under the kinetic boundary conditions (2.18) and (2.16). To get a unique solution, we have to specify a wave form for $\eta(\mathbf{x}, t)$. We assume a monochromatic sinusoidal wave propagating in the x-direction,

$$\eta(x, t) = a\cos(kx - \omega t). \tag{2.23}$$

The motivation for using a sinusoidal wave is coming from the theory of Fourier analysis, which states that any disturbance on the water surface can be decomposed into a linear superposition of sinusoidal components. Wind waves on the ocean are not necessarily sinusoidal.

The derivation of the solution of (2.15) for $\Phi(x, z, t)$ can be found in Kundu (2007) and Kinsman (1965), only the result is presented here:

$$\Phi(x, z, t) = \frac{a\omega}{k}\frac{\cosh k(z + H)}{\sinh kH}\sin(kx - \omega t) \tag{2.24}$$

To get the dispersion relation, i.e. $\omega(k)$, we need to combine (2.24) with the dynamic boundary condition (2.19), the definition of the velocity potential (2.9), and the sinusoidal wave ansatz (2.23) which gives

$$\omega = \sqrt{kg\left(1 + \frac{\sigma}{\rho g}k^2\right)\tanh kH}. \tag{2.25}$$

Deep Water Waves

In deep water and for sufficiently large wavenumbers k, $kH \gg 1$ and thus $\tanh kH \approx 1$, so that equation (2.25) simplifies and the phase velocity is given by

$$c(k) = \frac{\omega}{k} = \sqrt{\frac{g}{k} + \frac{\sigma}{\rho}k}. \tag{2.26a}$$

$$c(\lambda) = \sqrt{\frac{g\lambda}{2\pi} + \frac{\sigma}{\rho}\frac{2\pi}{\lambda}}. \tag{2.26b}$$

The dispersion relation for (pure) water with temperature $T = 20\,°\mathrm{C}$, and consequently the surface tension $\sigma = 72.5\,\mathrm{mN/m}$, $c(\lambda)$, is shown in 2.2 (red solid curve). The green (dashed) curve is obtained by neglecting the first term in (2.26b), the blue (dashdotted) curve by neglecting the second term.

The first term under the root in (2.26b), the gravitational term, is $\propto \lambda$, while the second, the surface tension term, is $\propto \frac{1}{\lambda}$. It is thus clear that the first term is dominant for long wavelengths, waves in this regime are called *gravity waves*, while the second is important for

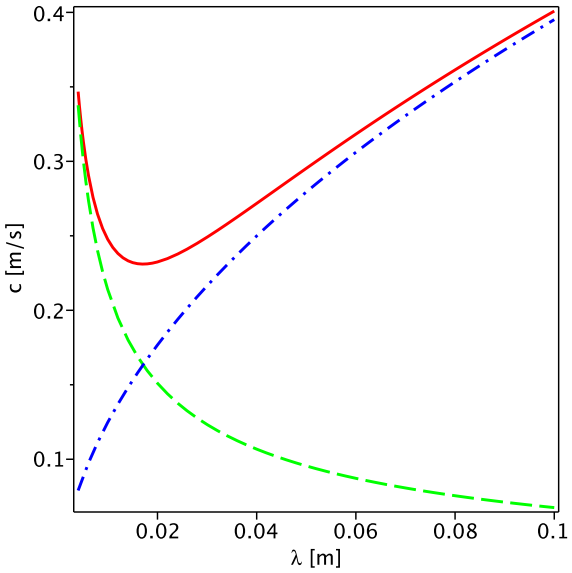

Figure 2.2: Dispersion relation for the phase velocity of water waves (solid red) with contributions from capillary waves (dashed green) and gravity waves (dashdotted blue).

very short wavelengths, where the absolute displacement of a fluid particle is not as important as the relative displacement compared to its neighbors (which leads to increased curvature). Waves in this regime, that are strongly depending on surface tension are called *capillary waves*. The minimum of the combined relation is at $\lambda = 1.71\,\text{cm}$, the corresponding phase velocity is $c_{min} = 23.1\,\text{cm}$.

Finite Depth Effects

In shallow water and for sufficiently small wavenumbers k when $kH \ll 1$, $\tanh kH$ can be approximated as $\tanh kH \approx kH$ in (2.25), which then reduces to

$$\omega = \sqrt{kg \tanh kH} = k\sqrt{gH}. \tag{2.27}$$

The capillary term can be neglected, since surface tension is negligible for small wavenumbers. The phase speed equation (2.26b) simplifies to

$$c = \sqrt{gH} \tag{2.28}$$

and becomes independent of the wavelength or wavenumber. This approximation is accurate with errors of less than 3 % if $H < 0.07\lambda$. Surface waves are thus regarded as *shallow-water waves* if the water depth is $< 7\,\%$ of the wavelength (Kundu, 2007).

2.2.2 Description of the Wave Field

The movement of the water surface of an ocean or lake appear random and chaotic. To some extent they are, but in a sense that they can be described in terms of statistics. For most practical purposes (and certainly for heat and gas transfer, themselves being statistical processes), the behavior of single waves is not of interest.[3]

One way to describe the wave field is in terms of its Fourier transform, which is called the *wave spectrum*. For a general introduction on the spectral description of wave fields see, for instance, Phillips (1977).

Another way to statistically describe the water surface is in terms of *probability density functions* (PDFs) of elevation, slope, curvature, etc. The measurement instrument presented in this work (see section 4.1) can directly measure the slope probability distribution for small slopes. From the probability for these small slopes, statistical parameters like the variance of the distribution – the *mean square slope* – can be estimated.

This requires that the shape of the PDF is known *a priori* and only some coefficients have to be fitted to the acquired data. The slope PDF has been investigated for over 50 years and various parameterizations have been published. Some of most important ones are presented in the next section. The process of extracting statistical parameters from the measurement data is described in section 5.2.

2.3 Surface Slope Probability Distribution

For most applications, it is neither practically possible nor reasonable to describe a water surface in terms of the motions of single fluid packets. Especially for the description of larger scale wave fields in the ocean, it is necessary to use a statistical description to capture the essence of the wave motions. If processes on timescales which are much longer than the lifetime of an individual wave, like gas exchange, are studied, using a statistical description of the wave field is not a limitation.

The elevation of a random sea may be represented to a first approximation as the sum of independent components, say sine waves. Consider the displacement at a single point

$$\eta^{(1)} = \sum a_n \cos(\mathbf{k_n} \cdot \mathbf{x} - \omega_n t + \Theta_n), \tag{2.29}$$

[3] *Tsunamis* and *rogue waves* are prominent exemptions. Due to their sparseness, they would not play a significant role in any statistical description, yet their effects are devastating.

where $\mathbf{k_n}$ is the vector wavenumber and ω_n is the frequency, related to $\mathbf{k_n}$ by the dispersion relation (2.25). Using trigonometric identities, and suitable substitutions (see Longuet-Higgins, 1963), this can be written in the form

$$\eta^{(1)} = \sum_{n=1}^{N'} \left[\xi_n \cos(\mathbf{k}\cdot\mathbf{x} - \sigma t) + \xi'_n \sin(\mathbf{k}\cdot\mathbf{x} - \sigma t)\right] = \sum_{n=1}^{2N'} \alpha_n \xi_n, \tag{2.30}$$

where the α_n are constants for a fixed position and time.

The α_n and ξ_n can be interpreted as independent random variables that are symmetrically distributed about the mean water level 0 with variance V_i. Then, from the central limit theorem, it follows that the probability density function (PDF) $p(\eta)$ converges to a Gaussian distribution (Kendall and Stuart, 1977). A similar argument holds for the surface slope, which is the derivative of the elevation.

However, non-linear interactions between the wave components in (2.30) arise from the non-linearity of the Navier-Stokes equation. The water surface cannot be described as a linear superposition of component waves and higher-order terms have to be accounted for:

$$\eta = \alpha_i \xi_i + \alpha_{ij} \xi_i \xi_j + \alpha_{ijk} \xi_i \xi_j \xi_k + \ldots, \tag{2.31}$$

where the summation convention is used and α_i, α_{ij}, α_{ijk}, etc. are constants. In this higher order description the ξ_i, ξ_j are not independent, so the central limit theorem no longer applies and the joint PDF $p(\eta)$ is no longer Gaussian.

The deviation of the slope PDF from a Gaussian distribution was already noticed by researchers in the middle of the last century (Cox and Munk, 1954b; Schooley, 1954). Since then, a number of models have been developed to parametrize and interpret the non-Gaussianity of the distribution, some of which will be presented in the following sections.

2.3.1 Gram-Charlier Expansion

The first and most widespread parametrization of the slope probability distribution was given by Cox and Munk (1954a). They made use of the fact that the non-linear wave-wave interactions are rather weak and that a Gaussian distribution needs small variations only to describe the slope PDF. These deviations from the normal distribution are described in terms of a *Gram-Charlier* series (Kendall and Stuart, 1977):

$$p(s^*_\mathrm{x}, s^*_\mathrm{y}) = \frac{1}{2\pi\sigma_x\sigma_y} \exp\left[-\frac{1}{2}(s^{*2}_\mathrm{x} + s^{*2}_\mathrm{y})\right] \left[1 + \sum_{i,j=1}^{\infty} c_{ij} H_i(s^*_\mathrm{x}) H_j(s^*_\mathrm{y})\right]. \tag{2.32}$$

Here, $s^*_\mathrm{x} = \frac{s_\mathrm{x}}{\sigma_\mathrm{x}} = \frac{1}{\sigma_\mathrm{x}}\frac{\partial\eta}{\partial x}$ and $s^*_\mathrm{y} = \frac{s_\mathrm{y}}{\sigma_\mathrm{y}} = \frac{1}{\sigma_\mathrm{y}}\frac{\partial\eta}{\partial y}$ are the normalized slope components in the cross- and upwind directions. H_i, H_j are Hermite polynomials, the first five are given in table 2.1.

$H_0(x)$	$H_1(x)$	$H_2(x)$	$H_3(x)$	$H_4(x)$
1	x	x^2-1	x^3-3x	x^4-6x^2+3

Table 2.1: The first five Hermite polynomials.

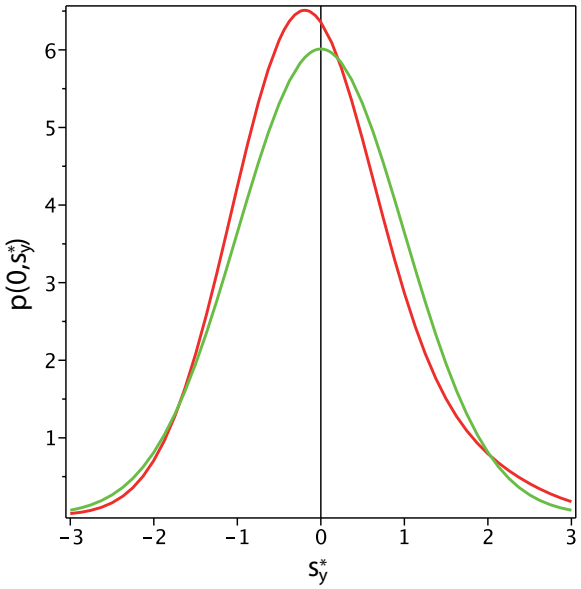

Figure 2.3: The Gram-Charlier expansion (red) according to (2.33) with the coefficient parametrization of Bréon and Henriot (2006), for $U = 10\,\mathrm{m/s}$. The green line is the corresponding Gaussian. The effects of skewness and peakedness are clearly visible.

The series expansion is usually truncated and two empirical facts are included: (1) The mean slope is negligible over an area much greater than the longest ocean wavelength. (2) There is no asymmetry crosswind (as long as the directions of wind and wave propagation are aligned) (Cox and Munk, 1954b). The Gram-Charlier expansion the reduces to (Cox and Munk, 1956)

$$\begin{aligned} p(s_\mathrm{x}^*, s_\mathrm{y}^*) = \frac{1}{2\pi\sigma_x\sigma_y}\exp(-\frac{1}{2}(s_\mathrm{x}^{*2}+s_\mathrm{y}^{*2}))\Big[1-\frac{1}{2}c_{21}(s_\mathrm{x}^{*2}-1)s_\mathrm{y}^* - \frac{1}{6}c_{03}(s_\mathrm{y}^{*3}-3s_\mathrm{y}^*) \\ + \frac{1}{24}c_{40}(s_\mathrm{x}^{*4}-6s_\mathrm{x}^{*2}+3) + \frac{1}{4}c_{22}(s_\mathrm{x}^{*2}-1)(s_\mathrm{y}^{*2}-1) + \frac{1}{24}c_{04}(s_\mathrm{y}^{*4}-6s_\mathrm{y}^{*2}+3). \end{aligned} \tag{2.33}$$

Despite their low number of samples under limited variation of environmental conditions, Cox and Munk's data is generally accepted to be the benchmark for every new PDF that is proposed (Zappa et al., 2008). A recent study evaluating millions of satellite images collected all over the world found good agreement with the Cox-Munk-PDF (Bréon and Henriot (2006)). The deviation of the Gram-Charlier PDF (red) from a Gaussian distribution (green) is shown in 2.3, its strength is determined by the *skewness* coefficients c_{21} and c_{03} as well as the *peakedness* coefficients c_{40}, c_{22}, and c_{04}. Skewness causes an asymmetry of the distribution and shifts the maximum to slightly negative values. Peakedness increases the probabilities for small and large slopes compared to a normal distribution (see 2.3).

Although this parametrization is arguably the most successful, it has been criticized by numerous authors (Liu et al., 1997a; Tatarskii, 2003; Wentz, 1976). Among the arguments given against it are the fact that the truncated expansion is *not* positive for all values of s_x, s_y, thus cannot represent a PDF. Longuet-Higgins (Longuet-Higgins, 1963) criticizes that Cox and Munk fail to deliver a physical justification for the distribution and that any decent function may be represented by such an expansion. However, Longuet-Higgins shows that for weakly non-linear interacting waves a similar expansion, a truncated *Edgeworth series* (see Edgeworth, 1906), can be obtained. In his argumentation, the skewness of the distribution is due to second order non-linear wave-wave interactions, while the peakedness is due to third-order interactions.

2.3.2 Bound Wave Model

An attempt to give additional physical insight into the causes for the skewness of the distribution, beyond the fact that it is caused by nonlinear interaction, is made by Longuet-Higgins (1982). He theoretically investigates multiple effects that could cause non-linearities and finds that the only effect that can yield skewness of the correct magnitude and sign is the modulation of ripples that are riding on longer waves. The ripples do not "see" the mean free water surface, but propagate on a tilted, slowly changing, water surface.

Based on this work, Plant (2003b) obtains a new formulation of the slope PDF by distinguishing two types of waves: free waves and bound waves. Free waves are created directly by the wind, while bound waves arise from non-linear wave interactions. In this model, the slope distribution is the superposition of two statistically independent Gaussian distributions for free and bound waves. Plant (2003a) shows that this approach is in agreement with the Cox & Munk Gram-Charlier parametrization, see figure 2.4.

Another parametrization using multiple Gaussians is given by Tatarskii (2003). Fitting 6 non-centered, non-normalized Gaussians and using fourth order polynomials for the coefficients' dependence on wind speed, the Cox and Munk data can be accurately described. In using such a large number of Gaussians, any effort of a physical interpretation is dropped, since any sufficiently smooth and positive function can be approximated by a sum of Gaussians.

2.3.3 Non-Gaussian Distributions

Motivated by the fact that the Gram-Charlier expansion is not suited to describe large slopes, other non-Gaussian distributions have been proposed. Based on PDFs for wavelength and wave height given by Longuet-Higgins (1975) and assuming statistical independence of both, Liu et al. (1997b) derives the following expression for the wave slope PDF (in terms of the variables used in equation (2.33)):

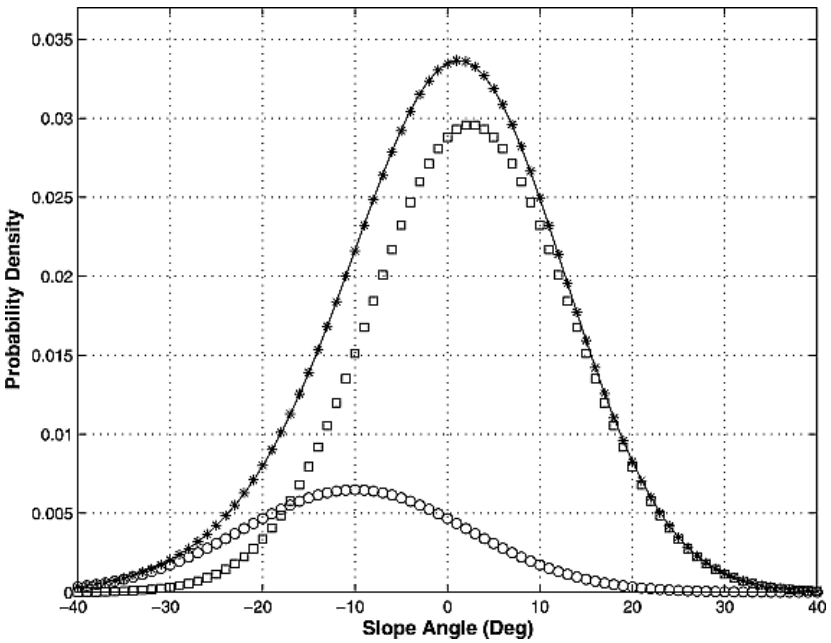

Figure 2.4: Comparison of bound wave/free wave model to Gram-Charlier parametrization. The solid curve is the Gram-Charlier fit to Cox & Munk data for wind speed $U = 13.5\,\mathrm{m/s}$. Circles and squares are the Gaussian PDFs representing bound and free waves, respectively. The asterisks are the sum of circles and squares and coincide with the solid curve. From Plant (2003a).

$$p(s_{\mathrm{x}}^*, s_{\mathrm{y}}^*) = \frac{n}{2\pi(n-1)\sigma_x\sigma_y}\left[1 + \frac{s_{\mathrm{x}}^{*2}}{n-1} + \frac{s_{\mathrm{y}}^{*2}}{n-1}\right]^{-(n+2)/2}. \tag{2.34}$$

The parameter n is called the peakedness coefficient, a skewness term has to be added to equation (2.34) in order to fit experimental data. For large values of n, the proposed formulation is approaching a Gaussian distribution.

Another approach leading to a non-Gaussian slope PDF is given in Chapron et al. (2000). The surface is described as a collection of randomly distributed patches in the order of meters. These patches encompass a dense population of gravity-capillary and short-scale waves and the local slope PDF within a patch is assumed to be Gaussian, while the slope variance parameter is allowed to vary randomly from patch to patch. The resulting slope PDF then is non-Gaussian and, after Bayes' theorem, written as

$$p(\mathbf{s}) = \int p(\mathbf{s}|\alpha)p(\alpha)d\alpha. \tag{2.35}$$

2.4 Reflections at the Water Surface

2.4.1 The Fresnel Equations

When a beam of light hits the water surface, a portion of the intensity is reflected. Since the water surface is, no matter how many waves may be present, smooth at the scale of the optical wavelengths, the water surface acts like a mirror on the incident beam. This mirror may be curved (by waves) and thus focus or defocus the beam. It certainly is not perfect, since by far the largest portion of the intensity is penetrating the water body. The reflection and transmission coefficients are given by the Fresnel equations, which can be derived from the fundamental Maxwell equations (see, for instance Hecht, 2001; Jackson, 1998). Here, only the result is given:

$$R_s = \left(\frac{n_a \cos\theta_i - n_w \cos\theta_t}{n_a \cos\theta_i + n_w \cos\theta_t} \right)^2 = \left(\frac{n_a \cos\theta_i - n_w \sqrt{1 - (\frac{n_a}{n_w} \sin\theta_i)^2}}{n_a \cos\theta_i + n_w \sqrt{1 - (\frac{n_a}{n_w} \sin\theta_i)^2}} \right)^2 \tag{2.36}$$

$$R_p = \left(\frac{n_a \cos\theta_t - n_w \cos\theta_i}{n_a \cos\theta_t + n_w \cos\theta_i} \right)^2 = \left(\frac{n_a \sqrt{1 - (\frac{n_a}{n_w} \sin\theta_i)^2} - n_w \cos\theta_i}{n_a \sqrt{1 - (\frac{n_a}{n_w} \sin\theta_i)^2} + n_w \cos\theta_i} \right)^2 \tag{2.37}$$

In the second formulation, Snell's law

$$\frac{\sin\theta_i}{\sin\theta_t} = \frac{n_w}{n_a} \tag{2.38}$$

was used to express θ_t in terms of θ_i and the refractive indices of air n_a and water n_w.
The first equation holds for light that is polarized in the direction perpendicular to the plane of the incident and reflected ray, the second equation for light that is polarized in the direction parallel to the reflection plane. Unpolarized light is a superposition of both, thus the total reflection coefficient $R = (R_s + R_p)/2$.
Setting $n_a = 1$ and $n_w = 4/3$, the reflection coefficient is $\frac{1}{49}$ for normal incidence. As can be seen from figure 2.5, the reflected intensity is practically constant for near normal incidence with incidence angles up to 0.3 rad. Since in our experimental setup only small incidence angles occur, the angular dependence of the reflectivity can be dropped and reflection brightness can be considered independent of the incidence angle.

2.4.2 Reflection and Refraction

When a beam of light is reflected and refracted at the water surface, the direction of both the reflected and the refracted beam depend on the "direction" of the surface – the surface slope. From the reflection condition $\theta_{in} = \theta_{out}$ or Snell's law in (2.38), the slope can be recovered when the directions of the incident and reflected or refracted beams are known, respectively. Figure 2.6 shows the basic principle of how the surface slope can be obtained

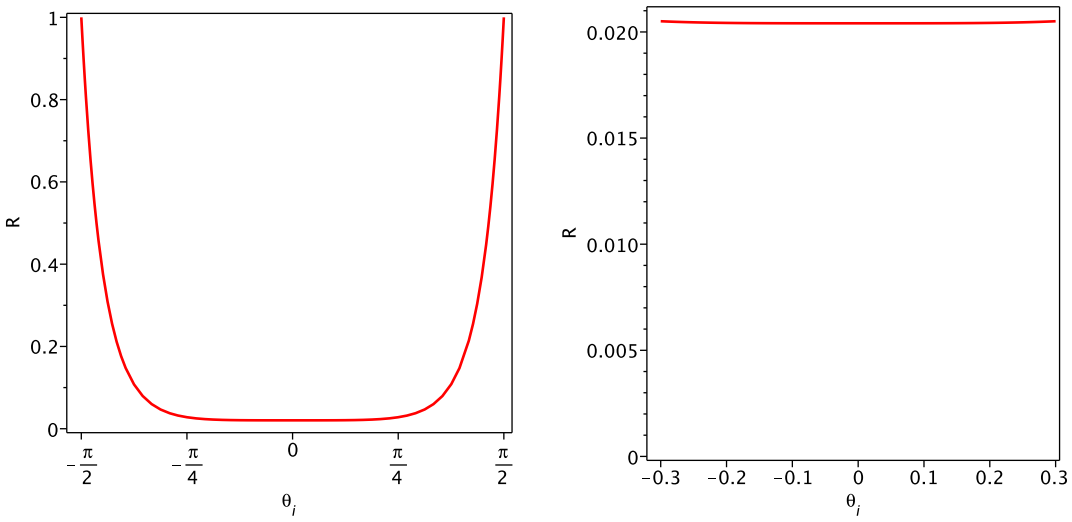

Figure 2.5: *Left:* Reflection coefficient as determined from the Fresnel formula for $n_a = 1$ and $n_w = \frac{4}{3}$.
Right: For near normal incidence, the reflection coefficient is practically constant at about 2%.

from the direction of reflected and refracted light rays. Measurement techniques that employ either one of the principles are presented in section 3.1.1.

2.4.3 Upwelling Light

In section 2.4.1 it was shown that only about 2 % of the incident light is reflected at the air-water interface. For a reflection-based wave imaging method to produce accurate results, it is necessary that reflections that can be seen in the images are actually coming from the water surface and that light is not reflected off particles, sea-weed, fish etc. that are floating in the water below the surface. These reflections can easily have the same (or even a higher) intensity as those coming from the surface and can therefore hardly be separated. One possible solution to the problem is using light with a wavelength that is absorbed in water. Visible light is hardly absorbed by water, which is unfortunate because most cameras are optimized for this part of the spectrum.

Fortunately, in the absorption spectrum of water, there is a peak in the near infrared at 970 nm (see figure 2.7) which is due to a vibrational excitation. By matching the light sources as closely as possible to this peak, the penetration depth (i.e. the depth at which the intensity has decreased to $1/e$) can be significantly reduced and upwelling light be effectively suppressed. While the penetration depth for red light at 650 nm is 295 cm (Pope and Fry, 1997), it is only 2.1 cm at 970 nm (Kou et al., 1993).

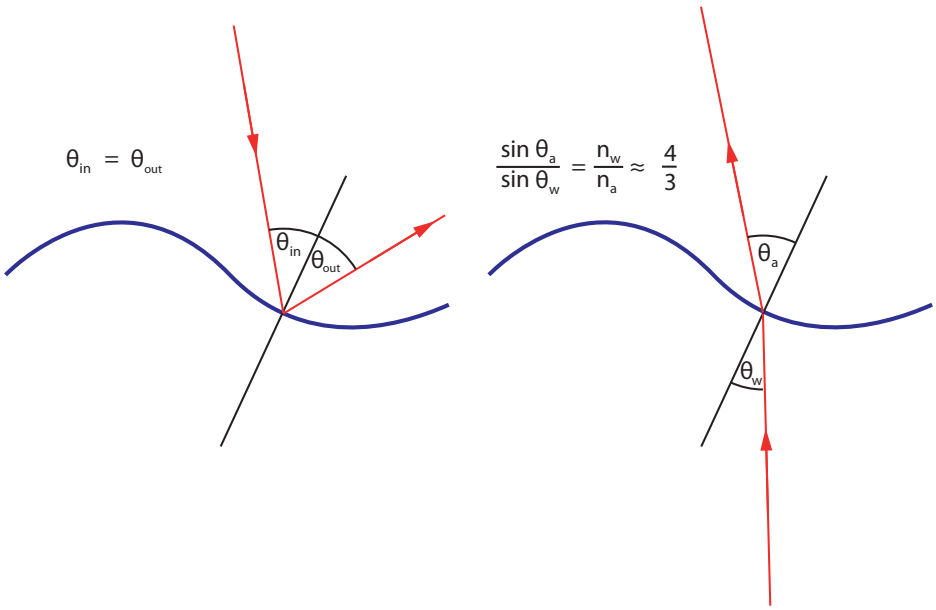

Figure 2.6: *Left:* Reflection: The incident angle equals the reflected angle.
Right: Refraction: According to Snell's law, the ratio of the sines of the angles equals the inverse ratio of the refractive indices.

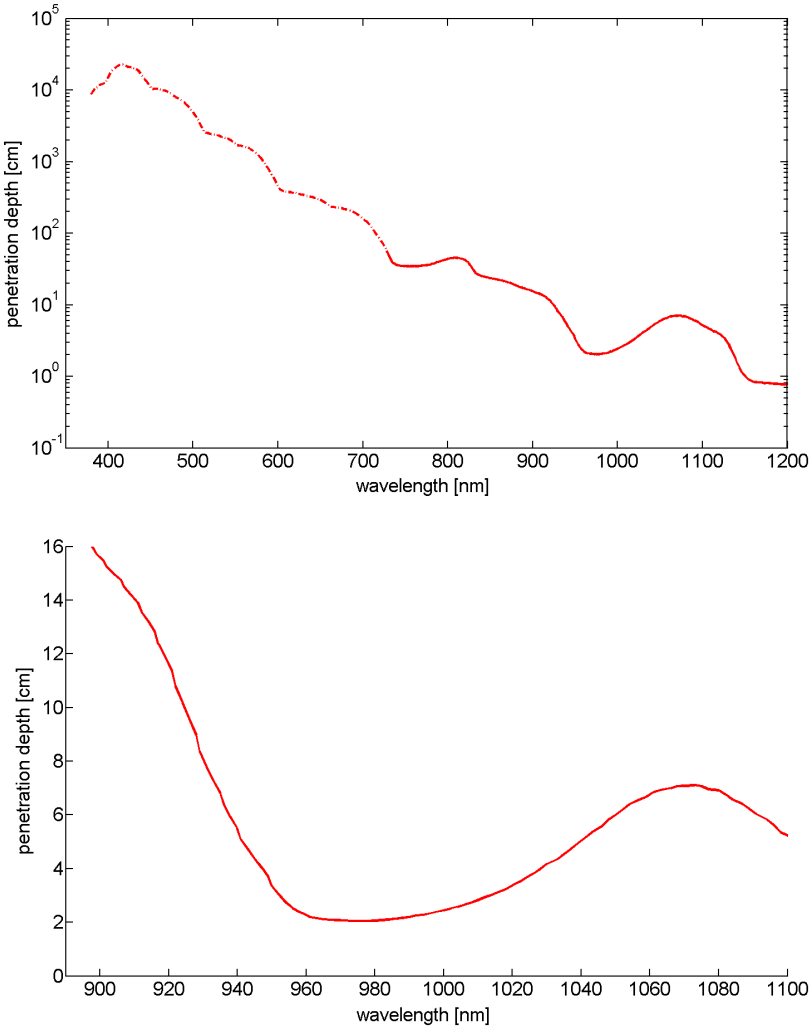

Figure 2.7: The penetration depth of light in water. In the visible range (*upper figure*) the penetration depth is of the order of many meters, at the absorption peak at 970 nm (detail in lower figure) of the order of cm. Data is from Pope and Fry (1997) (dashed line) and Kou et al. (1993) (solid line).

3 Method

3.1 Historical Review of Measurement Methods

3.1.1 Optical Measurement Techniques

Over the past 60 years, a number of methods for measuring wave field parameters have been developed. They range from relatively simple *wave wires*, that can measure water elevation through the variation of resistance or capacity, to elaborated optical techniques, both for laboratory and field use, as well as remote sensing methods, used from satellites, which can detect wave heights and slopes either optically or by the use of radar backscattering. In this chapter, the most important available methods are characterized and a historical overview is given.

Optical methods can be divided into two groups, based on the physical principle they rely on: refraction-based methods (see section 3.1.1) and reflection-based methods (see section 3.1.1). The fundamental physics of reflection and refraction were treated in section 2.4. Numerous implementations of both methods have been made and there are advantages and disadvantages to each of them, which will be described in the following sections. However, only a short overview can be given here, reviews of pros and cons of the available methods can also be found in (Balschbach, 2000; Fuß, 2004; Jähne et al., 1994, 2005; Rocholz, 2005).

Refraction-based Methods

The Cox Slope Gauge A slope meter based on the refraction of light at the air-water interface was first used by Cox (1958). He placed an ink-filled wedge horizontally below a wind wave flume. The wedge was illuminated uniformly from below, such that absorption by the ink created a brightness gradient. Using a photometer and a telescope, he recorded time series of the intensity of the light leaving the water at a certain point. Since the light refraction is dependent on the surface slope, the rays that enter the telescope can be traced back to different origins at the wedge. This way, slope in one direction is coded in light intensity. Although this method was, in Cox's own opinion, "less than ideal" since the intensity was wave height, curvature and even slope dependent, especially for larger slopes, it provided a good basis for further development.

The Laser Slope Gauge In the 1970s, the Cox method was significantly improved by the use of Lasers for lighting. When a Laser is installed in the water with the beam pointing towards the surface, the light is refracted at the air-water-interface and from the deflection the slope at a single point of the surface can be reconstructed. Tober et al. (1973) used graded transmission filters for position detection of the refracted Laser beam, Sturm and Sorrell (1973) and Scott (1974) used photo diodes that were extended in one dimension and cylindrical lenses to focus the beam onto them. Both could, similar to Cox, measure only one slope component at a time. Hughes et al. (1977) were the first to measure two-dimensional slopes. The refracted laser was absorbed on a translucent screen, the position of the laser point on the screen recorded with a modified video camera. By using telecentric lenses, they could make their slope measurement independent of wave height. The maximum recordable deflection and thus the maximum slope was determined by the diameter of the telecentric lenses. The device was eventually installed on a buoy and deployed on the ocean.
A further improvement was the development of the *scanning laser slope gauge* (Bock and Hara, 1992), which can make *de facto* area measurements. The laser scans the water surface at very high frequencies. The change of the surface shape during the scan interval is insignificant and 2D slope data can be recorded..

The Imaging Slope Gauge The imaging slope gauge (ISG) is an enhancement to Cox's method. The photo diode is replaced by a camera, which permits the measurement of the slope in an extended area on the water surface. With an early implementation of the ISG principle, Jähne and Riemer (1990) made the first systematic study of two-dimensional wave spectra. Two orthogonal brightness gradients were used for illumination so that both slope components could be measured in rapid sequence. Zhang and Cox (1994) was the first to measure both slope components simultaneously by using a discrete two-dimensional color matrix. More recent implementations of this color imaging slope gauge (CISG) make use of continuous color gradients and high speed digital cameras (Balschbach, 2000; Rocholz, 2008). Field measurements have been made using an ISG (Klinke and Jähne, 1995), however, since either the light source or the camera have to be installed below the water surface, these measurements are rather difficult and the field measurement device never made it past the prototype phase.

Reflection-based Methods

Reflection-based ocean wave slope measurements have a long history. In contrast to refraction-based techniques, they do not need any submerged parts, illumination and detector can be placed above the water surface. This feature makes them optimal candidates for field measurements.

Stereo Photography Optical wave measurements were performed as early as 1906, when German photographers made use of stereo photography to study coastlines and found that

they could also gather useful information about waves by the same technique. A more detailed historical account and explanation of the technique is given in section 3.1.2.

Cox & Munk Method Cox and Munk are the pioneers of wave *slope* imaging (as opposed to wave *amplitude* imaging, that was done earlier with stereo photography). In 1954, they took photometric (i.e. out of focus) images of sun glitter on the water surface from a plane and were able to derive the wave slope PDF from the brightness distribution in the images. They determined wave spectra, the dependency of mean square slope on wind speed and studied the effects of surface slicks (Cox and Munk, 1954a, 1956, 1954b). Even though they could only gather data on a very limited number of flights and with a relatively narrow spectrum of environmental conditions, their slope measurements were (and to some extent still are) benchmarks for other field measurement methods developed subsequently.

Stilwell Photography Stilwell (1969) used a different approach. He also relied on ambient natural illumination, but instead of imaging sun glitter, he made use of the ambient sky light. Under restricted environmental conditions, the sky can be used as an extended light source with known luminance. A cloudless sky emits light with an intensity gradient in one direction only, a completely overcast sky has uniform brightness. As was shown in section 2.4.1, the reflection coefficient of the water surface depends on the incident angle. Combining these effects, ideally, brightness of the image of the waves should only depend on surface slope. Wave spectra can then be extracted from the image by means of Fourier transformation, a technique applied to images of ocean waves already by Barber (1949). In contrast to the Cox & Munk method, Stilwell photography can capture slope information for (almost) every point in the image, a major drawback are severe restrictions on the environmental conditions under which the method can be applied.

Reflective Slope Gauge The *Reflective Slope Gauge* or *RSG* works similarly to the Cox & Munk method, but with an artificial light source. Early attempts of obtaining slope information by this method go back as far as 1954, when Schooley took flash photography images of the water surface of the Anacostia River (Schooley, 1954). Later, Wu (1971) used a setup with a light source and a telescope to obtain 1d slope information at a single point of the water surface. Although Schooley and Wu could obtain some useful results, the method was not widely used until the advent of digital image processing, when for the first time it was possible to process larger amounts of images (Dieter, 1998; Waas and Jähne, 1992).

If a point-like light source is used, reflections, and therefore information about the surface slope, can only be seen in isolated parts of the image. Theoretically, it would be possible to use an intensity gradient in an extended light source for position coding (similarly to Stilwell photography), however, this has not proven to be of use for the investigation of small-scale waves due to lens effects caused by the curvature of the water surface. In theory, position could also be coded using a light source with a color gradient, but since only 2 % of the light

is reflected and 98 % is transmitted at the air-water interface, upwelling light, that is light reflected from within the water (from floating particles, the bottom of a wind-wave facility, etc.) might have higher intensity than the light reflected at the surface. This is a problem especially for blue light, which has the highest penetration depth (see 2.4.1).

Polarimetric Imaging The reflection coefficient given by the Fresnel equations (2.37) depends on the polarization of the incident light. *Polarimetric Imaging* is an improvement of Stilwell photography, in which not only the incident angle of reflected light is used to reconstruct surface slope, but also its polarization. From the measurement of the four component *Stokes vector*, which contains the intensity, the degree of linear polarization as well as the circular polarization, the wave slope can be deduced (Zappa et al., 2008). Polarimetric imaging poses the same constraints on environmental conditions as Stilwell photography, a uniformly overcast or clear sky is needed. The implementation of Zappa et al. could not resolve capillary waves, because long integration times were needed, Pezzaniti et al. (2009) report that integration times could be reduced to 1 ms at frame rates of 60 Hz.

Non-optical methods

Wave Wires Wave wires are vertically suspended in the water and can measure wave amplitude by measuring the change in capacity or resistance caused by a change in water height. If one desires to measure gravity waves, these wires have sufficient precision. Fast changes in water height, however, cannot be resolved, since water adhesion will not follow the fast motion of the capillary waves. Wave spectra can be reconstructed from two-dimensional water elevation measurements using arrays of wave wires Donelan et al. (1985), but wires may cause spurious waves or wakes when a net flow is present and thus influence each other's measurement.

Radar Backscatter Radar backscatter is "almost" an optical technique, since it also makes use of electromagnetic radiation that is reflected at the water surface, like the reflection-based methods described above. The main difference is that for optical methods, the wavelength of the radiation is much smaller than the wavelengths occurring on the ocean surface, the ocean surface appears to be smooth and reflects light like a mirror. Radar waves have wavelengths comparable to those of short ocean waves, thus they are not reflected from a mirror but scattered at a rough surface; interference effects (*Bragg scattering* etc.) become important. A detailed description of radar scattering at the ocean surface is given by Valenzuela (1978).

Reflection vs. Refraction

For laboratory use, the refraction-based CISG has the advantage of the highest information density. Slope information can be obtained for each point on the water surface. In laboratory

setups, the requirement of having either the light source, or the camera suspended into the water (or placed beneath the water tank), is usually not a restriction.

For field measurements, the use of refraction-based methods is theoretically possible, but interactions of the suspended part of the setup with the wave field cannot be avoided and some sort of buoy is needed to hold the setup. Reflection-based methods do not need any submerged parts, they can be mounted on a ship, a platform, a pier etc. Also, since they do not get in contact with the water, they can be installed in such a way as to minimize (or even eliminate) any distortion of the wave field. Two different measurement techniques seem promising for field experiments under different conditions. Polarimetric (or Stilwell) imaging has the advantage of a higher information density, but poses significant restrictions on environmental conditions, limiting its applicability for field measurements. The Reflective Slope Gauge cannot obtain continuous elevation and slope maps of the surface, but has the advantage of being independent of natural illumination and thus of daytime and environmental conditions. It can also measure wave statistics during experiments conducted at night (e.g. heat transfer experiments).

3.1.2 Stereo Imaging of Water Waves

In contrast to most of the techniques presented in the preceding section, stereo photography is measuring wave elevation and not wave slope. Since slope is the spatial derivative of elevation, $\mathbf{s}(\mathbf{x}, t) = \nabla\eta(\mathbf{x}, t)$, the wave elevation (relative to the mean water level) can be reconstructed from two-dimensional slope measurements and wave slope can be determined from two-dimensional water elevation measurements.

Historical Review

For a long period of time, stereo photography was seen as the only practical approach towards measuring wave fields. It was used as early as 1904 by German oceanographers Laas and Kohlschütter (Kohlschütter, 1906; Laas, 1905, 1906, 1921). At that time, ship-borne stereo photography was primarily used for cartographic purposes, to determine the course of the coastline. As a side effect, wave amplitudes and wavelengths could be determined. This raised the interest of shipbuilders who could use reliable information on wave amplitude distributions to estimate the necessary strength of the ship's side to withhold the impact of waves. Later, Schumacher did systematic measurements of waves using stereo photography and for the first time also took time series at a frequency of 1 Hz (Schumacher, 1939, 1950). His work ended abruptly at the outbreak of World War II. Not long after Schumacher reported on the German experiments at a symposium on gravity waves organized by the National Bureau of Standards in Washington D.C. (Schumacher, 1952), a massive American collaboration, the *Stereo Wave Observation Project* (SWOP) was launched. Air-borne stereo images were taken and simultaneous wave pole reference measurements were conducted aboard a research vessel

in the same area. The manual evaluation of the images was costly and time consuming and despite big personal and financial efforts, only 2 of 100 image pairs were evaluated to yield directional wave spectra (Cote et al., 1960).

Later attempts to extend the measurement of wave spectra to the capillary wave range by e.g. Dobson (1970), Holthuijsen (1983a), Holthuijsen (1983b), Shemdin et al. (1988), and Banner et al. (1989) only had meager success. The number of images that were evaluated were limited due to the huge effort which was necessary. This problem could only be solved with the development of automated digital image processing (Waas, 1988). Especially for the smaller waves, another effect became significant: the stereo images of waves were *similar*, but not *identical*. The reason and consequence of this inherent problem of stereo wave imaging is explained in the following section.

Correspondence Problem

The main task in stereo imaging is finding corresponding points, that is, finding the location of an object in the two stereo images. Once an object is found in both images, its distance from the stereo camera setup is readily determined, provided that the necessary extrinsic calibration parameters (i.e. the position and rotation of the cameras relative to each other) are known.

The correspondence problem cannot be solved in general, certain conditions have to be met by the objects of interest as well as by their environment. Complications can be caused by:

- occlusions: two objects may overlap, one may be (partly) hidden by another
- discontinuities: the surface of objects may be discontinuous, which one might only see from one angle
- brightness differences: objects may have different brightnesses when viewed from different angles due to directed reflection

All these effects influence the appearance of an object in an image, thus complicating the matching of the same object in two images. Fortunately, the water surface is relatively well behaved and does not usually show a lot of these features. Discontinuities and occlusions only occur when waves break.[1]

Stereo imaging works well when objects have distinctive structures that separate them from the background. Unfortunately, the water surface is not usually well structured (although small capillary waves give some sort of structure). Complications for stereo imaging arise from another characteristic of the water surface: on the scale of the optical wavelengths, the water surface is smooth, making it a near perfect specular reflector (i.e. it reflects light like a mirror). As a consequence, when looking at the water surface, one does not really see the water surface itself, but the light source that is illuminating it.

[1] As long as the distance to the water surface is sufficiently larger than the maximum wave amplitude.

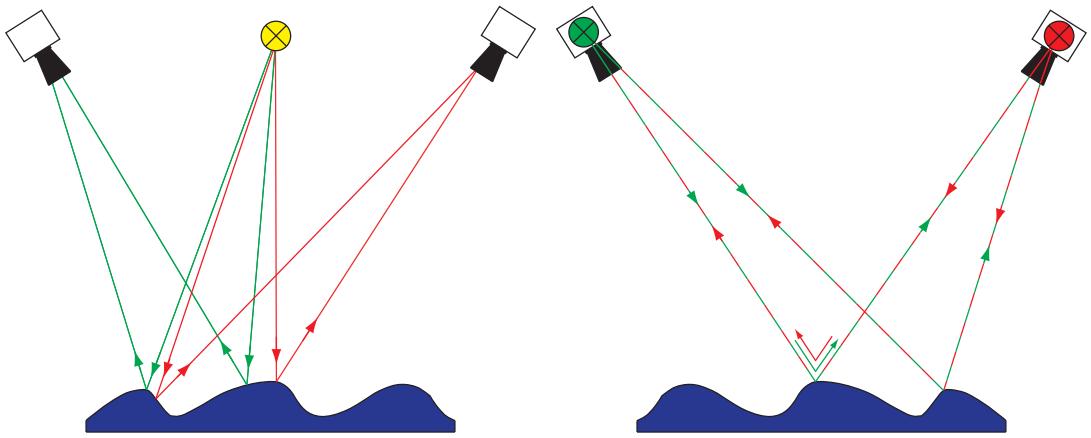

Figure 3.1: *Left*: Stereo imaging with an arbitrary light source: reflections into the two cameras come from different spots on the water surface.
Right: Using two light sources in complementary positions, reflections into the corresponding cameras come from the same spots. Reflections into the "wrong" cameras have to be suppressed.

Stereo imaging works well with Lambertian reflectors, which emit light of the same intensity in all directions and avoid brightness differences in the two images. Accurate stereo imaging of the water surface is possible only by arranging cameras and light sources in a distinctive way, described in section 3.1.2 and developed by Waas and Jähne (1992). The inherent inaccuracies of stereo imaging of water waves with natural illumination limit its applicability to the measurement of gravity waves (Jähne et al., 2005).

The Reflective Stereo Slope Gauge – RSSG

Waas and Jähne (Waas, 1988, 1992) combined the slope measurement principle of the reflective slope gauge (see 3.1.1) with water elevation (height) measurements from stereo photography and thus developed the *reflective stereo slope gauge* (RSSG). By using artificial light sources, they were able to solve the correspondence problem for capillary waves and overcome the limitations of stereo imaging of the water surface.

Figure 3.1 illustrates the problem of an arbitrarily positioned light source, where the two cameras see reflections coming from different spots on the water surface. In this case, stereo imaging is inaccurate, the waves look different in both images, and corresponding points can hardly be found resulting in inevitable mismatches. A similar argument holds for arbitrary extended light sources, like ambient sky light. Therefore, the RSSG can neither rely on Sun glitter nor on ambient sky light for illumination.

This general problem of stereo imaging at specular surfaces can be circumvented if two light sources are used, as is also shown in figure 3.1. The light sources need to be arranged in such a way that the path of the light beam is the same for both cameras. This requires the light sources to be positioned in the center of the image sensor, which obviously is impossible. Fortunately, the requirement can be weakened, it is sufficient for paths of the light beam to

overlap when projected onto axes parallel and perpendicular to the stereo base. This allows for the light sources to be placed next to the cameras in a direction normal to the stereo base, as is done in the experimental setup described in the next chapter.

If the light sources and cameras are arranged in this way, the reflections that can be seen in the two images are equal and corresponding points are easy to determine from the shape of the reflections.

The distance to the water surface (and thereby water elevation and wave amplitude) can then be computed from the parallax (i.e. the shift of the same reflection from one image to the other) of the reflections, which allows a partial 3-dimensional reconstruction of the wave field. Since the distance of the water surface is known for a limited number of points only, it needs to be interpolated. The exact shape of the wave field, especially its structure in the capillary range cannot be recovered.

Knowledge of the distances of the individual speckles is also needed for exact calibration of the slope measurements (see section 3.2). The dependence of the slope corresponding to a reflection at a certain image position on the height is rather weak and a mean calibration usually sufficient, but since the distances can easily be determined for each reflection, a precise calibration is possible.

In the next sections, the principles of height and slope measurements with the reflective stereo slope gauge are explained in detail.

3.2 Slope Measurement Principle

The simplified picture in figure 3.2 illustrates the slope measurement principle. A light ray coming from the light source is reflected at the water surface according to the reflection condition $\theta_{\text{in}} = \theta_{\text{out}}$; the direction of the reflected ray is determined by the surface tilt angle. A surface slope that is corresponding to visible reflections can be assigned to each pixel in the image, the equations become more complex when camera and light source are mounted on a ship that itself may be moving.

3.2.1 The Geometry of Reflection

Figure 3.3 shows the basic geometry of reflection for the RSSG setup. A beam of light coming from the light source at point L is reflected at the water surface, according to the reflection condition . If the water surface tilt α at a position P on the surface is such that $\sphericalangle(\overrightarrow{\text{PL}}, \overrightarrow{\text{PN}}) = \sphericalangle(\overrightarrow{\text{PC}}, \overrightarrow{\text{PN}})$, where P, L, N, and C lie in the same plane, the beam of light is reflected into the camera and a speckle is seen in the image. In this case, the surface normal vector

$$\mathbf{n}^* = \hat{\mathbf{r}} - \hat{\mathbf{i}}, \tag{3.1}$$

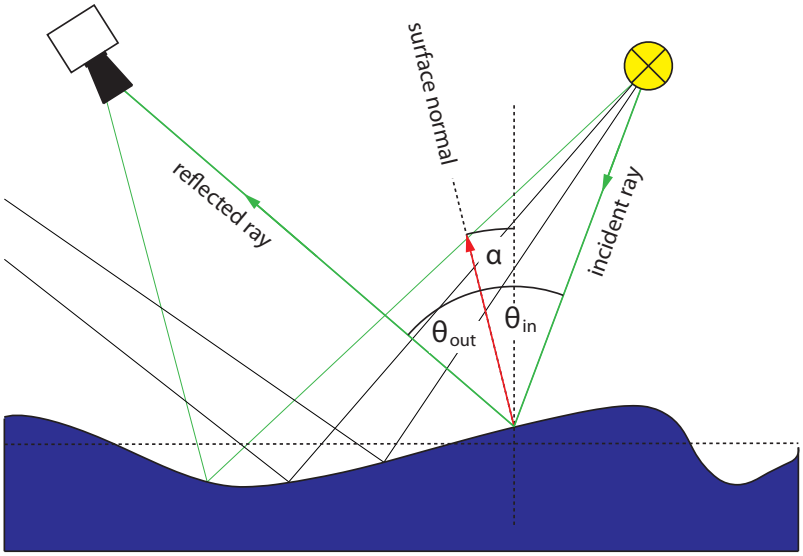

Figure 3.2: The surface tilt angle α under which a reflection of the light source is visible in the camera is uniquely determined by the reflection condition.

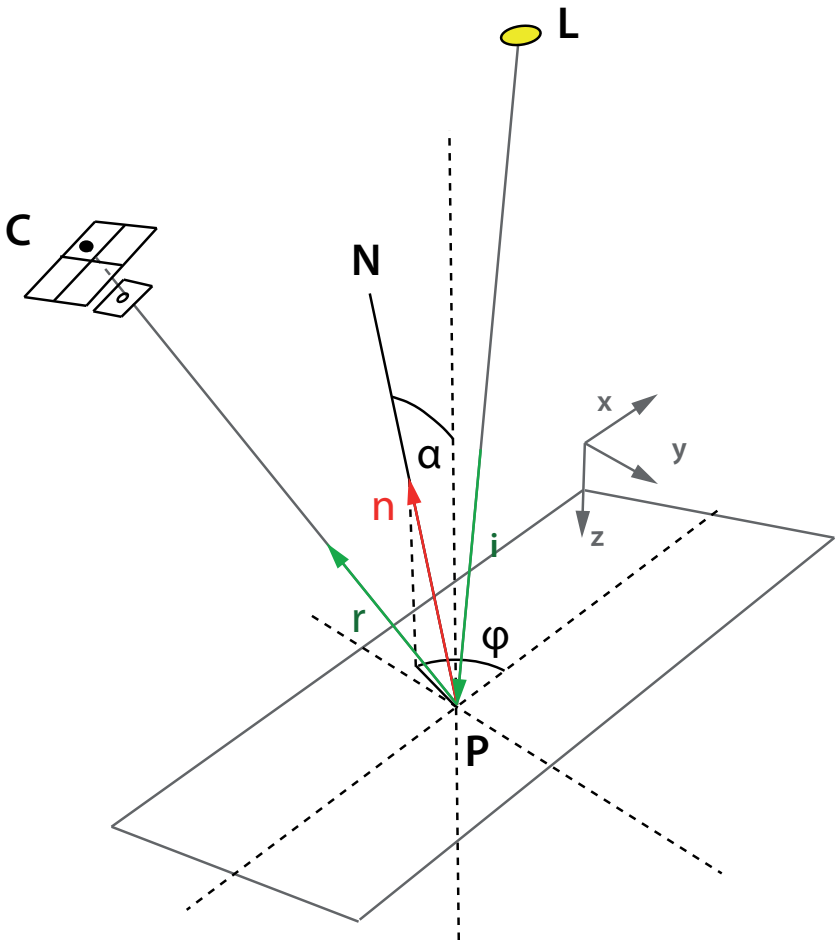

Figure 3.3: The geometry of reflection: A beam of light from the light source at L is reflected at the point on the water surface P into the camera at C, if the surface slope is such that $\theta_{\text{in}} = \theta_{\text{out}}$.

where $\hat{\mathbf{i}}$ is the vector of unit length in the direction of the incident beam and $\hat{\mathbf{r}}$ is the vector of unit length in the direction of the reflected beam. It is convenient to normalize the surface normal vector such that its third component $n_z = 1$, then

$$\mathbf{n} = \begin{bmatrix} \tan\alpha\cos\varphi \\ \tan\alpha\sin\varphi \\ 1 \end{bmatrix}, \tag{3.2}$$

where α is the surface tilt zenith angle and φ the azimuth from the direction of the wind. If x is taken to be the downwind direction, the first two components of $\mathbf{n}$ are the x- and y-components of the surface slope vector

$$\mathbf{s} = \begin{bmatrix} s_x \\ s_y \end{bmatrix} = \begin{bmatrix} \tan\alpha\cos\varphi \\ \tan\alpha\sin\varphi \end{bmatrix} = \begin{bmatrix} \partial\eta/\partial x \\ \partial\eta/\partial y \end{bmatrix}. \tag{3.3}$$

To write down equation (3.1) in terms of image coordinates and light source and camera positions as well as water surface distance, further computation is necessary. It is convenient to work with three different coordinate systems, or reference frames, which will be detailed in the next section.

3.2.2 Reference Frames

The surface slope needs to be measured in a reference system with the x-y-plane being the plane of the mean free water surface level, with the x-axis pointing in the downwind direction, and the z-axis aligned with gravity, which from here on will be called *world coordinate system*.

The positions of the cameras and light sources can are known in a reference system with the origin at the middle of the stereo base, the x-axis aligned with the stereo base, the y-axis in the direction given by the expansion of the light sources, and the z-axis pointing towards the water surface. This system will be referred to as *stereo base coordinate system*, vectors given in this system will be denoted with the index *sb*.

Finally, since the cameras are tilted towards each other to ensure overlapping images in the desired distance, we need to introduce a third frame of reference, the *camera coordinate system*. Its x- and y-axes are aligned with the direction of the x and y pixel coordinates on the image sensor, respectively, its z-axis is pointing into the direction of view (and thus towards the water surface). Vectors in the camera coordinate system have the index *c*.

3.2.3 Transformations Between the Reference Frames

The surface slope needs to be measured in world coordinates. The coordinates of the reflections in the images are given in the camera coordinate system, while information on pitch and roll

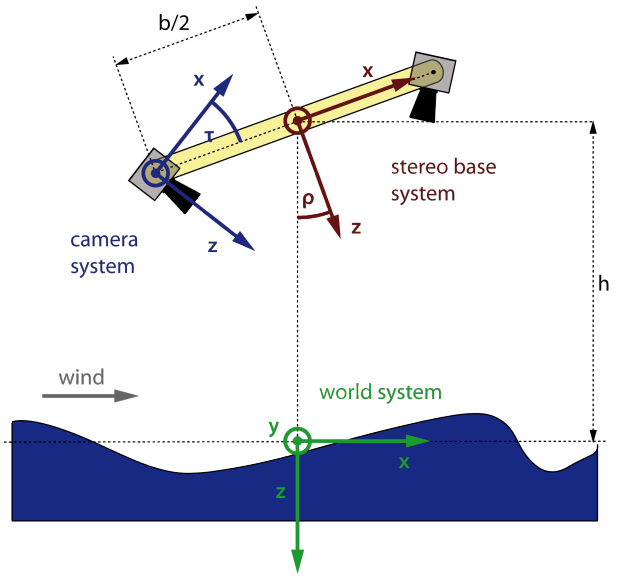

Figure 3.4: The relative positioning of the three coordinate systems. The y-axes are pointing out of the image plane. The depiction is exact if the pitch angle $\psi = 0$. The light sources are virtually placed at the position of the aperture of the cameras.

of the ship will be measured by the inclination sensor in the stereo base coordinate system. To combine this information, it is necessary to know how to transform coordinates from one reference frame into another. Figure 3.4 shows the relative positioning of the coordinate systems in the simplified case of zero pitch.

Stereo Base Coordinate System to Camera Coordinate System

The origin is shifted from the middle of the stereo base to the center of the image sensor, that lies on the x-axis of the stereo base coordinate system. Thus, a shift of $\pm\, b/2$ (with stereo base b) is necessary (more general: the origin is shifted by $\mathbf{c_{sb}}$, the position of the camera in the stereo base coordinate system and origin of the new coordinate system). Furthermore, the cameras are rotated about an axis parallel to the y-axis of the stereo base system by the angle τ. The coordinate transformation can be described with the rotation matrix ($C(\tau)$):

$$\mathbf{x_c} = \mathbf{C}(\tau)\ (\mathbf{x_{sb}} - \mathbf{c_{sb}}) = \begin{bmatrix} \cos(\tau) & 0 & \sin(\tau) \\ 0 & 1 & 0 \\ -\sin(\tau) & 0 & \cos(\tau) \end{bmatrix} (\mathbf{x_{sb}} - \mathbf{c_{sb}})\,. \tag{3.4}$$

Stereo Base Coordinate System to World Coordinate System

For a static laboratory setup, the stereo base coordinate system can be chosen to coincide with the world coordinate system – except for a shift of the origin by the distance h, the elevation of the stereo base relative to the mean water level (see figure 3.4).

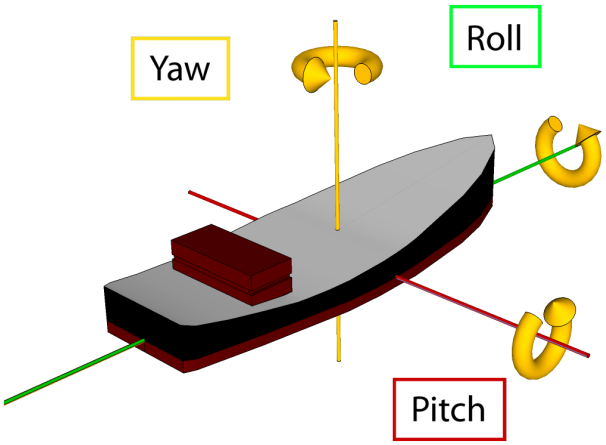

Figure 3.5: Nomenclature of rotational degrees of freedom for ships: *Yaw* is a rotation about the vertical axis, *pitch* is a rotation about the transverse axis, and *roll* is a rotation about the longitudinal axis.

During field experiments on research vessels however, the stereo base is not always parallel to the mean water level, since the ship may be pitching and rolling in longer waves and swell (see figure 3.5 for ship rotation nomenclature). The wind following system described in section 4.1.1 will ensure that the stereo base is always pointing in the up-/downwind direction during acquisition, so that no "yaw" correction is needed.

Using an inclination sensor, the inclination angles ψ due to pitch and ρ due to roll can be measured. The stereo base coordinate system can then be rotated so that its z-axis is pointing in the direction of gravity. If then the origin is shifted along this axis to the mean water level, the world coordinate system is obtained. The complete transformation for an arbitrary vector from stereo base coordinates to world coordinates is:

$$\begin{aligned} \mathbf{x} &= \mathbf{P}(\psi)\,\mathbf{R}(\rho)\,\mathbf{x_{sb}} - \begin{bmatrix} 0 \\ 0 \\ h \end{bmatrix} \\ &= \begin{bmatrix} 1 & 0 & 0 \\ 0 & \cos(\psi) & -\sin(\psi) \\ 0 & \sin(\psi) & \cos(\psi) \end{bmatrix} \begin{bmatrix} \cos(\rho) & 0 & -\sin(\rho) \\ 0 & 1 & 0 \\ \sin(\rho) & 0 & \cos(\rho) \end{bmatrix} \mathbf{x_{sb}} - \begin{bmatrix} 0 \\ 0 \\ h \end{bmatrix}. \end{aligned} \tag{3.5}$$

3.2.4 Ray Geometry

The question that needs to be answered for slope probability measurement is: What is the surface slope corresponding to a reflection at the image coordinates u, v?

As will be shown, this slope does not only depend on the image coordinates, but also on the height of the camera above the water surface. This height can be assumed to be known, since it is retrieved from stereo triangulation described in section 3.3.

By the intercept theorem, we know that

$$\begin{bmatrix} u \\ v \\ f \end{bmatrix} = f \begin{bmatrix} x_c/z_c \\ y_c/z_c \\ 1 \end{bmatrix}, \tag{3.6}$$

with the image coordinates u, v, and the focal length[2] f in pixels. If the distance z_c of an object (e.g. a reflection on the water surface) is known, then its position in camera coordinates is

$$\mathbf{x_c} = \begin{bmatrix} x_c \\ y_c \\ z_c \end{bmatrix} = \begin{bmatrix} z_c u/f \\ z_c v/f \\ z_c \end{bmatrix}. \tag{3.7}$$

For each position $\mathbf{x_c}$ in 3D space, the slope that is necessary to reflect light from a light source at $\mathbf{l_c}$ into the camera (pinhole) aperture at $\mathbf{c_c}$ can be computed from equations 3.1 and 3.2:

$$\mathbf{n_c^*} = \hat{\mathbf{r_c}} - \hat{\mathbf{i_c}} = \frac{\mathbf{r_c}}{|\mathbf{r_c}|} - \frac{\mathbf{i_c}}{|\mathbf{i_c}|} = \frac{\mathbf{c_c} - \mathbf{x_c}}{|\mathbf{c_c} - \mathbf{c_c}|} - \frac{\mathbf{x_c} - \mathbf{l_c}}{|\mathbf{x_c} - \mathbf{l_c}|}. \tag{3.8}$$

Combining (3.7) and (3.8), we have the desired relation of image coordinates and slope. This slope is given in the camera coordinate system, the transformation into world coordinates is described in section 3.2.3.

$$\mathbf{n^*} = \mathbf{P}(\psi)\, \mathbf{R}(\rho)\, \mathbf{C^{-1}}(\tau)\, \mathbf{n_c^*} \tag{3.9}$$

The vector then needs to be normalized according to (3.2) to obtain the slope components.

Figure 3.6 (left) shows the slope-position-function, which allows to determine the slope corresponding to a reflection at a certain image position, in terms of the pixel coordinates in x-direction (the center of the image here has coordinates (0,0)). The slope is plotted for water surface distances of $Z = 4\,\mathrm{m}$, $Z = 6\,\mathrm{m}$, and $Z = 8\,\mathrm{m}$. Variation in water surface distance of this order of magnitude can occur during ship-borne field experiments; figure 3.6 shows that the calibration of the slope reconstruction needs to account for this distance variability.

In figure 3.6 (right) the slope-position-function is shown for typical laboratory conditions. The water distance variability is much smaller – the five lines correspond to surface elevations of -20 cm (blue dashes), -10 cm (green dots), 0 cm (solid red curve), 10 cm (yellow dashdots), and 20 cm (pink spaced dashes) at a distance of 4.863 m, see 4.3 – thus the effect of distance variation on the slope-position-function is negligible (note the different range of the abscissa). The variations are in the order of 10^{-4}, the accuracy of the slope measurement is limited by

[2] f is not the focal length which is given as a characteristic of a lens, but the actual distance of the image sensor plane to the lens.

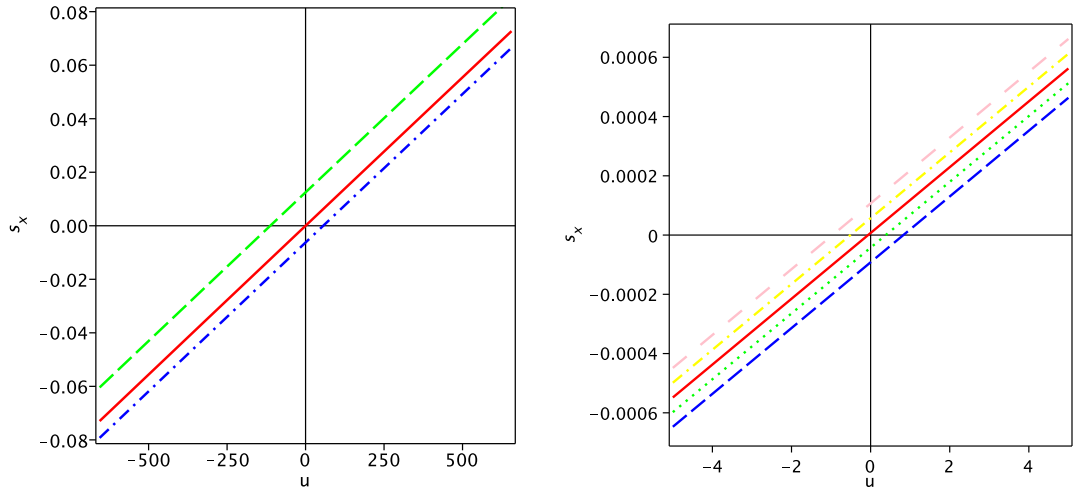

Figure 3.6: *Left*: Slope-position-function for water surface distances $Z = 4\,\mathrm{m}$ (red, solid), $Z = 6\,\mathrm{m}$ (green, dashed), and $Z = 8\,\mathrm{m}$ (blue, dashdot). Used parameters: stereo base length $b = 300\,\mathrm{mm}$, stereo reference height (see section 3.3) $Z_0 = 6000\,\mathrm{mm}$.
Right: Slope-position-function for laboratory conditions. The lower variability in water distance leads to smaller effects on slope calibration. Used parameters: stereo base length $b = 235\,mm$ (see 4.1), stereo reference height $Z_0 = 4863\,\mathrm{mm}$.

the finite size of the light source, to a precision of about 0.001. Thus, the effect of changing water height is negligible for moderate wind speeds in the laboratory.

3.3 Height Measurement Principle

3.3.1 Distance from Stereo Triangulation

When an object is observed from different positions, it is observed from different perspectives. The different perspectives lead to a shift of the projection of the object onto the image plane (Jähne, 2005). Figure 3.7 illustrates the origin of this shift, called the *stereo parallax*. If the stereo cameras have parallel optical axes and are not tilted towards each other, one finds from figure 3.8 that the parallax is

$$p = x_\mathrm{r} - x_\mathrm{l} = f\,\frac{X + b/2}{Z} - f\,\frac{X - b/2}{Z} = b\,\frac{f}{Z} \quad \Rightarrow \quad Z = b\,\frac{f}{p}\,. \tag{3.10}$$

In this simplified setup, the parallax is inversely proportional to the distance from the object Z. The stereo setup used in the new implementation of the RSSG is more complicated. The optical axes of the cameras are tilted towards each other to ensure maximum overlap of the footprints at the mean water level (see figure 3.9).

The catch of using tilted axes is that images get distorted in the direction orthogonal to the stereo base. This makes automated evaluation of the images more complex. With parallel

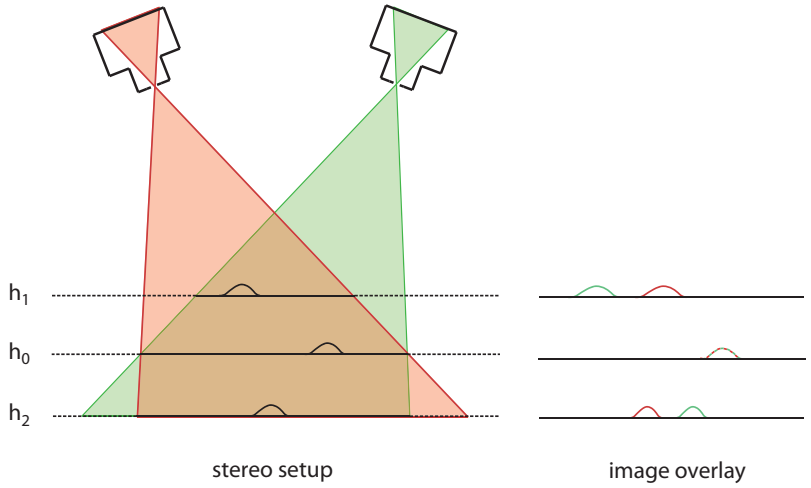

Figure 3.7: The effect of stereo parallax: An object at the reference distance h_0 is projected onto the same image coordinates in both images. For smaller (h_1) or greater (h_2) distances, image coordinates are shifted, the parallax is the relative shift in the overlay image.

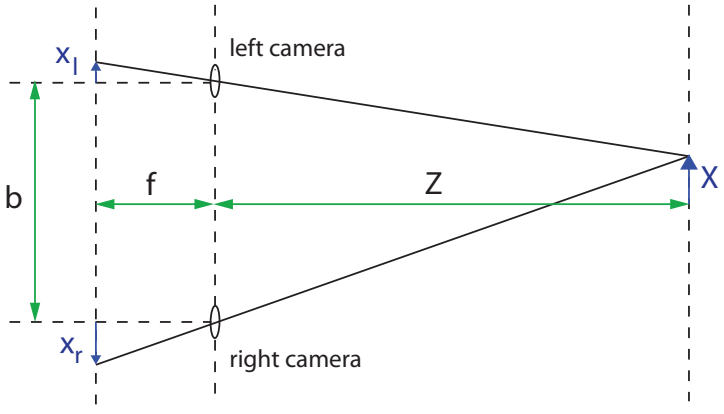

Figure 3.8: Schematic of a stereo camera setup with parallel optical axes. Modified after Jähne et al. (2005).

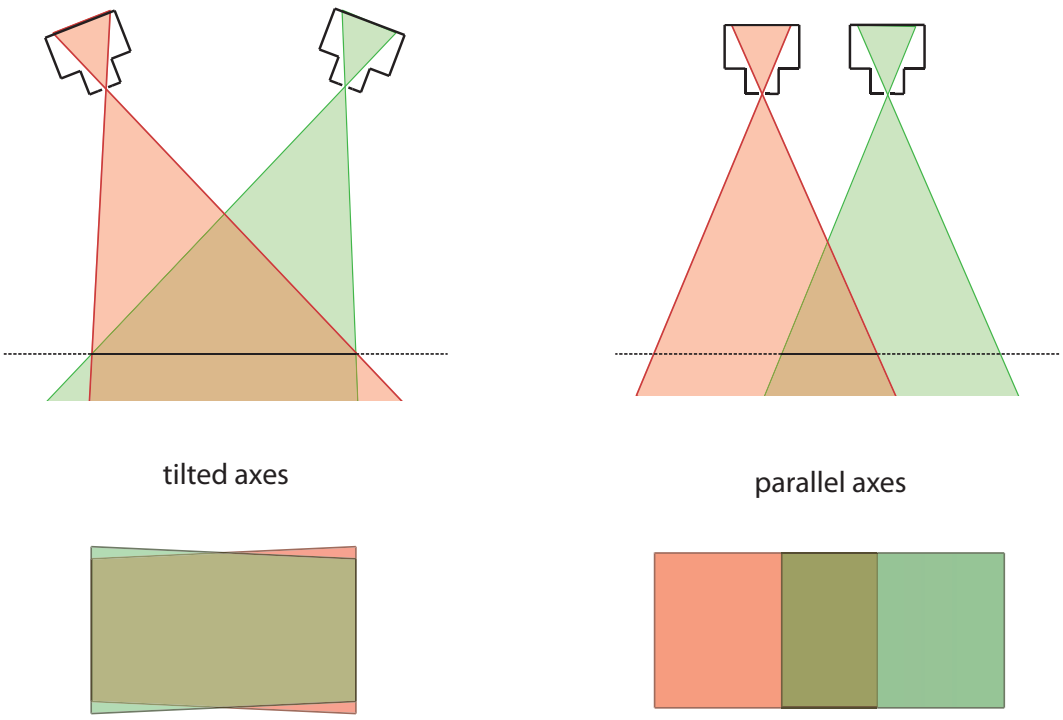

Figure 3.9: *Left:* Tilted optical axes allow setting of a reference height with maximum overlap of the images. Distortions occur in the direction normal to the stereo base.
Right: Parallel optical axes lead to a decreased overlap of the size of the stereo base, independent of the object distance. For small stereo base to distance fractions, this setup is attractive due to simplified computations.

axes, objects are shifted only in the direction of the stereo base, therefore correlation algorithms used to find the most probable parallax may be limited to searching in 1D. For tilted axes the search range has to be extended to 2D which increases the time needed for the computations. However, if parallel axes were used in the RSSG setup, at 6 m distance only about 60 % of the image areas would overlap and could be used for stereo height reconstruction.

3.3.2 Dependence of Parallax on Object Distance

As was noted before, the dependence of the parallax in the stereo images on the distance of the object is more complex for tilted optical axes than the simple $\propto \frac{1}{Z}$ relation derived in equation 3.10 for parallel axes.

Consider a point $\mathbf{x_{sb}}$ on the water surface. Light coming from this point is, in general, projected onto different locations on the image sensor. These locations can be determined for each of the cameras with the help of (3.4), which gives the transformation of a vector given in stereo base coordinates to the respective camera coordinates[3]:

$$\mathbf{x_{r,c}} = \mathbf{C}(\tau)\,(\mathbf{x_{sb}} - \mathbf{c_{r,sb}}) \qquad \mathbf{x_{l,c}} = \mathbf{C}(-\tau)\,(\mathbf{x_{sb}} - \mathbf{c_{l,sb}}) \tag{3.11}$$

Note that the right camera is tilted by the angle τ, while the left camera is tilted by the angle $-\tau$, in the opposite direction. To get the parallax, we recall (3.6), which gives the image coordinates u and v for any position $\mathbf{x_c}$:

$$\mathbf{p_l} = \begin{bmatrix} u_l \\ v_l \\ f \end{bmatrix} = f \begin{bmatrix} x_{l,c}/z_{l,c} \\ y_{l,c}/z_{l,c} \\ 1 \end{bmatrix} \qquad \mathbf{p_r} = \begin{bmatrix} u_r \\ v_r \\ f \end{bmatrix} = f \begin{bmatrix} x_{r,c}/z_{r,c} \\ y_{r,c}/z_{r,c} \\ 1 \end{bmatrix} \tag{3.12}$$

Then, the two-dimensional parallax[4] is given by

$$\mathbf{p} = \mathbf{p_l} - \mathbf{p_r} = f \left(\begin{bmatrix} x_{l,c}/z_{l,c} \\ y_{l,c}/z_{l,c} \end{bmatrix} - \begin{bmatrix} x_{r,c}/z_{r,c} \\ y_{r,c}/z_{r,c} \end{bmatrix} \right). \tag{3.13}$$

Using the known camera positions $\mathbf{c_{l,sb}} = (-b/2, 0, 0)$ and $\mathbf{c_{r,sb}} = (b/2, 0, 0)$, parallax is

$$\mathbf{p} = f \begin{bmatrix} \dfrac{\cos\tau\,(x+\frac{1}{2}b) - \sin\tau\,Z}{\sin\tau\,(x+\frac{1}{2}b) + \cos\tau\,Z} - \dfrac{\cos\tau\,(x-\frac{1}{2}b) + \sin\tau\,Z}{-\sin\tau\,(x-\frac{1}{2}b) + \cos\tau\,Z} \\ \dfrac{y}{\sin\tau\,(x+\frac{1}{2}b) + \cos\tau\,Z} - \dfrac{y}{-\sin\tau\,(x-\frac{1}{2}b) + \cos\tau\,Z} \end{bmatrix}. \tag{3.14}$$

[3] Indices r and l denote the reference frames of the right and left camera, respectively.

[4] The third component is dropped here, since it has no further significance, only the 2D image coordinates are of interest.

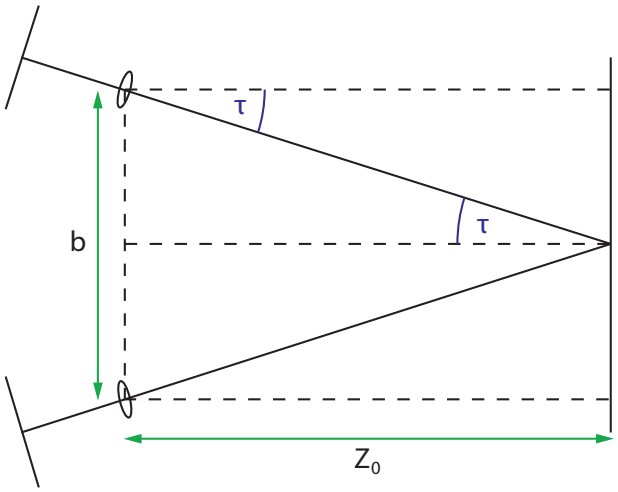

Figure 3.10: Tilted axes can be characterized by either the angle τ or by the stereo base b and the reference height Z_0.

The relation in (3.14) needs to be solved for the height Z. To get a useful relation, instead of the world coordinates x and y the left image coordinates u_l and v_l are used, see (3.12). Equation (3.14) can be solved for the height Z, which gives:

$$Z = \frac{b\left(f^2\cos^2\tau + (p_1 u_\mathrm{l} - u_\mathrm{l})(1-\cos^2\tau) - p_1 f \sin\tau\cos\tau\right)}{p_1 f(2\cos^2\tau - 1) + (2f^2 + 2u_\mathrm{l}^2 - 2p_1 u_\mathrm{l})\sin\tau\cos\tau}. \tag{3.15}$$

Note that only the first component p_1 of the 2D parallax in (3.14) is needed to reconstruct the water height. This was expected, since the p_2 component is merely an artifact from image distortions due to the tilting of the cameras. Also note that the result is consistent with the result obtained for parallel optical axes; in the limiting case of $\tau = 0$, from (3.15) one obtains (3.10) as is required.

While (3.15) is descriptive in the sense that the limiting case of parallel axes can be easily obtained, for practical purposes a different representation is advantageous. The tilting angle τ is not an independent variable, but a function of stereo base length b and what will be called *stereo reference height* Z_0. This reference height is the distance at which the images overlap and an object at the image center has zero parallax. As can be seen from figure 3.10,

$$\tau = \arctan\left(\frac{b}{2Z_0}\right). \tag{3.16}$$

Using (3.16) and the trigonometric identities

$$\sin(\arctan x) = \frac{x}{\sqrt{1+x^2}} \quad \text{and} \quad \cos(\arctan x) = \frac{1}{\sqrt{1+x^2}}, \tag{3.17}$$

equation (3.15) transforms to (the indices of u_l and p_1 are omitted for clarity)

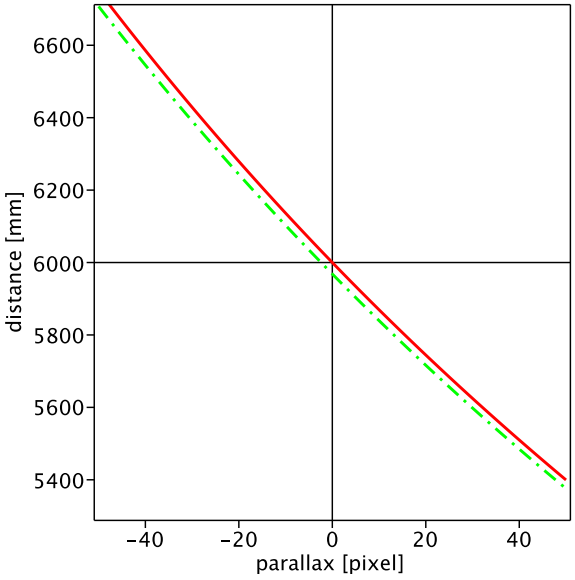

Figure 3.11: The height-parallax-function. The red (solid) curve is for the center of the image ($u = 0$), the green (dashed) curve for a pixel at the image border ($u = 656$). Used parameters: $f = 72\,\text{mm}$, $b = 300\,\text{mm}$, $Z_0 = 6000\,\text{mm}$.

$$Z = -\frac{b\left(4f^2Z_0^2 - 2pbfZ_0 + pub^2 - u^2b^2\right)}{-4pfZ_0^2 - (4bu^2 - 4pbu + 4bf^2)Z_0 + pfb^2}. \tag{3.18}$$

In figure 3.11 the height-parallax dependence is plotted for parameters similar to those used in field experiments, the stereo base $b = 300\,\text{mm}$ and the reference height $Z_0 = 6000\,\text{mm}$.

4 Setup and Simulation

In section 3.1.1, a number of wave measurement methods were presented. It was concluded that the reflective slope gauge (RSG) is best suited to provide wave slope statistics during field experiments when measurements have to be carried out under arbitrary environmental conditions. Then, in section 3.1.2, it was shown how the reflective slope gauge can be enabled to also measure water elevation by using a stereo camera setup. This reflective stereo slope gauge was first developed by Waas (1988, 1992). The technical limitations of the time restricted the automated image evaluation and prevented the routine use of the instrument. Dieter (1998) developed a new implementation of the RSSG principle in the late 1990s that was also able to measure curvature statistics. This HSCI (height/slope/curvature instrument) was used for measurements from a pier and from a research vessel on the open ocean, although results are published for static pier measurements only.

4.1 Experimental Setup

4.1.1 Setup of the Stereo Camera System

The RSSG measurement principle was detailed in section 3.2 and 3.3. Simultaneous measurements of wave height and slope are possible by combining the reflective slope gauge principle (see figure 3.2), which can measure slope statistics for small waves down to the capillary range, and stereo photography (see figure 3.7), which can measure height statistics for gravity waves and provide calibration data for the slope measurements.

Figure 4.1 shows the stereo camera setup that was used for laboratory experiments. Two LED arrays are used for illumination and are fixed to the camera lenses. Figure 4.2 shows the improved instrument that was built for field measurements. The size of the light sources is increased almost by a factor of 4.

An important improvement over earlier realizations of the measurement principle by Waas (1992) and Dieter (1998) is the use of near infrared light for illumination. By matching the light spectrum to the water absorption band at 970 nm, the effect of upwelling light (see 2.4.3) can be reduced.

All components of the RSSG were carefully selected, some of the criteria that were relevant in the selection process are detailed below.

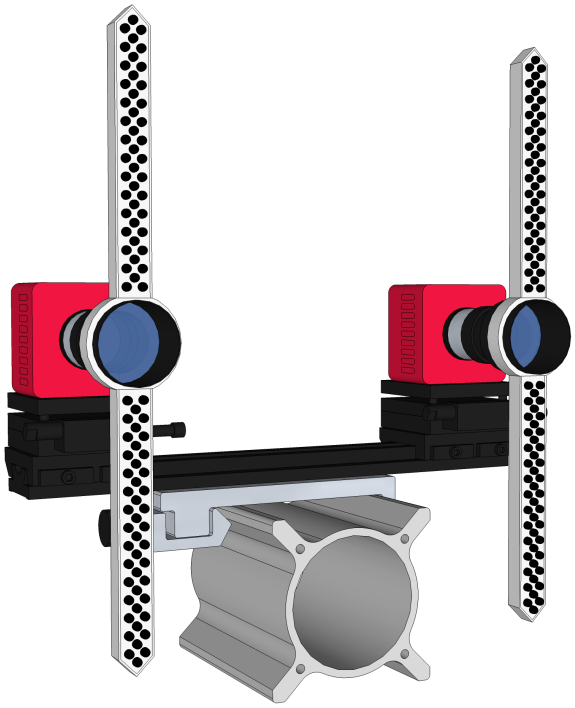

Figure 4.1: Sketch of the setup used for laboratory experiments at the *Aeolotron*; two IR-LED arrays (with 90 LEDs each) are fixed to the camera lenses, the stereo base is 235 mm.

Cameras

The cameras are required to have certain features:

- high sensitivity (quantum efficiency) in the near infrared
- high resolution to resolve reflections from small capillary waves
- high frame rate for good statistics

The cameras that were selected are a pair of *Photonfocus MV1-D1312I-CL-12* CMOS-cameras with enhanced infrared sensitivity. While all CCD and CMOS sensors are sensitive in the near infrared, quantum efficiency is usually very low. The *Photonfocus* cameras with extended infrared sensitivity were the best available product that at the same time met the other requirements. Some specifications are given in table 4.1.

Camera data is read out by a frame grabber (*Silicon Software MicroEnable 4*). This special interface is necessary because of the high data rate; acquiring mega-pixel images at a rate of 100 Hz with these cameras produces 540 MB/s of raw data.

The stereo base of the two-camera setup was 235 mm for laboratory experiments (figure 4.1). In the field setup (figure 4.2), the stereo base was increased to 300 mm to increase the height resolution.

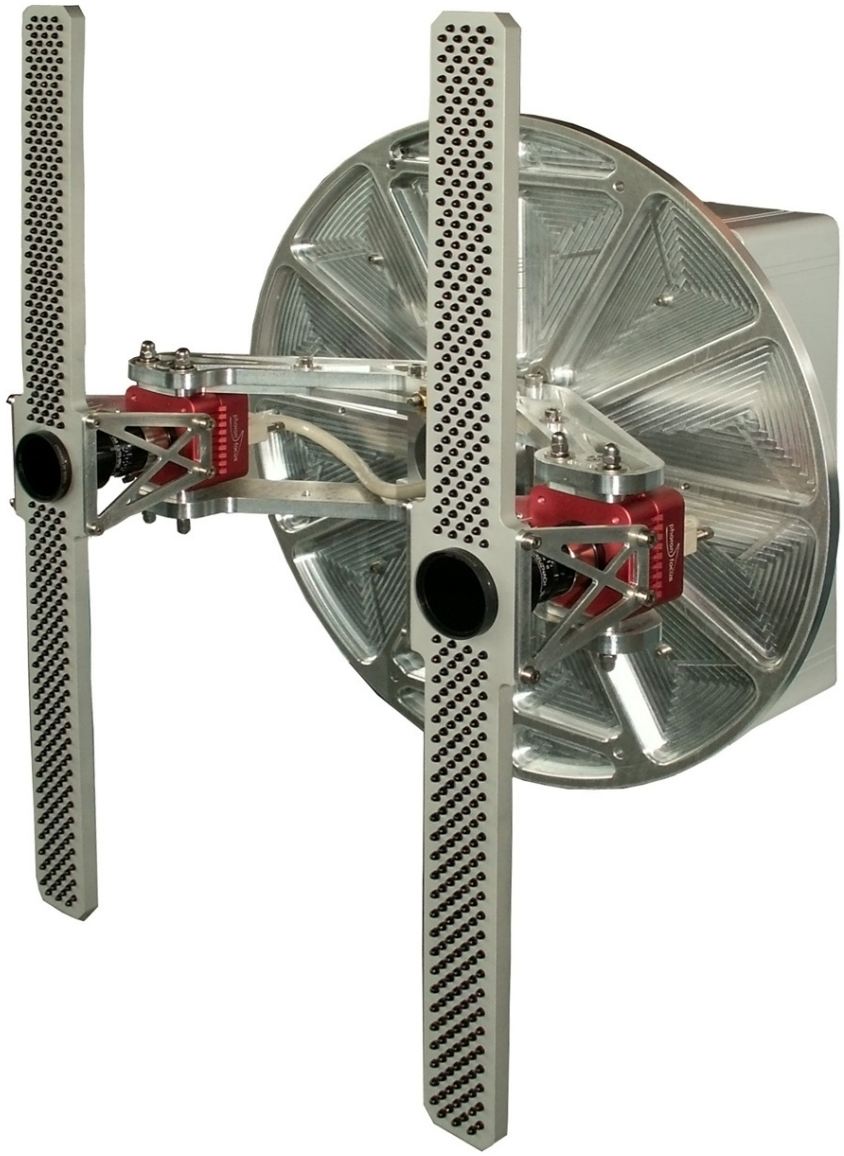

Figure 4.2: The setup that will be used for field experiments. The stereo base is increased to 300 mm and the LED arrays are built from 350 IR-LEDs each. The image acquisition system consisting of cameras and light sources can be rotated about the center of the stereo base.

Camera Specifications	
Resolution	1312 x 1082 pixel
Pixel size	8 µm x 8 µm
Spectral sensitivity	< 350 to 1100 nm
Exposure time	10 µs - 0.41 s
Frame rate	108 Hz
Grey scale resolution	12 bit

Table 4.1: Specifications of the Photonfocus MV1-D1312I-160

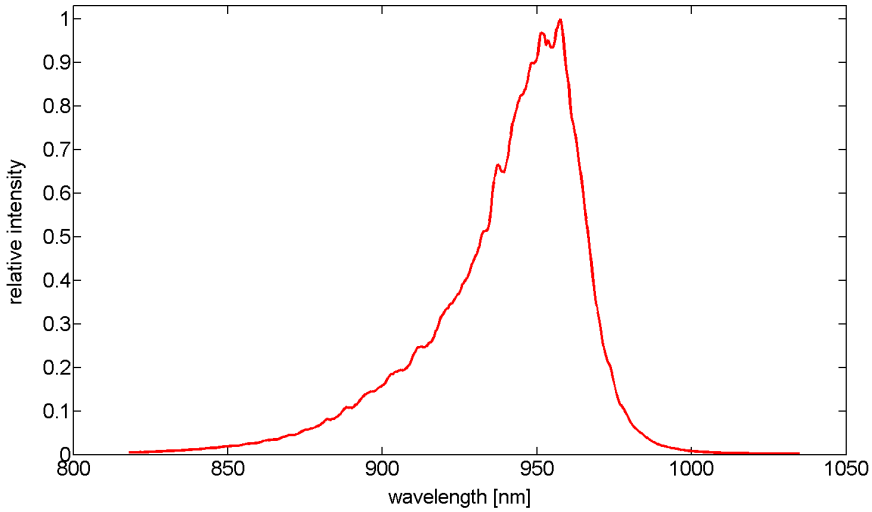

Figure 4.3: The radiation spectrum of the *Osram* SFH 4545 NIR-LEDs, measured with an *Ocean Optics Maya Pro* spectrometer.

Light Sources

The light sources are required to have:

- an infra-red emission peak wavelength close to 970 nm for effective suppression of upwelling light (see section 2.4.3)
- a high luminous density to resolve waves with high curvature (see section 4.2.2)
- a uniform directional characteristic in the field of view of the camera

Light emitting diodes (LEDs) provide high and efficient power output with a sufficiently narrow spectrum. After testing several candidate LEDs, it turned out that the requirement of a high luminous density was only met by the *Osram SFH 4545* LED. The specifications of the light sources that are used in the experimental setup are given in table 4.2. Figure 4.3 shows the radiation spectrum of the used LEDs. The penetration depth in water for light at the centroid wavelength 950 nm in water is about 3.4 cm (Kou et al., 1993).

Light Source Specifications	
Number of LEDs per array	90 / 350 (lab/field)
LED model	Osram SFH 4545
Current rating single LED	
- continuous mode	100 mA
- pulsed mode (2% duty factor)	1 A
Current rating array (pulsed mode)	8 A
Peak wavelength λ_{Peak}	940 nm
FWHM	36 nm
Array dimensions	15 x 322 mm / 33 x 550 mm (lab/field)
Penetration depth in water	3.4 cm (at 950 nm)

Table 4.2: Specifications of the light sources (LED arrays)

Each of the two light sources of the laboratory RSSG (figure 4.1) is built from 90 individual LEDs. In field setup, even 350 LEDs are used in each of the arrays. The use of extended light sources is necessary to ensure that reflections can be seen even in high curvature conditions. On the other hand, it limits the resolution and accuracy of the slope measurements, which only work if the origin of the light beam that is reflected is known. The compromise that was made in the new RSSG design is to have the light sources extended in one direction (the y-direction of the stereo base frame) and to measure only the slope component in the other direction (the x-direction). In the field setup, it is possible to automatically turn the acquisition unit to measure both downwind and crosswind components sequentially (see page 47).

The LED arrays are powered by a special LED controller (*Gardasoft* RT820F), which drives the LEDs at a selected current and allows for pulsing and triggering using the trigger signal from the frame grabber. Triggering and pulsing of the light sources is important for two reasons: (1) Pulsing allows "overdriving" the LEDs, at up to ten times the current rating for continuous use, and (2) triggering is necessary to synchronize the LED pulses with the cameras.

The trigger scheme for cameras and light sources is shown in figure 4.4. As described in section 3.1.2, stereo imaging requires that each camera only "sees" the opposite light source, so during acquisition of the left image, only the right light source can be powered and vice versa. The two images are acquired sequentially, separated by the exposure time of one image (0.2 ms). Of course the wave field cannot be allowed to change significantly between the acquisition of the left and right image, otherwise corresponding points (see section 3.1.2) could not be found in the images.

To ensure an optimum signal-to-noise ratio, the full dynamic range of the cameras should be used. Due to the large variability in reflection brightness described in section 4.2.2, using a bright light source will easily oversaturate images taken at lower wind speeds. Oversaturation may occur in field experiments when the wind speed is suddenly changing, but also in laboratory experiments when wind speed is continuously increased or decreased, as is done during

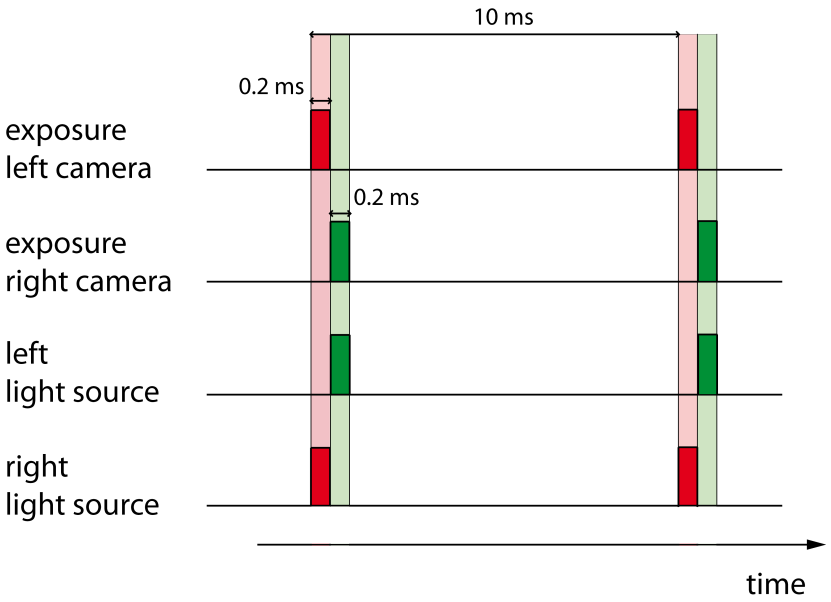

Figure 4.4: Trigger scheme for sequential image acquisition: The left camera and right light source are synchronized and vice versa.

some gas exchange measurements. Therefore, an adaptive control of the LED brightness was implemented, based on gray value histograms of the images.

Lenses and Filters

The focal length of the lenses is an important parameter for the RSSG. It determines the size of the footprint on the water surface – which should be large enough to resolve gravity waves – and the resolution for small structures – which has to be fine enough to resolve capillary waves.

In the RSSG, lenses with a focal length of 70 mm (*Schneider Kreuznach Tele-Xenar 2.2/70-0902*) are used. At the mean operating distance of 6 m, the total footprint is 87 cm x 72 cm, the resolution is 0.7 mm/pixel. To reduce background light, infrared filters with a cutoff wavelength of 850 nm (*B+W* infrared filter 093) are used. They effectively suppress light coming from the room illumination as well as from other experimental setups in the laboratory. They will possibly not be able to suppress direct reflections of sunlight during field experiments, but since experiments will be conducted at night, this is not a restriction.

If needed, the RSSG can be upgraded with filters that have a cutoff wavelength closer to the LED spectrum at 940 nm. Since sunlight in this spectral range is mostly absorbed by water vapor in the atmosphere, ambient light can be effectively suppressed.

Wind Adaptation

In laboratory wind wave facilities, the wind direction is known and constant at all times, and downwind and crosswind slopes can easily be measured separately. On a research vessel on the open ocean, the situation is more complex. The ship is usually aligned with the wind, its bow pointing upwind, to reduce distortions of the wind and wave field. However, the wind direction can change faster than the ship can be realigned. To continuously measure the downwind or crosswind component of the slope distribution, the RSSG has an integrated stepping motor that can rotate the acquisition unit consisting of cameras and LED arrays (see figure 4.2).

Wind direction (and speed) is measured with a *Young* anemometer installed close to the image acquisition system; the direction of the stereo base is adjusted on-line to adapt to changes in wind direction or to switch between the measurement of different slope components by a rotation of 90 degrees.

Data Acquisition System

In figure 4.5, a schematic of the data acquisition system is given. The whole process of data and image acquisition is controlled by the *heurisko* software on the measurement PC. The cameras are controlled by the frame grabber, which creates a trigger signal that is used not only for the cameras but also for the light sources. The light sources are powered with a special controller which can be programmed from the PC with an Ethernet link. Wind and ship inclination data is acquired from the anemometer and the inclination sensor (via a *Meilhaus* A/D USB interface). Wind data is used to set the parameters for the stepping motor which enables following the wind direction; ship inclination data (pitch and roll) is recorded for the evaluation of the slope measurements.

The advantage of controlling all devices from one software is obvious: it permits easy and on-line response to changing environmental conditions: If the wind direction changes, the stereo base can be rotated, so the RSSG continues to measure up- or crosswind slope; if the wind speed changes and e.g. creates more ripples, the brightness of the light sources can be increased to also resolve smaller structures.

4.1.2 The Aeolotron Wind Wave Facility

The laboratory RSSG setup was installed at the *Aeolotron* wind wave facility for test measurements and calibration. Figure 4.6 shows a drawing of the facility. The inner radius of the annular water channel is 4.34 m, the channel width is 62 cm. The water height is adjustable, it is 100 cm during normal operation.

The waves in the Aeolotron can usually be described in the *deep water wave* approximation (see 2.2.1). The deep water approximation is valid as long as the water depth is more than

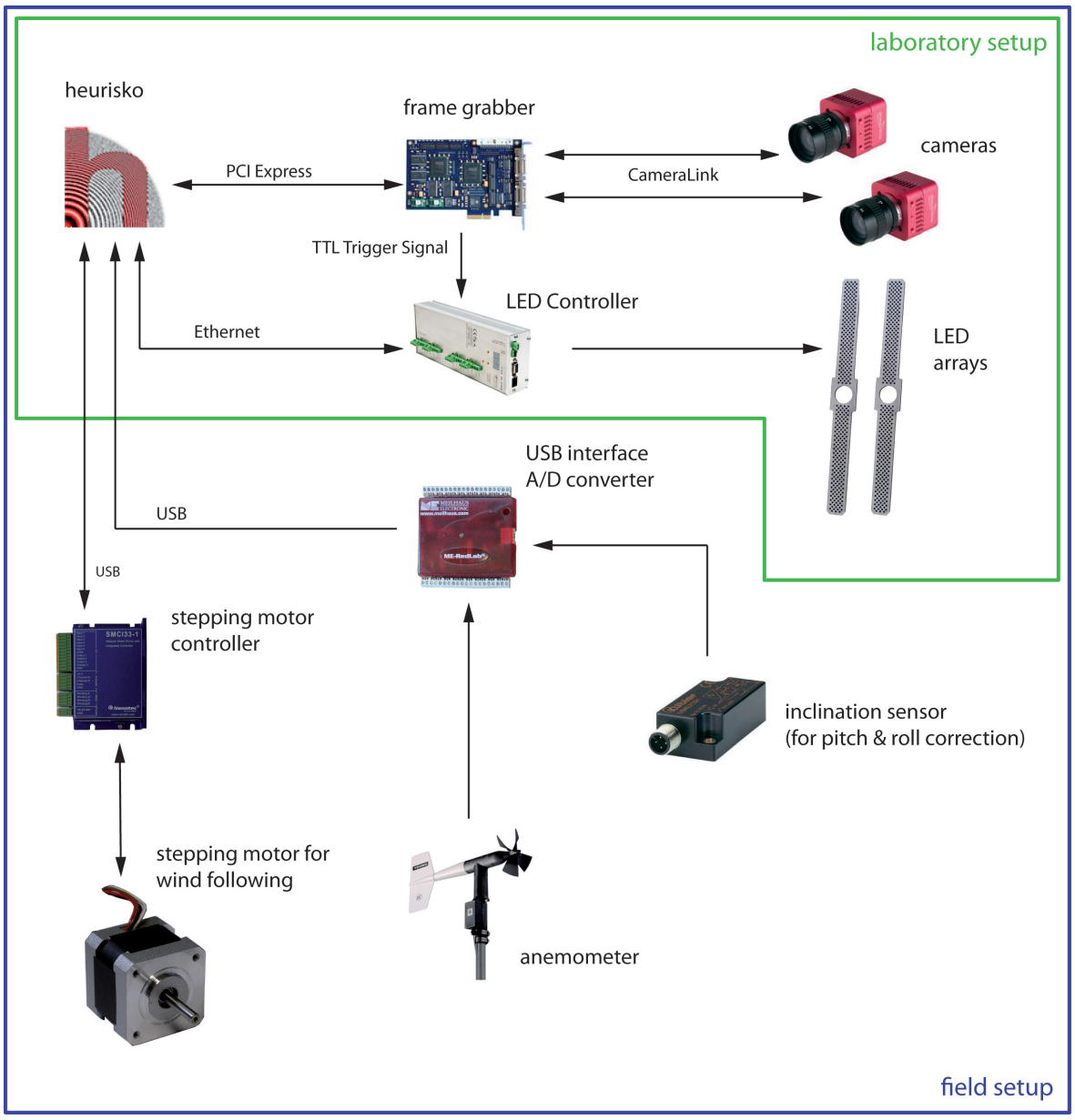

Figure 4.5: Schematic of the lab/field setup.

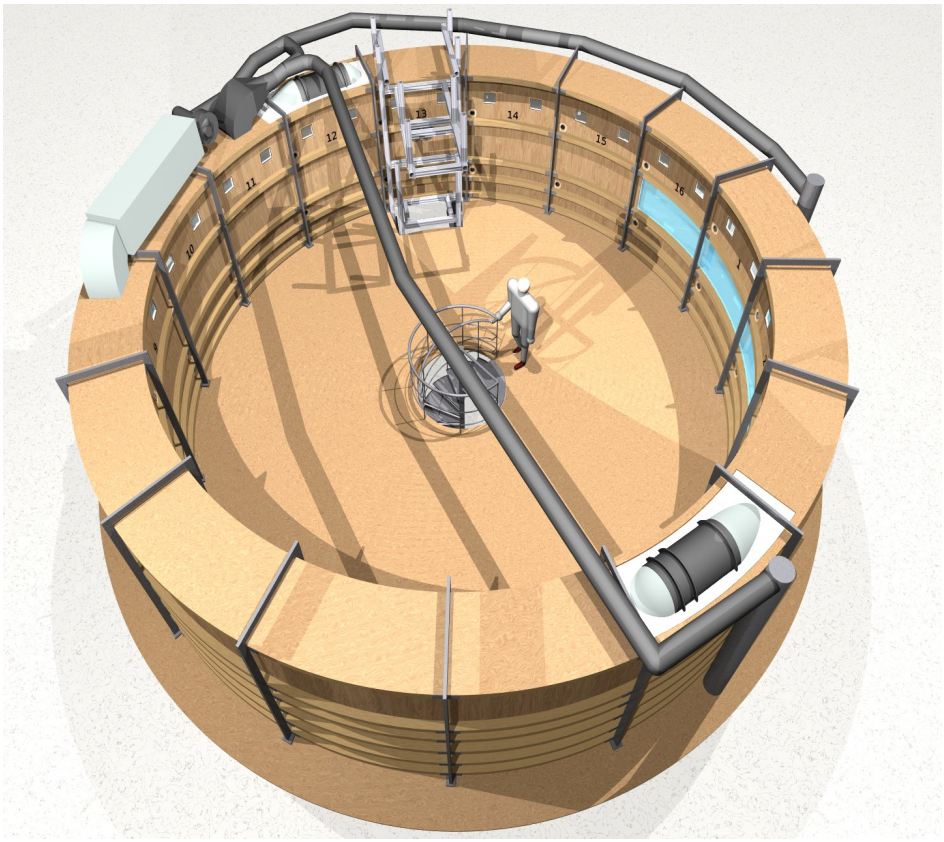

Figure 4.6: The Aeolotron wind wave facility, the largest active annular wind wave tank. Inner radius: 4.34 m. Channel width: 62 cm (from Richter, 2009).

28 % of the wavelength, which is corresponding to $\lambda \approx 3.60$ m in the Aeolotron. At the highest wind speeds, wavelengths can reach this range, the deep water approximation thus cannot completely describe the wave field. The longest waves begin to "see" the bottom of the water channel which increases wave breaking and limits the further growth of the waves.

Figure 4.7 show an illustration of the test setup with the laboratory RSSG. The mirror is needed to elongate the optical path between water surface and RSSG cameras. The distance between the cameras and the water surface is approximately 4.9 m. It was chosen to mimic the conditions of field experiments on research vessels. A glass window was installed in the ceiling of the Aeolotron to avoid disturbances of the wind and wave field and to allow simultaneous gas exchange and wave statistics measurements.

4.2 Image Simulation

Before a decision was made on the final design of the new RSSG, some properties of the planned system were simulated. A small ray tracing script was developed that can simulate the reflection images for given stereo camera setup parameters (relative camera positions, including stereo base length and camera tilt) and light source size and orientation. It is capable to simulate reflections from an arbitrary surface, provided that a two-dimensional

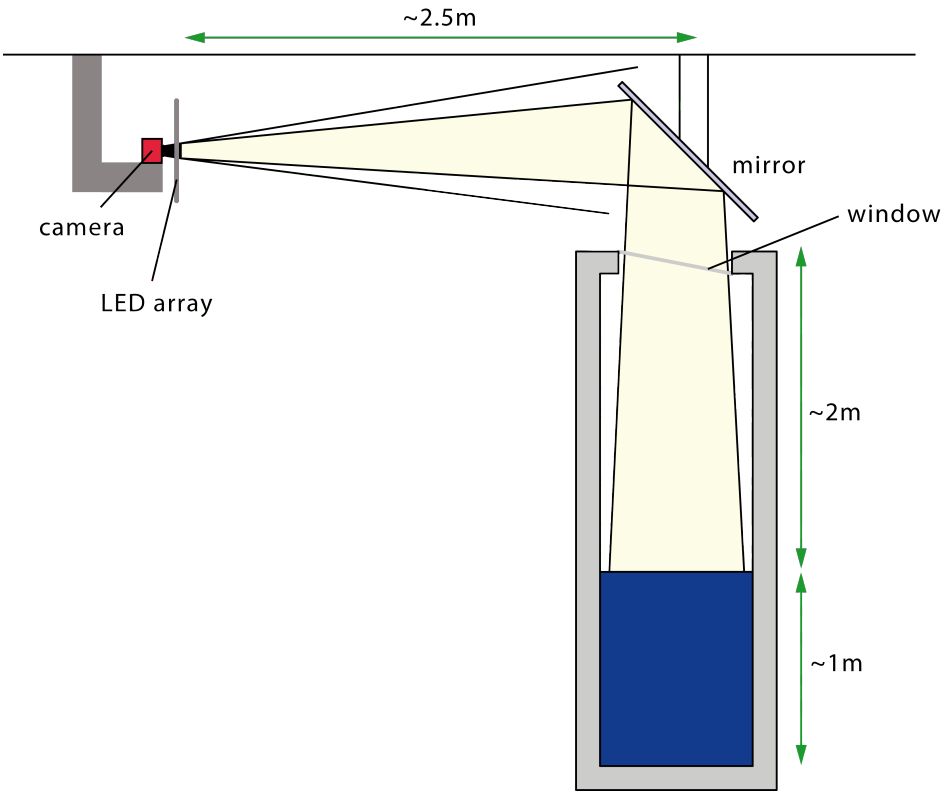

Figure 4.7: The RSSG installed at the Aeolotron. The illustration is not drawn to scale.

height map as well as two slope component maps are given. It accounts for the directional radiation characteristic and the extension of the light sources as well as the finite size of the aperture of the camera. The script traces light rays from the known light source positions to the water surface and determines, using the reflection condition, whether they are reflected into the camera aperture or not. The grid on the water surface can be selected with arbitrary precision depending on the desired application.

4.2.1 Consistency Check

A simulated sample image is presented in figure 4.8. It shows the reflection of the light source (consisting of 90 single LEDs) from a flat water surface in 6 m distance, as well as an actual image acquired with the RSSG under similar conditions. The images look alike, demonstrating the correct operation of the simulation tool. In the real image, the brightness of the individual LEDs seems to vary. This is mostly due to inhomogeneities in the LED directional characteristic (see section 4.3.1) and due to imperfect alignment of the LEDs in the light source aluminum frame.

4.2.2 Curvature Simulation

The curvature of the water surface produces lens effects and leads to brightness variations in the reflections (see figure 4.9). Negative curvature of the water surface defocuses an incident

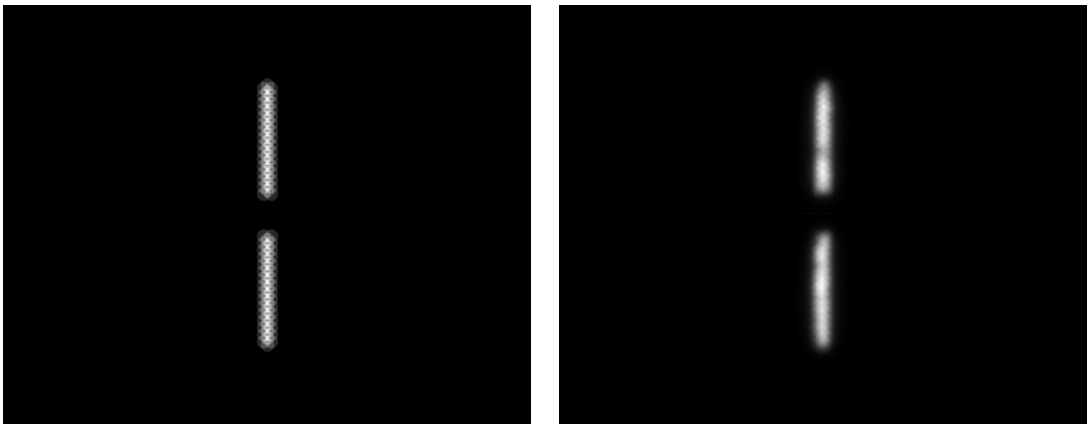

Figure 4.8: *Left:* Simulated image for flat water surface in 5.5 m distance.
Right: Actual image of flat water surface at Aeolotron in about the same distance for comparison. The simulated image agrees well with the actual image.

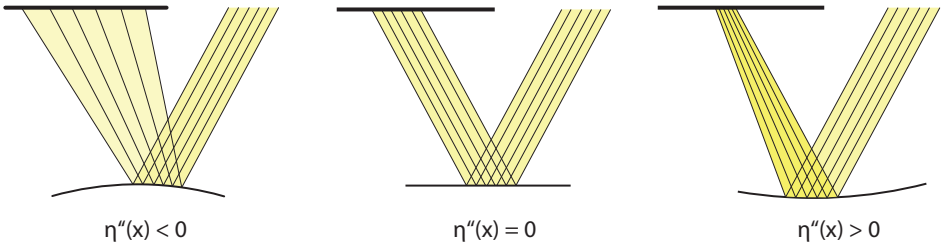

Figure 4.9: Lens effects due to surface curvature: A light beam that is reflected at a slightly curved surface is focused or defocused.

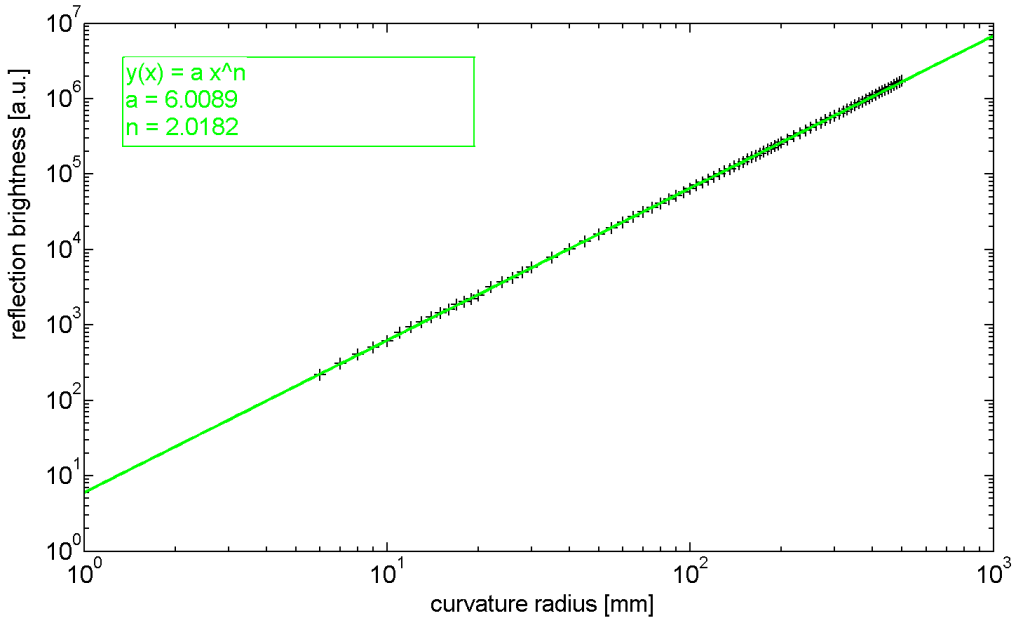

Figure 4.10: The simulated dependence of speckle brightness on surface curvature. Note the wide range of brightnesses that occur.

parallel light beam, which reduces speckle intensity. Positive curvature focuses a parallel beam. For very low positive curvatures, speckle intensity can be increased in the images due to this focusing. At higher curvatures however, the focal point lies close to the surface and far from the camera aperture. Behind the focal point, the rays are diverging and the speckle intensity in the images is reduced. This is a problem at higher wind speeds, when the water surface exhibits many turbulent regions and parasitic capillary waves. The reflecting patches here are small and can have high curvature. To investigate the influence of curvature on the brightness of reflections in the image, curved water surfaces were simulated. In the simulation, a surface was used that is shaped like a planoconvex lens floating on the water in 6 m distance, the lens radius was varied from 5 mm to 500 mm. Figure 4.10 shows the result of the simulations. The reflected brightness is clearly proportional to R^2, which seems reasonable, since brightness depends on the area from which light can be reflected into the camera.

If we assume sinusoidal waves on the water surface, the curvature of the surface is

$$\frac{\partial^2 \eta}{\partial x^2} = -ak^2 \sin(kx), \quad \frac{\partial^2 \eta}{\partial x^2} \approx \frac{1}{R}. \tag{4.1}$$

The RSSG "sees" points on the surface where the slope is close to zero, basically the maxima and minima (and saddle points) of the surface. The absolute value of the curvature is at maximum at these points (for sinusoidal waves). Thus $k = \sqrt{\frac{1}{aR}}$. A curvature radius of 5 mm is, assuming an amplitude of the order of 1 mm, equivalent to a wavenumber of the order $k = 450\,\frac{\mathrm{rad}}{\mathrm{m}}$, while a curvature radius of 500 mm corresponds to a wavenumber of the order $k = 4.5\,\frac{\mathrm{rad}}{\mathrm{m}}$ (assuming an amplitude of the order of 10 cm). These wavenumbers are well within

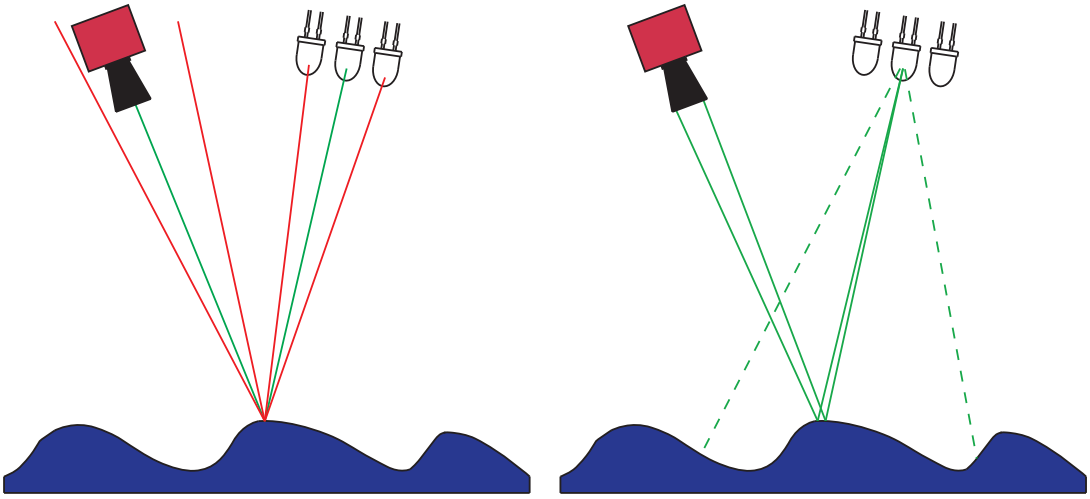

Figure 4.11: *Left*: Using multiple light sources at a specular reflecting surface cannot moderate inhomogeneities in the radiation characteristic efficiently.
Right: At a surface patch, only light coming from a small solid angle is reflected into the camera.

the limits of observable waves. Surface curvature leads to a high dynamic range of speckle brightness, which requires adaptive illumination brightness. At low wind speeds, when surface curvature is generally low, the brightness is reduced to prevent oversaturation of the images. At higher wind speeds, the brightness has to be increased to resolve high curvature reflections. This is possible because practically all reflections are coming from parasitic capillaries and other high curvature regions and high intensity reflections from relatively plane patches are unlikely. Still, one major challenge in designing the RSSG was to build sufficiently bright light sources to resolve small capillary waves.

4.3 Calibration of the RSSG

4.3.1 Illumination

Inhomogeneities

The RSSG derives statistics of the water surface from statistics of the speckle distribution in the images. Inhomogeneous illumination of the RSSG footprint leads to biased results for the speckle distribution that will affect the derived wave statistics. To achieve homogeneous illumination of a Lambertian surface, a large number of spatially distributed light sources can be used. The situation is more complex at a specularly reflecting surface. Figure 4.11 (left side) illustrates the problem. If the reflecting patch on the surface is sufficiently small, for a given surface slope only light coming from a single position is reflected into the camera, in this case, an extension of the light source is futile. The finite size of the aperture of the lens, however, weakens this condition, the area from which light is reflected into the camera for a given position and slope is the size of the aperture.

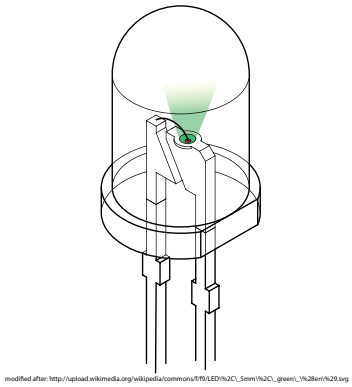

Figure 4.12: Inner construction of an LED: Light is emitted from the semiconductor die (*red*) at the center of the reflecting cavity (*green*).

A second problem for the illumination of the water surface is shown on the right side of figure 4.11: Out of the light cone emitted by a single light source, the camera "sees" only light emitted into a small solid angle. To achieve homogeneous illumination, the light sources are thus required to emit the same intensity in all directions – to have a constant directional characteristic.

The RSSG light sources are built from large number of individual infrared light emitting diodes (LEDs). Advantages of LEDs over conventional light sources include energy efficiency as well as a relatively narrow spectrum (which is important since the spectrum of the light sources has to be matched to a water absorption peak, see section 2.4.3). These advantages come at the cost of an asymmetric directional characteristic. Non-homogeneities are inherent, since the light emitting part of the diode itself is not rotation-symmetric. Figure 4.12 shows the inner construction of a typical single LED, similar to the type used in the RSSG LED arrays. The light emitting part, the semiconductor die, is directly connected to the anode from below, the cathode is connected with the center of the die by a thin metal wire reaching in from the side. This wire is breaking the rotation symmetry of the light emitter and thus of light emission itself.

The RSSG measurement principle is relating the probability for the occurrence of a given slope to the occurrence and brightness of reflections at only one position in the image. A reduced emission brightness in the direction of this position will thus directly lead to an underestimation of the probability of the corresponding slope.

To reduce the effect of inhomogeneities in the LED directional radiation characteristic in field experiments, holographic diffusors are added to the setup. Placed in front of the LED array, they diffuse the light coming from the LEDs while maintaining a sufficiently narrow lighted area. Standard diffusors made from opal glass typically have an almost Lambertian radiation characteristic, which would lead to the illumination of unwanted areas. The holographic diffusors that are used have narrow diffusing angles that are matched to the LED radiation half angle of 5°, and thus reduce light loss to a minimum.

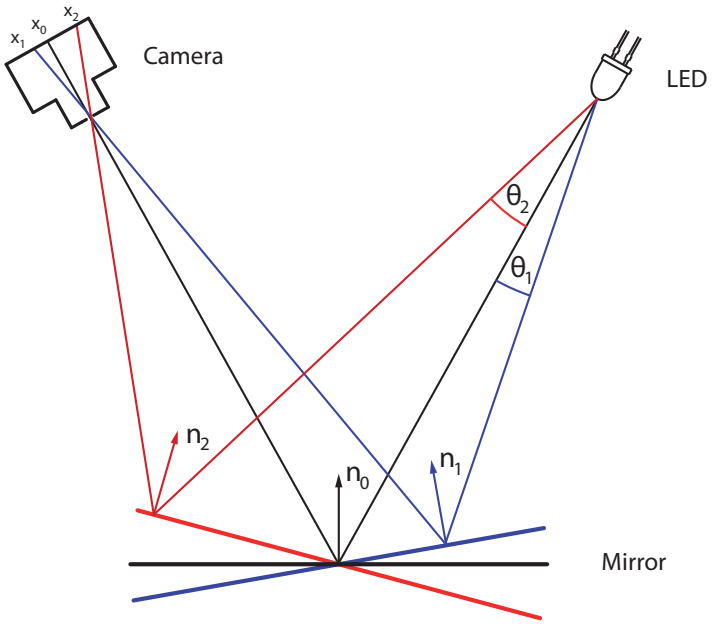

Figure 4.13: Schematic of the setup used to measure the directional characteristic of the LEDs.

Measuring the Directional Characteristic

If all the inhomogeneities of the light field are known, the intensity in the speckle images can be corrected and the influence on the measured slope probabilities can be minimized. Figure 4.13 shows a simplified one-dimensional schematic of the setup used for measuring the characteristic. To mimic experimental conditions, the mirror (or glass pane) that reflects the light from the LED into the camera is located at the height of the mean water level inside the Aeolotron wind-wave facility. The mirror can be tilted in arbitrary directions using a calibration robot with 3 step motors (Rocholz, 2008). Different mirror inclinations $\mathbf{n_i}$ lead to different positions $\mathbf{x_i}$ of the LED in the image and reflect light emitted into a different solid angle θ_i. The reflection brightness is extracted from the images and either the inclination information given by the step motor controller or the position of the reflections in the image can be used to determine the LED brightness as a function of the surface slope s_x, s_y.

Figure 4.14 shows the directional characteristic for a single LED. The directional characteristic for the LED array can be obtained from superposition of the distributions of single LEDs.

4.3.2 LED Intensity Calibration

The *Gardasoft* LED array controller allows setting LED brightness by controlling the current. The brightness of the LED is, however, not linearly dependent on the current. To measure the exact dependence of LED brightness on the driving current, an Ulbricht sphere was illuminated with one of the LEDs used in the RSSG arrays. The LEDs were pulsed with currents ranging from 0 to 1 A, which is equivalent to a range of 0 to 1000 % of the LED current rating for continuous use, and the emitted intensity was recorded with the RSSG cameras. The result of

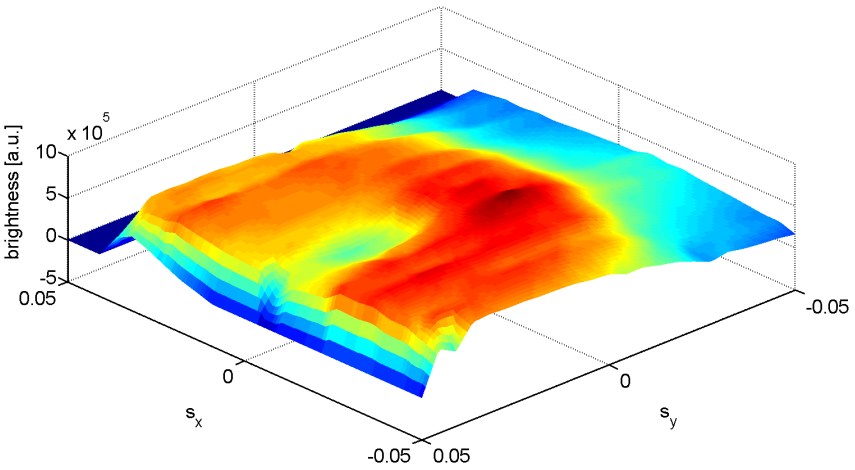

Figure 4.14: Directional characteristic of a single LED. The dip is likely caused by the cathode wire, see figure 4.12.

this calibration is plotted in figure 4.15. Clearly, for higher currents the curve is significantly deviating from a linear characteristic. If this were not accounted for, reflection brightness would be underestimated in high wind speed conditions.

4.3.3 Stereo Calibration

Stereo images contain information about object distance, coded in parallax magnitude and orientation. In order to convert parallax into distance, the dependence of parallax on distance needs to determined. This was done by geometric considerations in section 3.3, under the assumption that the exact geometry of the stereo setup is known. In the Aeolotron however, the distance between the camera and the mean water level that is used as the reference height Z_0 (see 3.3) cannot be measured accurately. The distance can, on the other hand, be determined with a two-point measurement: Equation (3.18) gives the water height as a function parallax p, stereo reference height Z_0, stereo base b, focal length f and image position of the reflection u. The parallax can be determined for two different water heights in the Aeolotron Z_1 and $Z_1 + \Delta Z$; the difference ΔZ is easily measured. With these two data points, the stereo reference height can be determined from equation (3.18).

To reduce errors in the measurement, longer data series were recorded. The cameras were aligned so that the images overlapped at (i.e. the stereo reference height was equivalent to) an Aeolotron water height of 605 mm. The water height was varied between 1000 mm and 300 mm and the parallax was determined for a number of water heights. The procedure was repeated for a stereo reference height equivalent to a water height of 990 mm. The black crosses in figure 4.16 are the determined parallaxes at the corresponding water heights. The green lines are fits of the parallax-height function (3.14), with the stereo reference height as a fit parameter. Table 4.3 summarizes the fit results. The difference in the determined stereo

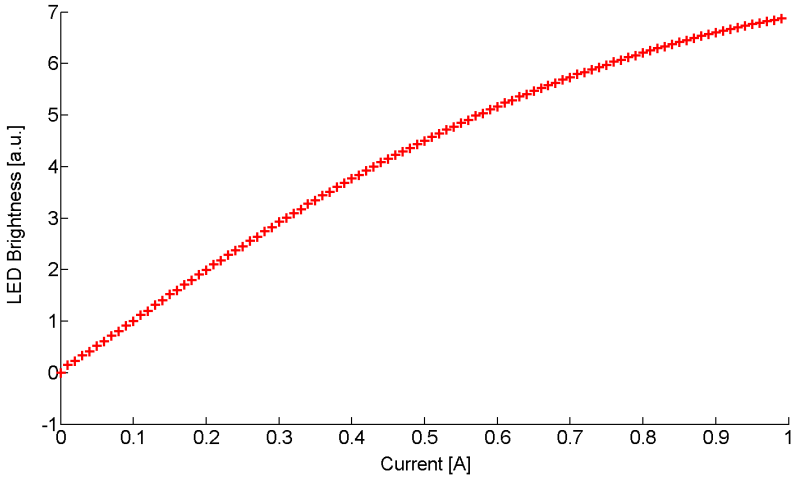

Figure 4.15: The brightness-current dependency of the OSRAM SFH 4545 LEDs.

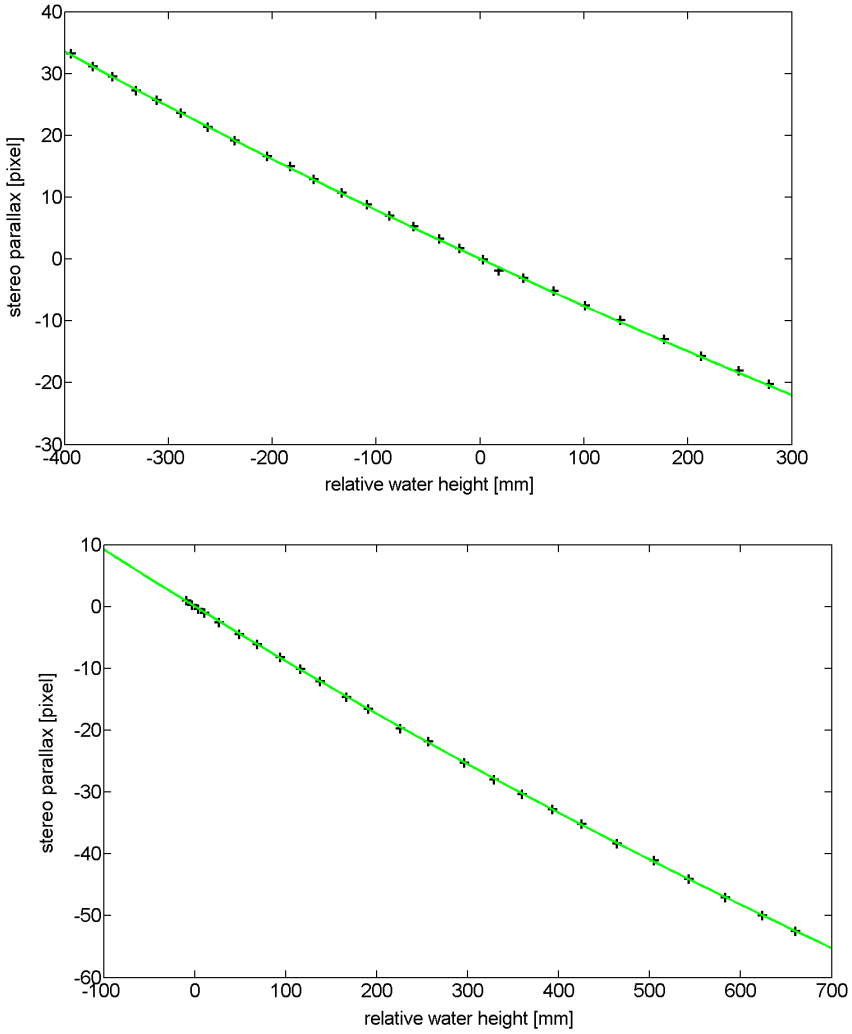

Figure 4.16: Results from two stereo calibration runs. The reference height was set to water levels of 605 mm (*top*) and 990 mm (*bottom*).

	water height [mm]	determined reference height [mm]
run 1	990	4872.9
run 2	605	5257.9
difference	385	385.0

Table 4.3: Results for the experimental determination of the camera-water distance at the Aeolotron.

reference heights is equal to the difference in the Aeolotron water heights. An important result is that the distance of the cameras to the mean water level at 100 cm water height, that is the water height usually used in gas exchange experiments in the Aeolotron is 4.862 m. This value is used for the calibration of the slope measurements.

5 Data Evaluation

Digital images can be described as $M \times N$ matrices G, where M is the number of pixels in the y-direction and N is the number of pixels in the x-direction. The entries g_{ij} of such an image G are commonly named *gray values*. In raw images, gray values are positive integers and their range is determined by the resolution of the analog/digital converter of the used camera. The converter of the RSSG cameras has a resolution (or *bit depth*) of 12 bits, as a consequence gray values range between 0 and 4095. During image processing, it is more convenient to treat gray values as floating point numbers and to allow them to become negative.

The RSSG acquires 200 speckle images per second of operation. From these images, slope and height data can be reconstructed. Due to the huge amount of data that is recorded, automated image processing algorithms are needed. In this section, the data evaluation principle is explained and image processing algorithms are described.

5.1 Preprocessing During Acquisition

The raw image data acquired by the RSSG during normal operation amounts to 540 MB/s (or about 1.8 TB/h). With today's storage possibilities, this is not feasible for a two week measurement campaign on a research vessel or extensive laboratory measurements. Also, since writing data to hard drives is slow, the overall rate of image acquisition drops tremendously if all this data needs to be saved. However, due to the special characteristics of the images, the data size can be significantly reduced with simple image processing operations that can be performed on-line during measurements.

A flow chart of the preprocessing routine is given in figure 5.1. In a first step, artifacts from the readout electronics of the image sensor are removed by the subtraction of a *dark image*. All pixels that contain no information (i.e. *background* pixels) are ideally set to a gray values of 0 by this operation. In real images, noise causes the gray values to scatter around this value.

The information density in the reflection images is relatively low, that is, only a small fraction of the image is covered with speckles. By definition, the background contains no information, it does not need to be saved. The separation of pixels with gray values that contain information (i.e. pixels that belong to *objects*) from *background* pixels is called *segmentation*. The segmentation is usually stored as a binary image, i.e. in the form of a matrix with entries 0 (for background pixels) and 1 (for object pixels). There are many different strategies

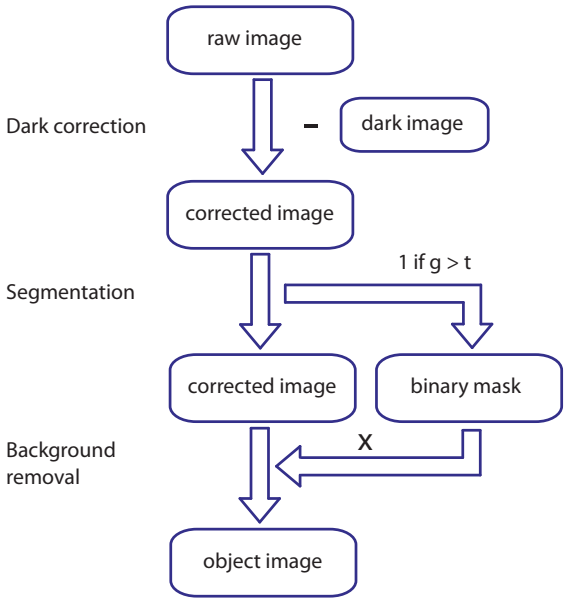

Figure 5.1: Raw image preprocessing: After dark image correction, a global threshold is applied to the image and background is removed.

and algorithms to determine whether a pixel belongs to an object or to the background, an introduction is given by Jähne (2005).

In the RSSG reflection images, the bright reflections can be separated from the dark background by applying a global threshold t. This produces a binary image B with entries

$$b_{ij} = \begin{cases} 1 & g_{ij} > t, \\ 0 & g_{ij} \leq t. \end{cases} \tag{5.1}$$

The level of the threshold has to be set sufficiently high to prevent *false positive* segmentations of noisy background pixels. On the other hand, a high threshold increases the probability of *false negatives*, i.e. speckle pixels with low brightness that are mistaken to be background pixels. In the laboratory experiments described in chapter 6, the threshold was set to approximately three times the standard deviation of background noise.

The background is removed from the images by element-wise multiplication of the image with the segmentation mask; all background pixels are thereby set to gray value 0. The resulting object image can effectively be compressed with the lossless LZW algorithm. The basic idea of the compression algorithm is to use dictionaries in which repeating data patterns are replaced by a short number[1]. In the preprocessed object images, most of the pixels are set to 0, so patterns with gray values (0,0,0,0,...) will appear often. The compression can reduce the file size by a factor greater than 20.

[1]for further information see http://partners.adobe.com/public/developer/en/tiff/TIFF6.pdf

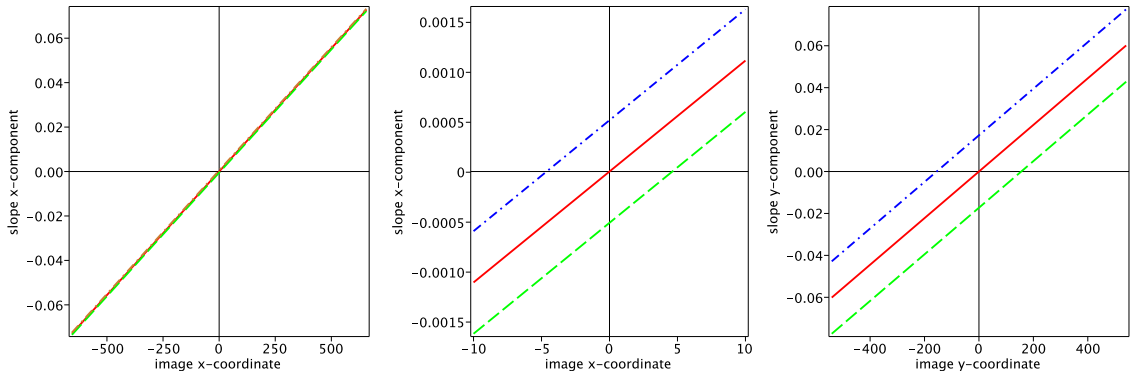

Figure 5.2: The slope-position function for x- and y-coordinates of the image (coordinate system is shifted so that the center pixel of the image is at 0,0). The three lines represent the maximum, "mean", and minimum slope that is visible at the respective image coordinates. An effect in the x-direction is only visible in the magnified detail (middle figure), note the different scale of the abscissa. The small angle approximation was not used to obtain these curves.

5.2 Slope Statistics Reconstruction

5.2.1 Finite-sized Light Source

In chapter 3.2, the surface slope that is corresponding to reflections in the image was computed. For a given water height, a unique slope can be assigned to each pixel of the image. The probability for the occurrence of this slope is directly correlated with the occurrence of a reflection in this pixel.

This strict condition was derived for point light sources. The RSSG, uses extended, finite-sized, light sources. The slope that leads to a reflection at a certain pixel is not unique anymore, light coming from different parts of the light source is reflected into the camera if the surface slope is within the slope interval

$$\mathbf{s} \pm \delta\mathbf{s} = \mathbf{s} \pm \begin{bmatrix} \delta s_\mathrm{x} \\ \delta s_\mathrm{y} \end{bmatrix} = \mathbf{s} \pm \begin{bmatrix} L_\mathrm{x}/2z \\ L_\mathrm{y}/2z \end{bmatrix}, \tag{5.2}$$

where L_x and L_y are the dimensions of the light source in the respective directions. The last identity in equation (5.2) follows from geometric considerations using the small angle approximation for the surface tilt angle θ.

In figure 5.2, the slope range that is visible when the small Aeolotron light sources are used is plotted. The RSSG light source dimensions are asymmetric, see figure 4.1, the extension of the visible slope range is pronounced in the y-direction of the image only, in the x-direction (i.e. parallel to the stereo base) it is practically negligible. As can be seen from figure 5.2, the last identity in (5.2) that was obtained using a linear approximation is sufficient to describe the visible slope range.

The effect of the finite-dimension light sources on the probability of reflections in the images may be described mathematically as a convolution of the slope probability density function $p(s_x, s_y)$ with the light source function $l(s_x, s_y)$. This convolution is described by the following integral:

$$p^*(s_x, s_y) = \iint_{-\infty}^{\infty} p(s'_x, s'_y)\, l(s'_x - s_x, s'_y - s_y)\, \mathrm{d}s'_x\, \mathrm{d}s'_y, \tag{5.3}$$

where

$$l(s_x, s_y) = \begin{cases} 1 & \text{for } |s_x| < \delta s_x \text{ and } |s_y| < \delta s_y, \\ 0 & \text{else.} \end{cases} \tag{5.4}$$

Even under ideal experimental conditions (stationary wave field, infinite observation time), the speckle distribution is not proportional to the slope PDF $p(s_x, s_y)$, but to the convoluted $p^*(s_x, s_y)$. The convolution kernel (the light source function l) has a size of $\delta s_x = 0.00056$, $\delta s_y = 0.0172$. This size sets the limit to the resolution of the PDF measurement.

5.2.2 Probability Distribution of Small Slopes

In the Aeolotron laboratory setup, the RSSG can measure the slope component in the x-direction in the range $s_x = \pm - 0.07$, in the y-direction in the range $s_y = \pm 0.06$[2]. For all but the lowest wind speeds, the RSSG is imaging only a small fraction of the slope PDF which is centered around slope zero. The general slope PDF can be described by the Cox & Munk (CM) Gram-Charlier expansion given in equation (2.33):

$$\begin{aligned} p(s_x^*, s_y^*) = \frac{1}{2\pi\sigma_x\sigma_y} \exp(-\frac{1}{2}(s_x^{*2} + s_y^{*2})) \Big[1 - \frac{1}{2}c_{21}(s_x^{*2} - 1)s_y^* - \frac{1}{6}c_{03}(s_y^{*3} - 3s_y^*) \\ + \frac{1}{24}c_{40}(s_x^{*4} - 6s_x^{*2} + 3) + \frac{1}{4}c_{22}(s_x^{*2} - 1)(s_y^{*2} - 1) + \frac{1}{24}c_{04}(s_y^{*4} - 6s_y^{*2} + 3). \end{aligned} \tag{5.5}$$

In the measurement range of the RSSG, as long the assumptions $s_x \ll \sigma_x$ and $s_y \ll \sigma_y$ are fulfilled, the Gaussian in (5.5) can be approximated by a parabola (Taylor expansion up to quadratic order):

$$g(s_x, s_y) = \frac{1}{2\pi\sigma_x\,\sigma_y} \left(1 - \frac{{s_x}^2}{2{\sigma_x}^2} - \frac{{s_y}^2}{2{\sigma_y}^2}\right) + O(|\mathbf{s}|^3). \tag{5.6}$$

If equation (5.6) is used to describe the slope PDF $p(s_x, s_y)$, skewness and peakedness of the distribution, originating in non-linear wave-wave interactions, are neglected. Looking at the CM parametrization evaluated at zero slope,

$$p(0,0) = \frac{1}{2\pi\sigma_x\sigma_y} \left(1 + \frac{1}{8}c_{40} + \frac{1}{8}c_{04} - \frac{1}{4}c_{22}\right), \tag{5.7}$$

[2] In the field, this range is extended by the ship's pitch and roll.

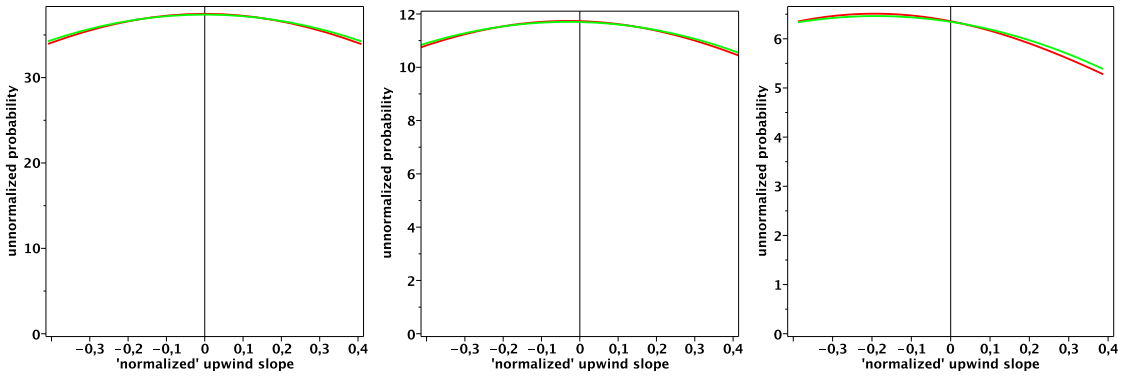

Figure 5.3: Comparison of the CM Gram-Charlier expansion (up-/downwind direction, *red*) and the approximation in 5.8 (*green*) for wind speeds (from left to right) 1 m/s, 5 m/s, and 10 m/s.

it is obvious that peakedness terms lead to an increase of the PDF amplitude for small slopes. The peakedness coefficients given by CM are $c_{40} = 0.3$, $c_{04} = 0.4$, and $c_{22} = 0.12$ (Cox and Munk, 1954a), independent of wind speed[3]. The peakedness term thus increases the amplitude of $p(0,0)$ by 5.75 % compared to a pure Gaussian. Since the reflection probability in the RSSG images will only be proportional to the slope PDF, the peakedness term can be absorbed by the overall proportionality constant.

Skewness causes asymmetry of the slope PDF and leads to a shift of the maximum, away from 0. The latter effect can be accounted for, the asymmetry of the distribution is neglected in this approximation. The approximated PDF $\tilde{p}(s_\mathrm{x}, s_\mathrm{y})$ thus becomes

$$\tilde{p}(s_\mathrm{x}, s_\mathrm{y}) = \frac{1}{2\pi\sigma_\mathrm{x}\,\sigma_\mathrm{y}} \left(1 - \frac{(s_\mathrm{x} - s_{\mathrm{x},0})^2}{2{\sigma_\mathrm{x}}^2} - \frac{{s_\mathrm{y}}^2}{2{\sigma_\mathrm{y}}^2}\right). \tag{5.8}$$

In figure 5.3 the approximated PDF is compared to the CM Gram-Charlier distribution, in the slope range that is visible to the RSSG: At very low wind speeds, σ_x and σ_y are small, the assumptions $s_\mathrm{x} \ll \sigma_\mathrm{x}$ and $s_\mathrm{y} \ll \sigma_\mathrm{y}$ are no longer valid for the image borders and deviations of the approximated PDF increase. At higher wind speeds, the influence of distribution skewness increases and the fit quality decreases.

[3]The Cox-Munk-parametrization was obtained from fitting ocean data and it is doubtful if it can describe laboratory data from the Aeolotron. However, in this approximation, a peakedness correction that is not dependent on wind speed is assumed, then the exact magnitude of the correction is irrelevant.

5.2.3 Extraction of the Mean Square Slope

In equation (5.3) the effect of the finite size of the light source on the relation between the slope PDF and the reflection PDF was described by a convolution. For the approximated PDF from equation (5.8), the convolution integral becomes:

$$\begin{aligned} p^*(s_\mathrm{x}, s_\mathrm{y}) &= \int_{-\infty}^{\infty}\!\!\int \tilde{p}(s'_\mathrm{x}, s'_\mathrm{y})\, l(s'_\mathrm{x} - s_\mathrm{x}, s'_\mathrm{y} - s_\mathrm{y})\, \mathrm{d}s'_\mathrm{x}\, \mathrm{d}s'_\mathrm{y} \\ &= \frac{1}{2\pi\sigma_\mathrm{x}\,\sigma_\mathrm{y}} \int_{\mathbf{s}-\delta\mathbf{s}}^{\mathbf{s}+\delta\mathbf{s}}\!\!\int 1 - \frac{(s'_\mathrm{x} - s'_{\mathrm{x},0})^2}{2{\sigma_\mathrm{x}}^2} - \frac{{s'_\mathrm{y}}^2}{2{\sigma_\mathrm{y}}^2}\, \mathrm{d}s'_\mathrm{x}\, \mathrm{d}s'_\mathrm{y} \\ &= \frac{2\delta s_\mathrm{x}\delta s_\mathrm{y}}{\pi\sigma_\mathrm{x}\sigma_\mathrm{y}} \left(1 - \frac{(s_\mathrm{x} - s_{\mathrm{x},0})^2}{2\sigma_\mathrm{x}^2} - \frac{s_\mathrm{y}^2}{2\sigma_\mathrm{y}^2} - \frac{\delta s_\mathrm{x}^2}{6\sigma_\mathrm{x}^2} - \frac{\delta s_\mathrm{y}^2}{6\sigma_\mathrm{y}^2}\right) \end{aligned} \tag{5.9}$$

Since the cubic terms all cancel out, the resulting $p^*(s_\mathrm{x}, s_\mathrm{y})$ is still a parabola, which is reasonable, since the extended (homogeneous) light source should only spread out and smoothen the distribution. Ideally, i.e. for infinite observation time and stationary conditions, the gray value distribution in the images should be proportional to $p^*(s_\mathrm{x}, s_\mathrm{y})$.

To reduce the statistical error (which is inevitable for finite observation times), it is desirable to average the gray value distribution over a larger portion of the image. Mathematically this is equivalent to integrating $p^*(s_\mathrm{x}, s_\mathrm{y})$ over the desired slope range. In the s_y-direction this yields

$$\begin{aligned} p_\mathrm{x}(s_\mathrm{x}) &= \int_{s_{\mathrm{y},1}}^{s_{\mathrm{y},2}} p^*(s_\mathrm{x}, s_\mathrm{y})\mathrm{d}s_\mathrm{y} \\ &= \frac{2\delta s_\mathrm{x}\delta s_\mathrm{y}}{\pi\sigma_\mathrm{x}\sigma_\mathrm{y}} \left[(s_{\mathrm{y},2} - s_{\mathrm{y},1}) \left(1 - \frac{(s_\mathrm{x} - s_{\mathrm{x},0})^2}{2\sigma_\mathrm{x}^2} - \frac{\delta s_\mathrm{x}^2}{6\sigma_\mathrm{x}^2} - \frac{\delta s_\mathrm{y}^2}{6\sigma_\mathrm{y}^2}\right) - \frac{(s_{\mathrm{y},2}^3 - s_{\mathrm{y},1}^3)}{6\sigma_\mathrm{y}^2}\right] \end{aligned} \tag{5.10}$$

while in the s_x-direction it gives

$$\begin{aligned} p_\mathrm{y}(s_\mathrm{y}) &= \int_{s_{\mathrm{x},1}}^{s_{\mathrm{x},2}} p^*(s_\mathrm{x}, s_\mathrm{y})\mathrm{d}s_\mathrm{x} \\ &= \frac{2\delta s_\mathrm{x}\delta s_\mathrm{y}}{\pi\sigma_\mathrm{x}\sigma_\mathrm{y}} \left[(s_{\mathrm{x},2} - s_{\mathrm{x},1}) \left(1 - \frac{s_\mathrm{y}^2}{2\sigma_\mathrm{y}^2} - \frac{s_{\mathrm{x},0}^2}{2\sigma_\mathrm{x}^2} - \frac{\delta s_\mathrm{x}^2}{6\sigma_\mathrm{x}^2} - \frac{\delta s_\mathrm{y}^2}{6\sigma_\mathrm{y}^2}\right) + \frac{s_{\mathrm{x},0}(s_{\mathrm{x},2}^2 - s_{\mathrm{x},1}^2)}{2\sigma_\mathrm{x}^2} - \frac{(s_{\mathrm{x},2}^3 - s_{\mathrm{x},1}^3)}{6\sigma_\mathrm{x}^2}\right] \end{aligned} \tag{5.11}$$

Some simplifications to these distributions can be made with reasonable approximations. First of all, since $s_{\mathrm{x/y},1/2} \ll 1$, $s^3_{\mathrm{x/y},1/2}$ is very small and the first term in the brackets of both (5.10) and (5.11) can be neglected. Furthermore, the second term in (5.11) vanishes identically as long as a symmetric interval is used in the integration.

There are several strategies to extract the mean square slope from this distribution, two of which will be presented in the following paragraphs.

Mean Gray Value

Integrating (5.11) in the s_y-direction, which is, together with the integration in (5.11), equivalent to averaging over all the gray values in two-dimensional region of the image, and applying approximations equivalent to those described above, one gets[4]

$$G = \frac{2\delta s_x \delta s_y \Delta s_x \Delta s_y}{\pi \sigma_x \sigma_y} \left(1 - \frac{s_{x,0}^2}{2\sigma_x^2} - \frac{\delta s_x^2}{6\sigma_x^2} - \frac{\delta s_y^2}{6\sigma_y^2}\right). \tag{5.12}$$

If all but the last of the terms in the brackets can be neglected, then $G \propto \frac{1}{\sigma_x \sigma_y}$ from which the mean square slope can be estimated. The second and third term in (5.12) are consequences of the finite size of the light source. As long as $\delta s_{x/y}^2 \ll 6\sigma_{x/y}^2$, they can be neglected. In the critical y-direction, for the small light source in the Aeolotron setup, $\delta s_y = 0.017$. Even at near zero wind speed, rms slope is of the order $\sigma_{x/y} \approx 0.03$ (Bréon and Henriot, 2006; Cox and Munk, 1954b), thus the approximation is reasonable and the error introduced by neglecting the term should be small. The dimension of the light source in the x-direction is negligible. The first term in (5.12) is a consequence of the non-linear wave-wave interaction and the skewness[5] of the slope PDF. At low wind speeds, the shift of the maximum due to distribution peakedness that is modeled with $s_{x,0}$ is near zero and experimentally it is found (Bréon and Henriot, 2006), that $s_{x,0}$ increases slower than σ_x, so $s_{x,0}^2$ is negligible to a good approximation.

Under these approximations, the mean gray value of the image is proportional to the product of the root mean square (rms) slope components $G \propto \frac{1}{\sigma_x \sigma_y}$. Writing $\epsilon := \frac{\sigma_x}{\sigma_y}$, the mean square slope can be obtain from the rms component product using

$$\sigma_x \sigma_y = \frac{1}{\epsilon}\sigma_x^2 \quad \text{and} \quad \sigma_x \sigma_y = \epsilon \sigma_y^2, \tag{5.13}$$

so that the total mean square slope is

$$\sigma^2 = \sigma_x^2 + \sigma_y^2 = (\epsilon + \frac{1}{\epsilon})\sigma_x \sigma_y \propto \frac{\epsilon + 1/\epsilon}{G}. \tag{5.14}$$

The value of $\epsilon + 1/\epsilon$ is experimentally found to be almost independent of wind speed both in ocean measurements and only slightly dependent on wind speed in laboratory measurements (see figures 5.4,5.5). Thus, at least relative values for σ^2 can be derived from the mean gray value to a good approximation.

This last approximation can be avoided if not only the mean gray value of the image is used, but also the distribution of the gray values is taken into account. This approach is described in the next section.

[4] Here, $\Delta s_{x/y} = (s_{x/y,2} - s_{x/y,1})$.

[5] The skewness is only modeled with this shift of the maximum, since the approximated PDF used here is symmetric about its maximum.

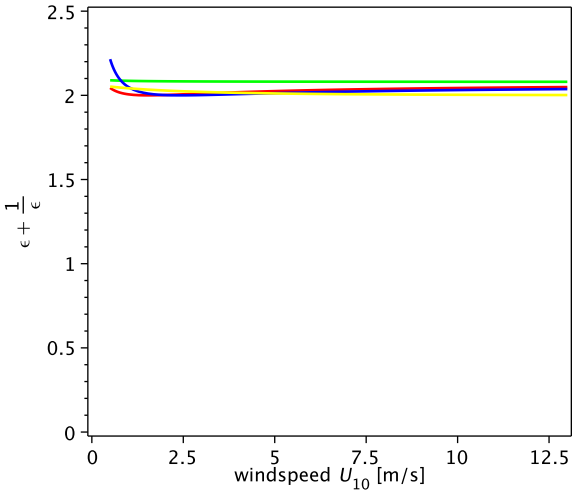

Figure 5.4: The dependence of $\epsilon + 1/\epsilon$ on wind speed U. Data is from Cox and Munk (1954b) (both clean and slick parametrizations), Hughes et al. (1977), and Bréon and Henriot (2006). Clearly, the factor is almost independent of wind speed for all parametrizations.

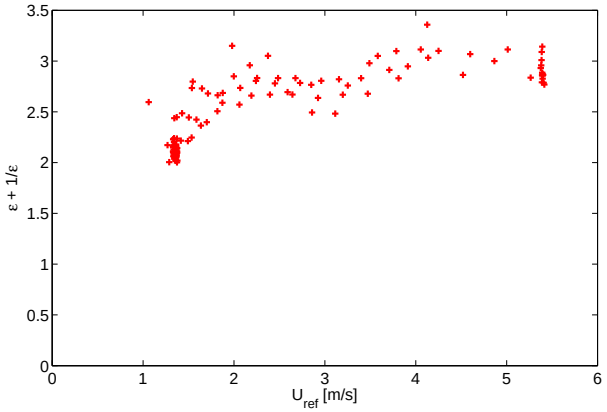

Figure 5.5: The dependence of $\epsilon + 1/\epsilon$ on wind speed U. Data from CISG measurements at the Aeolotron wind wave facility, Rocholz (2010).

Fitting the Curvature

Equation (5.10) describes the distribution of gray values that is obtained by averaging over the y-coordinate of the image. By fitting a parabola of the form $a_0(x-x_0)^2+a_1$ to this distribution, the fitting parameters a_0 and a_1 can be used to extract both rms slope components and thus the mean square slope:

$$\begin{aligned} p_{\mathrm{x}}(s_{\mathrm{x}}) &= -\frac{\delta s_{\mathrm{x}}\delta s_{\mathrm{y}}\Delta s_{\mathrm{y}}}{\pi\sigma_{\mathrm{x}}^3\sigma_{\mathrm{y}}}\,(s_{\mathrm{x}}-s_{\mathrm{x},0})^2 + \frac{2\delta s_{\mathrm{x}}\delta s_{\mathrm{y}}\Delta s_{\mathrm{y}}}{\pi\sigma_{\mathrm{x}}\sigma_{\mathrm{y}}}\,\left(1-\frac{\delta s_{\mathrm{x}}^2}{2\sigma_{\mathrm{x}}^2}-\frac{\delta s_{\mathrm{y}}^2}{2\sigma_{\mathrm{y}}^2}\right), \\ a_0 &= -\frac{\delta s_{\mathrm{x}}\delta s_{\mathrm{y}}\Delta s_{\mathrm{y}}}{\pi}\,\frac{1}{\sigma_{\mathrm{x}}^3\sigma_{\mathrm{y}}}, \\ a_1 &= \frac{2\delta s_{\mathrm{x}}\delta s_{\mathrm{y}}\Delta s_{\mathrm{y}}}{\pi\sigma_{\mathrm{x}}\sigma_{\mathrm{y}}}\,\left(1-\frac{\delta s_{\mathrm{x}}^2}{2\sigma_{\mathrm{x}}^2}-\frac{\delta s_{\mathrm{y}}^2}{2\sigma_{\mathrm{y}}^2}\right) \end{aligned} \tag{5.15}$$

By making the same assumptions as in the preceding section, the mean square slope can be extracted from a_1 (which is the amplitude of the maximum of the parabola at x_0). The $s_{\mathrm{x},0}^2$ term from (5.12) does not appear here, so in theory this extraction should be more accurate. In practice however, statistical noise is suppressed more efficiently when integrating over both directions, favoring the approach described in the last section. With $1/\sigma_{\mathrm{x}}\sigma_{\mathrm{y}}$ known, the x-component of the mean square slope, σ_{x}^2 can easily be determined from a_0, then of course also σ_{y} and the mean square slope can be computed without making any assumptions on $\epsilon+1/\epsilon$.

There is another way of determining σ_{x} from the two coefficients. Without making any further approximations and thus including the terms reflecting the finite dimension of the light source, the (nonlinear) equation system of the last two lines in (5.15) can be solved numerically to directly yield σ_{x} and σ_{y}.

It is important to keep in mind that for this approach to work it is critical that the gray value distribution in the image depends only on reflection probability. This requires that the illumination is homogeneous and vignetting does not occur. The values for σ_{x} and σ_{y} rely heavily on the extrapolation of the PDF to higher slope values and are not directly computed from measurement data.

5.2.4 Implementation of the image processing algorithm

For the evaluation of the test measurements at the Aeolotron, an algorithm using the mean gray value method described above was implemented. The motivation for using this approach is the reduced sensitivity to inhomogeneities of the illumination. The light source that will be used in future field experiments has added diffusors which remove most inhomogeneities (see section 4.1). This will allow the application of the more precise curvature fitting method.

A flow chart of the image processing algorithm used to evaluate the data from the Aeolotron test experiments with the small light source is shown in figure 5.6. Each image sequence consisting of 100 images taken in 1 second is summed up over the time coordinate. The

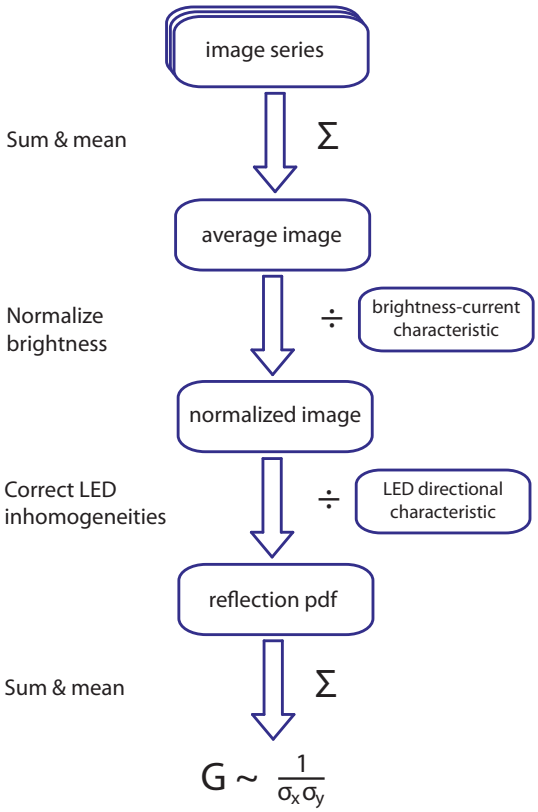

Figure 5.6: The process of slope reconstruction from reflection images.

brightness of the resulting average image needs to be normalized, since images are acquired with changing illumination brightness to ensure optimum saturation of the images at all wind speeds. The normalization factor for the brightness can be obtained from the brightness-current characteristic in 4.15. The image gray values are divided by the factor corresponding to the light source current used during image acquisition, and are thus normalized to a current of 0.1 A (which is the LED current rating for continuous use). Inhomogeneities in the directional characteristic can in theory be corrected by element-wise division of the normalized image with the correction image that was obtained from the calibration measurements described in section 4.3. Finally, the average of the corrected image gray values is determined. Only relative measurements are possible with this approach, a calibration is done by simultaneous measurement of the mean square slope with the CISG.

5.3 Wave Height Evaluation

5.3.1 Parallax Determination

To reconstruct the water height, the stereo parallax needs to be determined for each reflection. An elegant way to do this is offered by Fourier analysis.

Instead of describing an image by its gray values in *position* space, one can equivalently describe it in terms of wavenumbers in *frequency* space. The frequency space representation is obtained from the position space representation by applying the Fourier transform (FT)

$$\hat{g}(\mathbf{k}) = \iint_{-\infty}^{\infty} g(\mathbf{x}) \exp(-2\pi \mathbf{k} \cdot \mathbf{x}) d\mathbf{x} \tag{5.16}$$

The inverse Fourier transformation, which transforms an image from frequency space to an image in position space, is given by

$$g(\mathbf{x}) = \iint_{-\infty}^{\infty} \hat{g}(\mathbf{k}) \exp(2\pi \mathbf{k} \cdot \mathbf{x}) d\mathbf{x}. \tag{5.17}$$

Accounting for pixel discretization, the FT alters to

$$\hat{g}_{u,v} = \frac{1}{MN} \sum_{m=0}^{M-1} \sum_{n=0}^{N-1} g_{m,n} \exp\left(-\frac{2\pi m u}{M}\right) \exp\left(-\frac{2\pi n v}{N}\right), \tag{5.18}$$

and similarly for the inverse FT. For further information including some mathematical prerequisites, the reader is referred to Jähne (2005).

Consider the product of the Fourier transforms of two images[6], $g_1(\mathbf{x})$ and $g_2(\mathbf{x}')$

$$\hat{g}_1(\mathbf{k}) \hat{g}_2^*(\mathbf{k}) = \iint_{-\infty}^{\infty} g_1(\mathbf{x}) \exp(-2\pi \mathbf{k} \cdot \mathbf{x}) \mathrm{d}\mathbf{x} \iint_{-\infty}^{\infty} g_2(\mathbf{x}') \exp(-2\pi \mathbf{k} \cdot \mathbf{x}') \mathrm{d}\mathbf{x}'. \tag{5.19}$$

If the only difference in the two images is a global shift $\mathbf{\Delta x}$ (e.g. a stereo parallax), so that $g_2(\mathbf{x}') = g_2(\mathbf{x} + \Delta\mathbf{x}) = g_1(\mathbf{x})$, equation (5.19) can be rewritten

$$\begin{aligned}
\hat{g}_1(\mathbf{k}) \hat{g}_2^*(\mathbf{k}) &= \iint_{-\infty}^{\infty} g_1(\mathbf{x}) \exp(-2\pi \mathbf{k} \cdot \mathbf{x}) \mathrm{d}\mathbf{x} \iint_{-\infty}^{\infty} g_2(\mathbf{x} + \mathbf{\Delta x}) \exp(2\pi \mathbf{k} \cdot (\mathbf{x} + \mathbf{\Delta x})) d\mathbf{x} \\
&= \exp(-2\pi \mathbf{k} \cdot \mathbf{\Delta x}) \iint_{-\infty}^{\infty} g_1(\mathbf{x}) \exp(-2\pi \mathbf{k} \cdot \mathbf{x}) d\mathbf{x} \iint_{-\infty}^{\infty} g_1(\mathbf{x}) \exp(2\pi \mathbf{k} \cdot \mathbf{x}) d\mathbf{x} \\
&= \exp(-2\pi \mathbf{k} \cdot \mathbf{\Delta x})\ \hat{g}_1(\mathbf{k}) \hat{g}_1^*(\mathbf{k}) \\
&= \exp(-2\pi \mathbf{k} \cdot \mathbf{\Delta x})\ |\hat{g}_1(\mathbf{k})|^2 .
\end{aligned} \tag{5.20}$$

The global shift in gray values in image 2 with respect to image 1 translates into a global complex phase factor in Fourier space. Dividing (5.20) by $|\hat{g}_1(\mathbf{k})|^2$ and applying the inverse FT yields

$$\iint_{-\infty}^{\infty} \exp(-2\pi \mathbf{k} \cdot \mathbf{\Delta x}) \exp(2\pi \mathbf{k} \cdot \mathbf{x}) d\mathbf{k} = \iint_{-\infty}^{\infty} \exp(2\pi \mathbf{k} \cdot (\mathbf{x} - \mathbf{\Delta x})) d\mathbf{k} = \delta(\mathbf{x} - \mathbf{\Delta x}). \tag{5.21}$$

[6] To simplify the equations, the gray value distribution is treated as a continuous function of $\mathbf{x}$ here, quantization effects are discussed later.

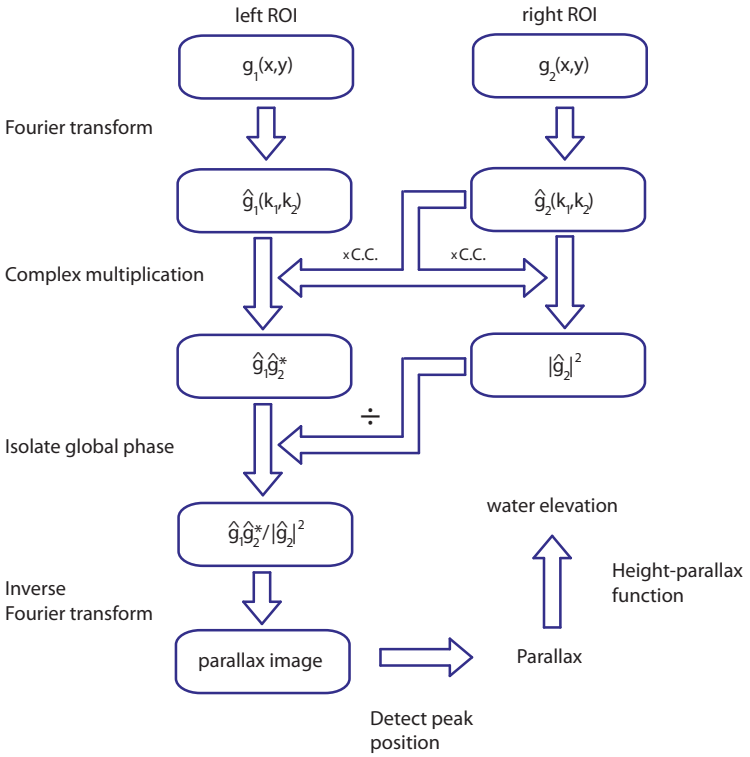

Figure 5.7: Flow chart of the height reconstruction algorithm.

The resulting image has a sharp peak at the coordinates of the shift between the images. Since images are noisy and quantized both in position and frequency space, and since the parallax is not an integer in general, the peak covers multiple pixels. The gray value distribution of the peak can be used for detecting the peak position with subpixel accuracy, e.g. by determining its "center of gravity". The same argumentation can be applied to regions of interest cut out of the images. This way, the parallax can be computed for each reflection.

5.3.2 Implementation of the Image Processing Algorithm

A schematic of the complete height reconstruction algorithm is given in figure 5.7. After the selection of a suitable region of interest (ROI) (i.e. an image segment that is containing a reflection) in the image, Fourier transformations are computed for both left and right image ROIs. The FT of the left image is multiplied with the complex conjugate (C.C.) of the FT of the right image to obtain (5.20), while the FT of the right image is multiplied with its own complex conjugate to obtain the square of the absolute value. Then, by dividing the left by the right the global phase factor is isolated. An inverse Fourier transformation is applied and the center of gravity of the resulting peak is computed. The peak position is identical to the parallax of the contents of the region of interest. With the height-parallax function from section 3.3 the corresponding water elevation can be determined. This algorithm was used to evaluate the stereo calibration measurements described in section 4.3.

6 Results

The RSSG was tested at the Aeolotron during a gas exchange measurement campaign in the spring of 2010. For the gas exchange experiments, it was necessary to continuously increase or decrease the wind speed according to figure 6.1. The RSSG was continuously acquiring data; the datasets were then classified by the wind speed during acquisition and grouped into wind speed bins with a width of 0.2 m/s.

6.1 Sample Images

Figure 6.2 shows 3 stereo images that were acquired at the Aeolotron. These are false color images, the left image gray values are shown in green, those of the right image in red. In the yellow areas, reflections in both images overlap. The footprint at the water surface is about 55 x 50 cm.

Different stages of the wave field development are readily observable: At low wind speeds (upper image, $U = 1.6\,\mathrm{m/s}$), the water surface is relatively smooth and a small number of reflections are visible. Most of the reflections are extended in the y-direction. Two effects contribute to this: Firstly, the waves are approximately plane waves, propagating in the x-direction, and secondly, the light source is extended in the y-direction. At medium wind speeds (middle image, $U = 2.9\,\mathrm{m/s}$), many "ripples" (capillary waves) appear on the water surface. The number of reflections increases, at the same time the single reflections become smaller. A structure with interchanging patches with many speckles and patches with almost no speckles evolves. At at wind speed of $U = 5.4\,\mathrm{m/s}$ (lower image), this structure is more pronounced. The darker patches belong to the windward side of short gravity waves (with a wavelength of 15-20 cm). The brighter patches correspond to the leeward side of the short gravity waves, where many reflections are visible, due to parasitic capillaries.

6.2 Mean Square Slope

Figure 6.3 shows the dependence of the mean square slope (mss) on wind speed, as measured with the color imaging slope gauge (Rocholz, 2010). The dependence of the mss on wind speed is linear, but with a change in the slope at 3.5 m/s, where the slope approximately doubles. This coincides with the onset of the breaking of short gravity waves.

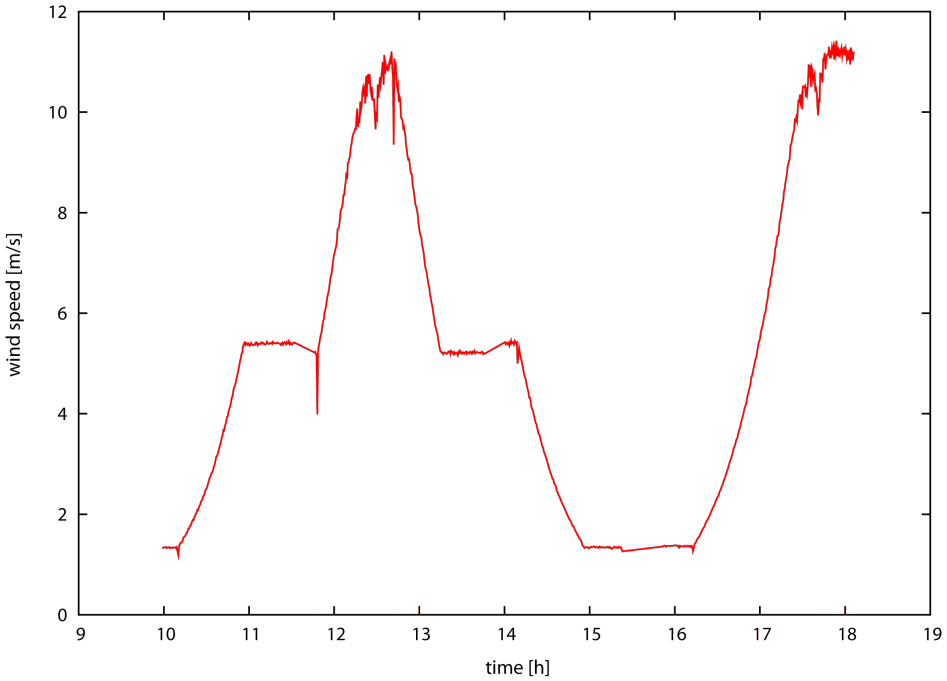

Figure 6.1: Time series of the reference wind speed U_{ref} during the Aeolotron test measurements, (May 4, 2010).

Figure 6.4 shows the evaluation of the RSSG data. The 'mean gray value' method, described in section 5.2, was used to obtain the factor[1] G that is proportional to $\frac{1}{\sigma^2}$. The wind dependence is similar to that obtained in the reference measurement with the ISG. The change in the slope of the linear fit occurs at the same wind speed, however, the slope triples at the transition, instead of doubling as it does in the CISG data. By scaling the slope of the linear fit for low wind speeds to that of the respective fit for the ISG data, the two data sets can be compared directly. In figure 6.5 the scaled RSSG data (blue) is plotted together with the CISG mss data (red). The two data sets coincide for wind speeds up to 3 m/s, at higher wind speeds, the RSSG overestimates the mean square slope.

The overestimation of the mss is caused by an underestimation of the mean gray value in the images. A possible cause for this underestimation is the segmentation in data preprocessing. The threshold was set to be three times the standard deviation of the background noise level. At high wind speeds, a significant number of reflections may have a brightness below this threshold, these speckles are "cut out" in the segmentation process.

6.3 The Effect of Surfactants

To study the effect of surface films on the wave field, a soluble surfactant (*Triton X-100*) was added to the water. All other environmental conditions were held constant, and the wind was varied according to the same scheme (see figure 6.1). Data from the measurements with clean

[1] G is the mean gray value of the image (after preprocessing).

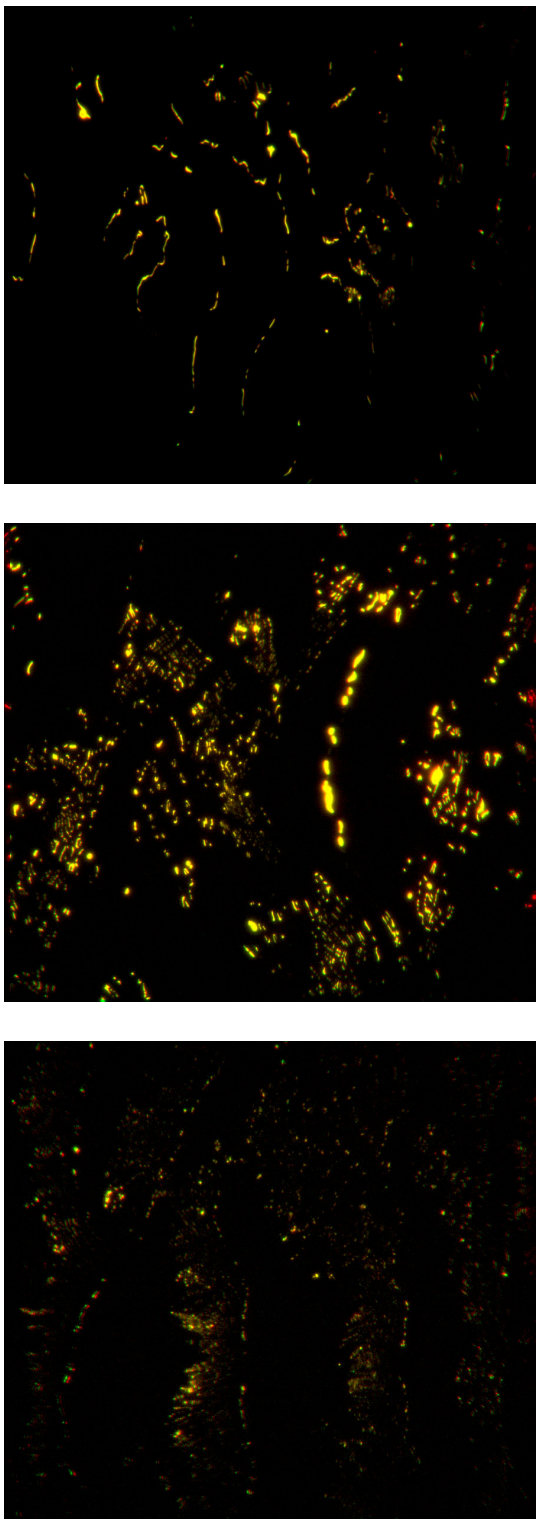

Figure 6.2: False color sample stereo images from the Aeolotron measurements. The wind is blowing from right to left at wind speeds (from top to bottom) 1.6 m/s, 2.9 m/s, and 5.4 m/s. The left camera is shown in green, the right camera in red. In the yellow areas, the two camera images overlap. The footprint at the water surface is 50 x 45 cm.

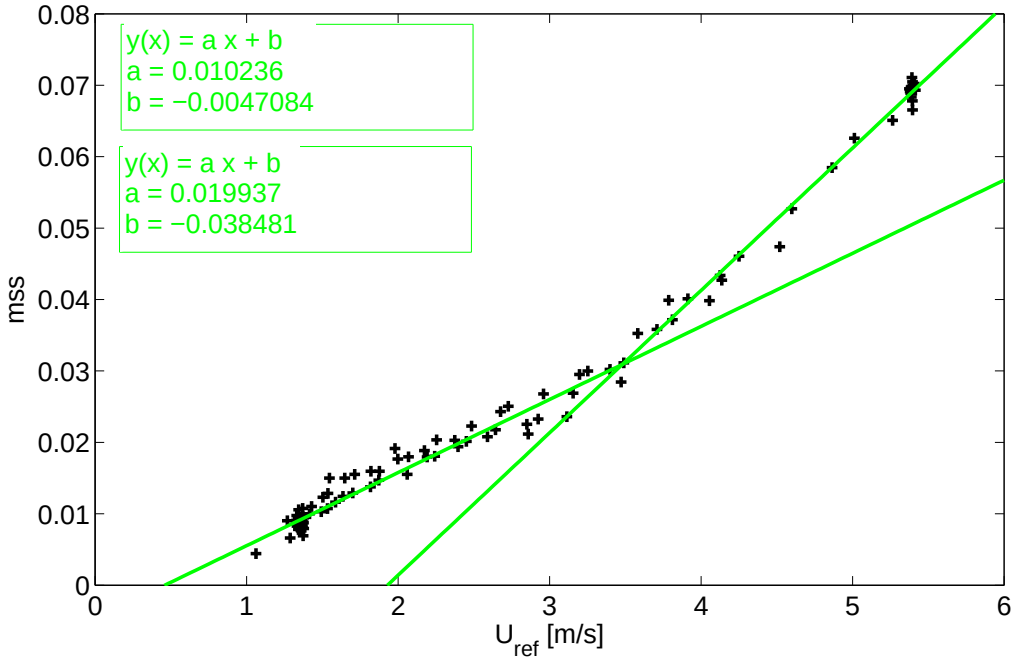

Figure 6.3: The dependence of the mean square slope on wind speed, measured at the Aeolotron with the CISG.

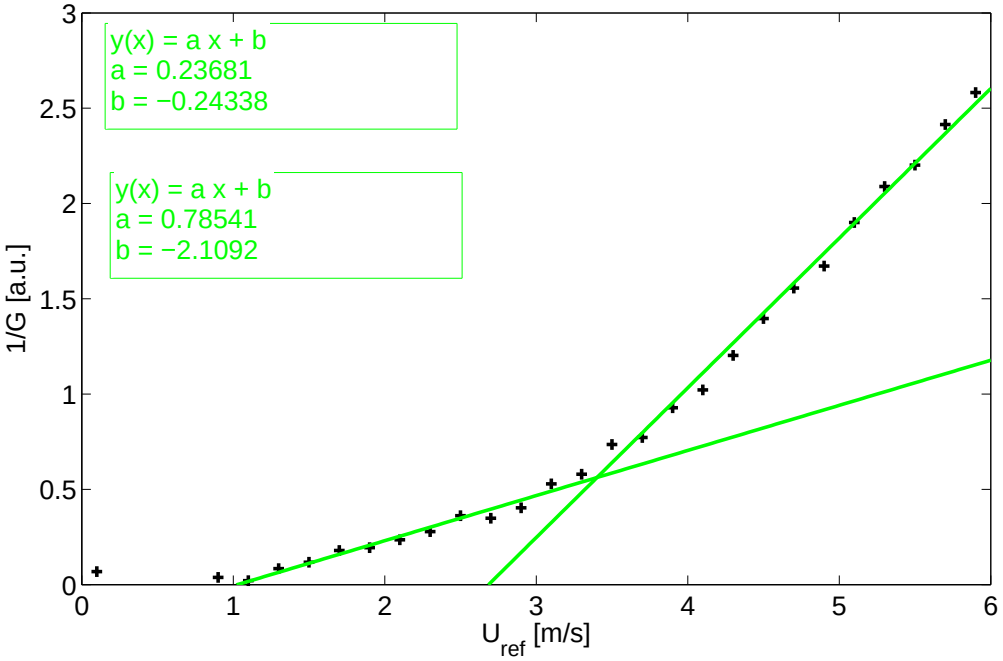

Figure 6.4: The dependence of the factor $1/G$, determined from RSSG data, on wind speed. The factor is proportional to the mean square slope, according to equation (5.14).

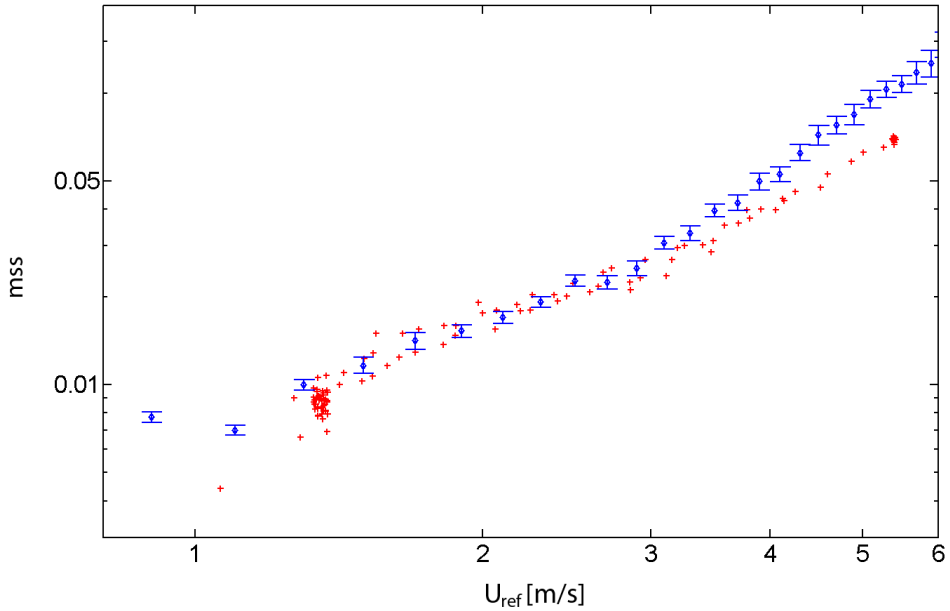

Figure 6.5: Comparison of the mss data sets obtained by the CISG (red) and the RSSG (blue). For low wind speeds the RSSG data coincides with the reference data from the CISG, at higher wind speeds the RSSG overestimates the mss.

water and with the surfactant are shown in figure 6.6. The $1/G$ factor that is proportional to the mean square slope, according to section 5.2.3, is shown for both clean water (black) and the water with added surfactant (red). The development of the wave field is clearly suppressed by the surfactant below a wind speed of 6 m/s. At higher wind speeds, the surface film breaks up, and the wave field begins to evolve. At wind speeds around 10 m/s the surfactant has no significant effect on the mean square slope.

6.4 Slope Probability Density Function

The CISG can determine the slope PDF in a range of $s_{x/y} = \pm 1.0$. Figure 6.7 shows the slope PDF in this range at three different wind speeds. With increasing wind speed, higher slopes are more probable and the distribution is widened. The distributions qualitatively agree with those given by Balschbach (2000).

The RSSG can only determine the slope distribution for very small slopes in the range $s_{x/y} = \pm 0.05$. The comparison of the measured slope PDFs is thus limited to this range. In figure 6.8, the 2D slope distributions measured by the RSSG and CISG are compared at low wind speeds. Although they exhibit a similar overall trend, significant differences are visible. The RSSG PDF is decreasing much faster towards the boundary of the measurable slope range. This is most likely due to inhomogeneous illumination. The illumination intensity is known to decrease towards the borders of the field of view of the camera because of the narrow radiation

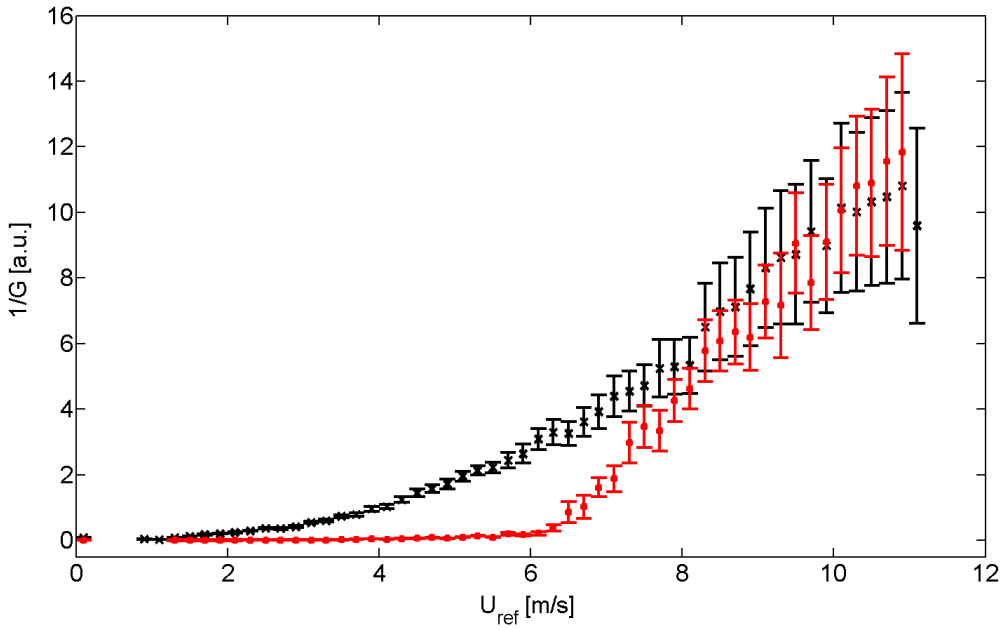

Figure 6.6: The development of the wave field is effectively suppressed by the presence of a surface film (Triton X-100) on the water surface (red data points). The reference data for the clean water surface (black) are from the same series as in 6.5.

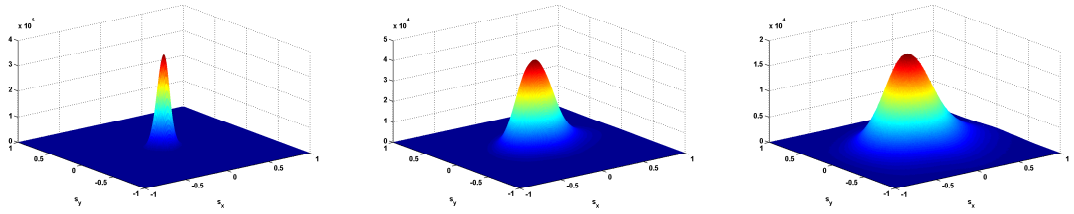

Figure 6.7: The 2D slope PDF measured with the CISG at (from left to right) 1.2 m/s, 5.2 m/s, and 10.2 m/s wind speed. z-axis: arbitrary scaling of the slope probability.

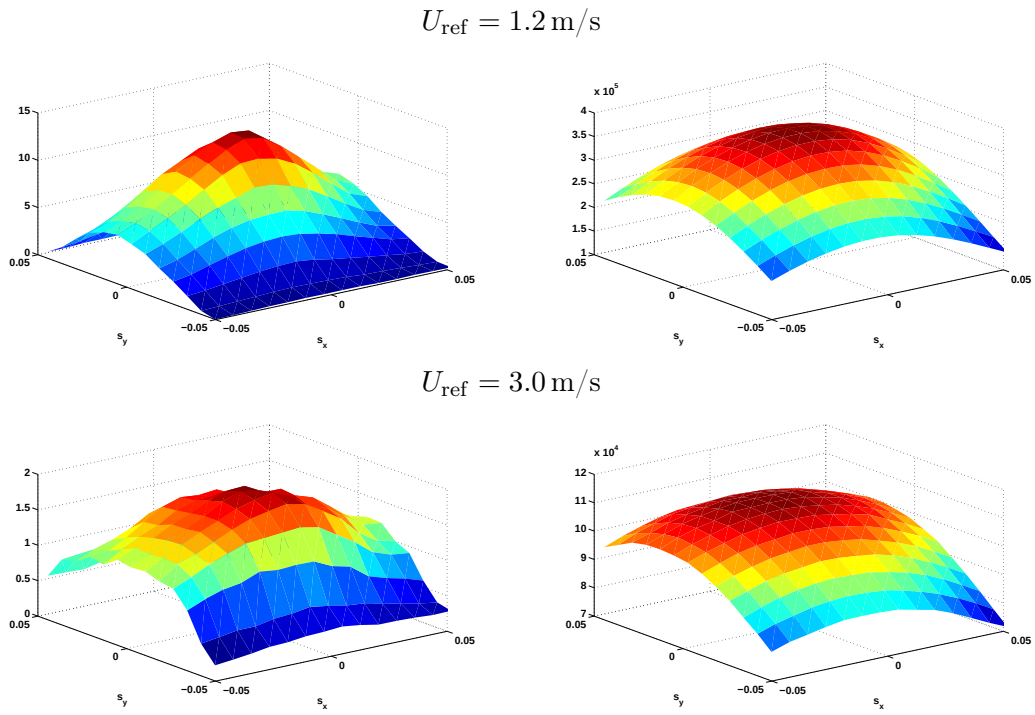

Figure 6.8: Comparison of the slope PDF measured with the RSSG (left) and CISG (right) at low wind speeds. z-axis: arbitrary scaling of the slope probability.

angle (see section 4.3.1). The intensity correction matrix described in section 4.3.1 was found to be insufficient and not used in the data evaluation.

At higher wind speeds (figure 6.9), the differences between the CISG and RSSG distributions are more pronounced. In the CISG distributions (right side), a shift of the maximum in the crosswind direction (y-direction) is visible. At high wind speeds (7.4 m/s, 10.2 m/s), the maximum of the distribution is shifted out of the measurement range of the RSSG. This cannot be explained with the expected distribution asymmetry (see 2.3) alone, since not only the maximum but also the mean of the distribution is shifted. In ocean measurements, the mean of the surface slope is zero for sufficiently long integration times. In the circular Aeolotron, however, the centrifugal force increases the mean water height at the outer wall and decreases it at the inner wall of the channel, leading to a mean slope other than zero. This shift of the distribution maximum is mostly concealed by the illumination inhomogeneities in the RSSG PDFs.

Another effect contributes to differences in the CISG and RSSG distributions: the footprint of the CISG is an area of 19.4 cm × 14.5 cm in the center of the water channel, while the RSSG footprint is extended almost over the full width of the channel (61 cm). Effects of the finite size of the water channel may thus be more pronounced in the RSSG data.

A general difference in the measurement principles of the RSSG and CISG is responsible for the different sensitivities to wave field inhomogeneities. The RSSG is measuring a single slope at each pixel of its footprint, the slope distribution is obtained by combination of all this information. A distinct slope distribution in a part of the footprint will thus affects a part

$U_{\text{ref}} = 4.2\,\text{m/s}$

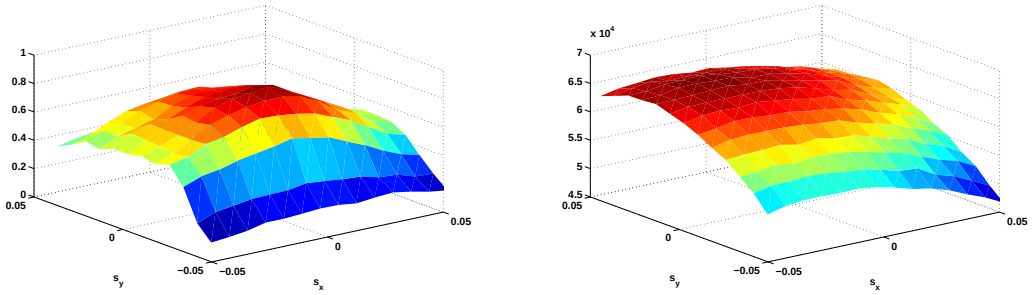

$U_{\text{ref}} = 5.2\,\text{m/s}$

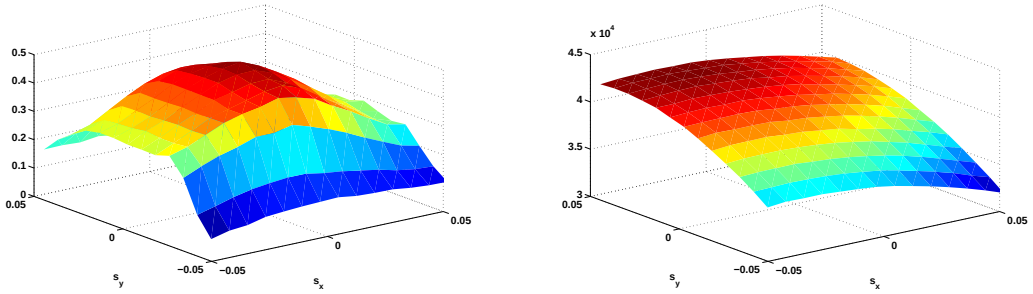

$U_{\text{ref}} = 7.4\,\text{m/s}$

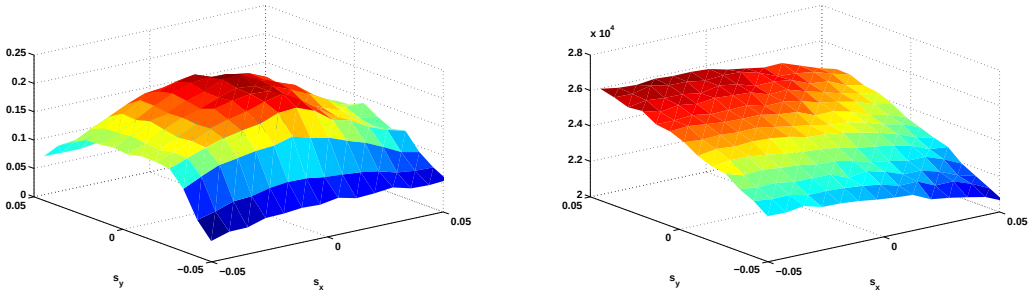

$U_{\text{ref}} = 10.2\,\text{m/s}$

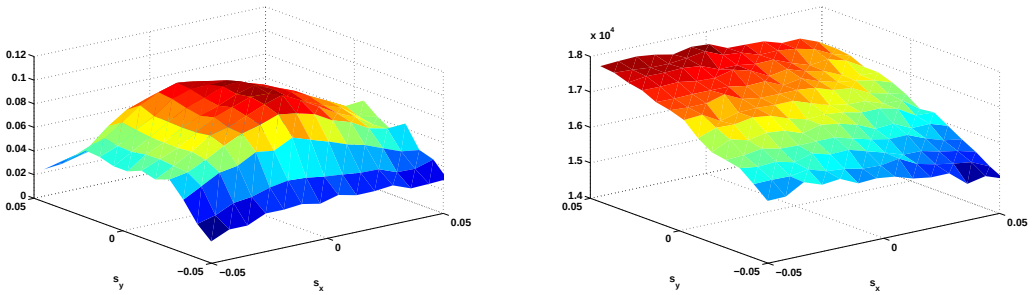

Figure 6.9: Comparison of the slope PDF measured with the RSSG (left) and CISG (right) at higher wind speeds. z-axis: arbitrary scaling of the slope probability.

of the slope distribution only. This means, that inhomogeneities lead to distortions of the measured slope PDF. The CISG on the other hand measures the whole slope distribution for each pixel of its images. The global slope distribution is then obtained by averaging all these distributions. Inhomogeneities in an area of the footprint will thus affect the global slope distribution as a whole in the averaging process.

6.5 Discussion

The RSSG has been tested in a wide range of wind speeds under clean water and slick conditions at the Aeolotron. Simultaneous reference slope PDF measurements were performed with an CISG (Rocholz, 2010).

Mean square slope values determined by the RSSG can be calibrated with the values determined by the CISG in the range of 0 to 3 m/s (see section 6.2). At higher wind speeds, the RSSG significantly overestimates the mean square slope. This can be attributed to insufficient illumination brightness and the segmentation during preprocessing. The problem is strongly correlated to the high dynamic range in speckle brightness that was simulated in section 4.2. The high curvature of small structures like capillary waves reduces the reflection brightness by multiple orders of magnitude, compared to a flat water surface. With the small light sources that were used in the test experiments, the intensities of reflections coming from high curvature areas were of the same order of magnitude as background noise. Thus it was inevitable that some reflections were cut out of the images in the segmentation process. The size of the new larger light sources for the field measurements is almost four times the size of the small laboratory test light sources. Since the mean gray value in the image is linearly dependent on the light source dimensions (see section 5.2.3), speckle size and brightness can be increased to facilitate the separation of speckles from background also at high wind speeds. For the available laboratory data, the extraction of the mean square slope by fitting the speckle brightness distribution with a model PDF (see section 5.2.3) was unsuccessful due to the deviations in the brightness distribution (see 6.4).

The big influence of surfactants on the measured mean square slope values (see section 6.3) can directly be seen from figure 6.6. The damping of capillary waves reduces surface curvature, the intensity of the speckles is strongly increased. Due to the large effect of surfactants on the mean gray value of the speckle images, surface slicks can be detected reliably by the RSSG. In field experiments, this is valuable information for gas and heat exchange experiments. With the RSSG mean square slope measurements, slick conditions can be distinguished from no-slick conditions. This allows conditional sampling of the exchange rates.

The partial slope probability distributions measured with the RSSG are compared to those measured with the CISG in section 6.4. Despite the similar trends that are observable, significant deviations occur. The probability for slopes near the maximum of the measurement range of the RSSG is underestimated and the shift of the distribution maximum due to the

centrifugal force (see section 6.4) that is visible in the CISG distributions is not measured by the RSSG. The slope measurement principle of the RSSG is based on the assumption of a homogeneous wave field in the footprint on the water surface is made. Information from the whole image has to be combined to yield a single PDF (see 3.2). However, the finite dimensions of the circular Aeolotron wind-wave facility lead to inhomogeneous conditions, varying over the RSSG footprint and distortions of the PDF are inevitable. The CISG is measuring the slope PDF in the center of the facility only, its footprint is much smaller. Inhomogeneities do not affect the CISG PDFs because the CISG can determine slope PDFs for single pixels which then are averaged to yield the global PDF. Inhomogeneities thus are reflected equally in the PDF as a whole, not only in certain areas.
Another factor contributing to the deviations of the RSSG slope PDFs is the directional characteristic of the LEDs. The LEDs are known to have inhomogeneities (see section 4.3) and the intensity of emitted radiation is lower in the direction of the image borders, where the higher slopes are measured. This leads to an additional underestimation of the higher slope values. The correction matrix determined in the calibration could not be used on the preprocessed experimental data. The image processing algorithm will be adapted for future measurements, the directional characteristic correction will be performed *before* the segmentation step in the preprocessing routine. Furthermore, the diffusors that are added to the new LED arrays will reduce the effects of directional inhomogeneities.

The stereo evaluation algorithm is currently under development. In section 4.3.3 the height reconstruction principle was shown to generally work in calibration measurements. The resolution of the images of the new RSSG is significantly improved over the earlier work of Waas (1992) and Dieter (1998). This allows higher precision in the determination of the parallax and thus better height resolution. The height resolution will depend on the size of the speckles, from the calibration measurements that were performed with a flat water surface it is estimated to be $\pm 2\,\mathrm{mm}$.

Implications for Field Measurements

Some difficulties that were observed in the laboratory test experiments could be accounted for in the development of the instrument for field measurements (see figure 4.2). The larger light sources provide sufficient illumination brightness for higher wind speeds. In addition, the holographic diffusors reduce directional inhomogeneities. The above mentioned difficulties with inhomogeneities of the wave field are not expected to occur in the ocean, the wave field in the ocean is in general homogeneous over the area of the RSSG footprint (except for the case of partial surface slick coverage, which can readily be detected), the problems with the finite size of the laboratory facility do not occur.

Pitch and roll of the ship will increase the slope range that is visible to the RSSG, the slope PDF can be measured for a larger range and the mean square slope components can be extracted by fitting the model PDF to the data. Data from the inclination sensor can be

included at the beginning of the slope evaluation process. In field measurements, it is also necessary to account for the change of the distance Z to the water surface due to pitch and roll or larger waves. For the calibration of the slope measurements (see 3.2.4, it should be sufficient to use the mean water height, determined globally for each stereo image pair. This eliminates the need for a sophisticated stereo height reconstruction algorithm for slope measurements. The algorithm presented in section 5.3 is capable of providing this information and ready to use.

7 Conclusion and Outlook

7.1 Conclusion

An improved optical instrument for the measurement of surface ocean wave statistics has been presented in this thesis. This reflective stereo slope gauge (RSSG) is capable of simultaneous measurements of height and slope statistics of the water surface in the field.

Using a stereo camera setup and two artificial light sources, the correspondence problem at the specular reflecting water surface can be solved (see section 3.3). Cameras and light sources are triggered to ensure that each camera can only see reflections coming from the corresponding light source (see section 4.1). The distance of the instrument to the reflections on the water surface can be reconstructed from the parallax of the reflections in stereo images (see section 5.3). From this information, wave height statistics can be inferred. The water height could be reconstructed from stereo parallax in calibration measurements (see section 4.3.3) with an accuracy of ± 2 mm at a working distance of 4.8 m (see section 6.5).

The light sources are built from infrared LEDs. Their emission peak wavelength (940 nm) is matched to a water absorption peak. Since the penetration depth is only 3.4 cm, upwelling light can be effectively suppressed (see section 2.4.3).

The probability distribution of surface slope is related to the probability distribution of the occurrence of reflections at different image positions (see section 3.2). Slope statistics are derived from the spatial brightness distribution in the images (see section 5.2).

A laboratory version of the instrument has been set up and characterized at the Aeolotron wind wave facility (see section 4.1). It is shown that the RSSG can be used to acquire the two-dimensional slope probability distribution for a slope range of ± 0.05 (see section 6.4). However, significant deviations to reference measurements occurred. Inhomogeneities in the illumination brightness due to the directional characteristics of the light source were identified to be a major source of error.

The directional radiation characteristic of the LED emission was measured and a correction matrix was obtained (see section 4.3.1). The evaluation of the test experiment data demonstrated the need for an on-line correction, that is performed prior to further image preprocessing (see section 6.5). Another measure to homogenize the light sources is the use of holographic diffusors (see section 4.3.1). This is already incorporated in the design of the instrument for the field measurements.

From the slope probability distributions, the mean square slope was extracted (see section 6.2). The comparison with reference measurements shows good agreement at low wind speeds. At higher wind speeds, the RSSG systematically overestimates the mean square slope. This can be attributed to insufficient illumination brightness. Surface curvature leads to a high dynamic range in speckle reflection brightness (see section 4.2). At higher wind speeds, mean speckle brightness decreases to the level of background noise and reflections are missed by the image processing algorithms (see section 5.1), which leads to the observed overestimation of mean square slope (see section 5.2). To approach this problem, the size of the light sources for the ocean instrument has been increased by a factor of 4, compared to the laboratory setup (see section 4.1).

The laboratory experiments have confirmed the ability of the RSSG to detect surface slicks (see section 6.3). This feature will aid the data evaluation of heat exchange experiments (see section 6.5).

7.2 Outlook

The ocean instrument is scheduled to be deployed to the Baltic Sea in June 2010. It will accompany heat exchange measurements from aboard a research vessel.

The effect of the holographic diffusors on the directional characteristic of the light sources has to be studied. If necessary, a correction matrix has to be obtained from further calibration measurements.

A stereo evaluation algorithm capable of reconstructing the envelope of the wave field is currently under development. Comparative field measurements with a polarimetric camera are aspired to assess the accuracy of the wave field height reconstruction and slope statistics.

Bibliography

G. B. Airy. On tides and waves. In *Encyclopaedia Metropolitana*, pages 241–396. B. Fellowes, London, 1845.

G. Balschbach. *Untersuchungen statistischer und geometrischer Eigenschaften von Windwellen und ihrer Wechselwirkung mit der wasserseitigen Grenzschicht*. Dissertation, Institut für Umweltphysik, Fakultät für Physik und Astronomie, Univ. Heidelberg, 2000. URL `http://www.ub.uni-heidelberg.de/archiv/2473/`.

M. L. Banner and O. M. Phillips. On the incipient breaking of small-scale waves. *Journal of Fluid Mechanics*, 65:647–656, 1974.

M. L. Banner, I. S. F. Jones, and J. C. Trinder. Wavenumber spectra of short gravity waves. *Journal of Fluid Mechanics*, 198:321–344, 1989.

N. F. Barber. A diffraction analysis of a photograph of the sea. *Nature*, 164:485–485, 1949.

E. J. Bock and T. Hara. Optical measurements of ripples using a scanning laser slope gauge. In *Optics of the Air-Sea Interface*, volume 1749, page 272ff, 1992. Part II: Data analysis and interpretation from a laboratory.

J. Boussinesq. Théorie des ondes et des remous qui se propagent le long d'un canal rectangulaire horizontal, en communiquant au liquide contenu dans ce canal des vitesses sensiblement pareilles de la surface au fond. *J. Math. Pures Appl.*, 17 (2):55–108, 1872.

F. M. Bréon and N. Henriot. Spaceborne observations of ocean glint reflectance and modeling of wave slope distributions. *Journal of Geophysical Research (Oceans)*, 111:6005–+, June 2006. doi: 10.1029/2005JC003343.

B. Chapron, V. Kerbaol, D. Vandemark, and T. Elfouhaily. Importance of peakedness in sea surface slope measurements and applications. *Journal of Geophysical Research Oceans*, 105 (C7):17195–202, 2000.

L.J. Cote, J.O. Davis, W. Marks, R.J. McGough, E. Mehr, W.J. Jr. Pierson, J.F. Ropek, G. Stephenson, and R.C. Vetter. The directional spectrum of a wind generated sea as determined from data obtained by the stereo wave observation project. *Meteorological Papers*, 2 (6):1–88, 1960.

C. Cox and W. Munk. Statistics of the sea surface derived from sun glitter. *Journal of Marine Research*, 13(2):198–227, 1954a.

C. Cox and W. Munk. Slopes of the sea surface deduced from photographs of sun glitter. Technical report, University of California, 1956.

C. S. Cox. Measurement of slopes of high-frequency wind waves. *J. Marine Res.*, 16(3): 199–225, 1958.

Charles Cox and Walter Munk. Measurements of the roughness of the sea surface from photographs of the sun's glitter. *Journal of the Optical Society of America*, 44(11):838–850, 1954b.

J. Dieter. *Analysis of Small-Scale Ocean Wind Waves by Image Sequence Analysis of Specular Reflections.* Dissertation, IWR, Fakultät für Physik und Astronomie, Univ. Heidelberg, 1998. URL `http://d-nb.info/955455804`.

E. B. Dobson. Measurements of the fine-scale structure of the sea. *J.Geophys.Res.*, 75:2853–2856, 1970.

M. A. Donelan and R. Wanninkhof. Gas transfer at water surfaces - conepts and issues. In M. A. Donelan, W. M. Drennan, E. S. Saltzman, and R. Wanninkhof, editors, *Gas Transfer at Water Surfaces.* American Geophysical Union, 2002.

M. A. Donelan, J. Hamilton, and W. H. Hui. Directional spectra of wind-generated waves. *Royal Society of London Philosophical Transactions Series A*, 315:509–562, September 1985.

F.Y. Edgeworth. The generalised law of error, or law of great numbers. *Journal of the Royal Statistical Society*, 69:497–530, 1906.

C. B. Field and M. R. Raupach. *The Global Carbon Cycle : Integrating Humans, Climate, and the Natural World.* Island Press, Washington D.C., 2004.

D. Fuß. *Kombinierte Höhen- und Neigungsmessung von winderzeugten Wasserwellen am Heidelberger Aeolotron.* Dissertation, Institut für Umweltphysik, Fakultät für Physik und Astronomie, Univ. Heidelberg, Heidelberg, Germany, 2004. URL `http://www.ub.uni-heidelberg.de/archiv/4820`.

E. Hecht. *Optics.* Addison Wesley, 4th edition, 2001.

H. Hühnerfuss, W. Walter, P. Lange, and W. Alpers. Attenuation of wind waves by monomolecular sea slicks and the Marangoni effect. *Journal of Geophysical Research*, 92: 3961–3963, 1987.

L. H. Holthuijsen. Observations of the directional distribution of ocean-wave energy in fetch-limited conditions. *J.Phys.Oceanogr.*, 13:191–207, 1983a.

L. H. Holthuijsen. Stereophotography of ocean waves. *Applied Ocean Research*, 5:204–209, 1983b.

B. A. Hughes, R. W. Grant, and R. W. Chappell. A fast response surface-wave slope meter and measured wind-wave moments. *Deep-Sea Res.*, 24:1211–1223, 1977.

J. D. Jackson. *Classical Electrodynamics*. Wiley, 3rd edition, 1998.

B. Jähne. *Zur Parametrisierung des Gasaustauschs mit Hilfe von Laborexperimenten*. Dissertation, Institut für Umweltphysik, Fakultät für Physik und Astronomie, Univ. Heidelberg, 1980. URL `http://d-nb.info/810123614`. IUP D-145.

B. Jähne. *On the transfer processes at a free air-water interface*. Habilitation thesis, Institut für Umweltphysik, Fakultät für Physik und Astronomie, Univ. Heidelberg, 1985. IUP D-200.

B. Jähne. *Digitale Bildverarbeitung*. Springer, Berlin, 6 edition, 2005. doi: 10.1007/b138991.

B. Jähne. Investigating the mechanisms of air-water gas transfer by quantitative imaging techniques: history, current progress and remaining challenges. In *6th Int. Symp. Gas Transfer at Water Surfaces, Kyoto, May 17–21, 2010*, 2010. keynote talk.

B. Jähne and K. Riemer. Two-dimensional wave number spectra of small-scale water surface waves. *J. Geophys. Res.*, 95(C7):11531–11646, 1990. doi: 10.1029/JC095iC07p11531.

B. Jähne, K. O. Münnich, and U. Siegenthaler. Measurements of gas exchange and momentum transfer in a circular wind-water tunnel. *Tellus*, 31:321–329, 1979.

B. Jähne, K. O. Münnich, R. Bösinger, A. Dutzi, W. Huber, and P. Libner. On the parameters influencing air-water gas exchange. *Journal of Geophysical Research*, 92:1937–1950, February 1987. doi: 10.1029/JC092iC02p01937.

B. Jähne, J. Klinke, and S. Waas. Imaging of short ocean wind waves: a critical theoretical review. *J.Opt.Soc.Am.*, 11:2197–2209, 1994. doi: 10.1364/JOSAA.11.002197.

B. Jähne, M. Schmidt, and R. Rocholz. Combined optical slope/height measurements of short wind waves: principles and calibration. *Measurement Science & Technology*, 16(10): 1937–1944, 2005. ISSN 0957-0233. doi: 10.1088/0957-0233/16/10/008.

M. G. Kendall and A. Stuart. *The advanced theory of statistics, Vol. 1: Distribution theory*. Griffin, London, 1977.

B. Kinsman. *Wind Waves: Their Generation and Propagation on the Ocean Surface*. Prentice-Hall, Englewood Cliffs, 1965.

J. Klinke and B. Jähne. Measurements of short ocean waves during the mbl ari west coast experiment. In B. Jähne and E. C. Monahan, editors, *Air-water Gas Transfer, Selected Papers from the Third International Symposium on Air–Water Gas Transfer*, pages 165–173, Hanau, 1995. Aeon.

E. Kohlschütter. Die Forschungsreise S.M.S. Planet II. Stereophotogrammetrische Aufnahmen. *Annalen der Hydrographie und Maritimen Meterologie*, 34:220–227, 1906.

L. Kou, D. Labrie, and P. Chylek. Refractive indices of water and ice in the 0.65–2.5 μm spectral range. *Appl. Opt.*, 32:3531–3540, 1993.

P. K. Kundu. *Fluid Mechanics*. Academic Press, San Diego, CA, 4th edition, 2007.

W. Laas. Photographische Messung der Meereswellen. *Zeitschr. d. Vereins Dtsch. Ingenieure*, 49:S.1889 ff. S.1937 ff. und S.1976 ff., 1905.

W. Laas. Messung der Meereswellen und ihre Bedeutung für den Schiffsbau. *Jahrbuch der Schiffsbautechn. Gesellschaft*, 7:S.391 ff., 1906.

W. Laas. Die photographische Messung der Meereswellen. *Veröff. Inst. f. Meereskunde N. F. Reihe A*, Heft 7, 1921.

A. K. Liu, S. Martin, and R. Kwok. Tracking of ice edges and ice floes by wavelet analysis of SAR images. *Journal of Atmospheric and Oceanic Technology*, 14:1187–1198, 1997a.

Y. Liu, X.-H. Yan, W. T. Liu, and P. A. Hwang. The probability density function of ocean surface slopes and its effects on radar backscatter. *Journal of Physical Oceanography*, 27: 782–797, May 1997b. doi: 10.1175/1520-0485(1997)027.

M. S. Longuet-Higgins. The effect of non-linearities on statistical distributions in the theory of sea waves. *Journal of Fluid Mechanics*, 17:459–480, 1963.

M. S. Longuet-Higgins. On the skewness of sea-surface slopes. *Journal of Physical Oceanography*, 12:1283–1291, November 1982.

M.S. Longuet-Higgins. On the joint distribution of the periods and amplitudes of sea waves. *Journal of Geophysical Research Oceans*, 80:2688–2694, 1975. URL `http://europa.agu.org/?uri=/journals/jc/JC080i018p02688.xmlview=article`.

J. Larry Pezzaniti, David Chenault, Mike Roche, John Reinhardt, and Howard Schultz. Wave slope measurement using imaging polarimetry. In *Ocean Sensing and Monitoring*, 2009. doi: 10.1117/12.819031.

O. M. Phillips. *The dynamics of the upper ocean*. Cambridge University Press, second edition edition, 1977.

W. J. Plant. A new interpretation of sea-surface slope probability density functions. *Journal of Geophysical Research (Oceans)*, 108:3295–11, 2003a. doi: 10.1029/2003JC001870.

W. J. Plant. Bound waves and sea-surface slopes. In *OCEANS 2003. Proceedings*, volume 4, pages 1825–1828, 2003b.

R. M. Pope and E. S. Fry. Absorption spectrum (380 -700 nm) of pure water. II. Integrating cavity measurements. *Appl Opt*, 36:8710–8723, November 1997.

K. Richter. Technische Daten des Aeolotron nach dem Umbau 2007/2008. Technical report, Institute of Environmental Physics, University of Heidelberg, 2009.

R. Rocholz. Bildgebendes System zur simultanen Neigungs- und Höhenmessung an kleinskaligen Wind-Wasserwellen. Diplomarbeit, University of Heidelberg, 2005.

R. Rocholz. *Spatiotemporal Measurement of Short Wind-Driven Water Waves*. Dissertation, Institut für Umweltphysik, Fakultät für Physik und Astronomie, Univ. Heidelberg, 2008. URL `http://www.ub.uni-heidelberg.de/archiv/8897`.

R. Rocholz. Calibration of the 2010-CISG Setup at the Aeolotron. Technical report, Institute of Environmental Physics, University of Heidelberg, 2010.

C. L. Sabine, R. A. Feely, N. Gruber, R. M. Key, K. Lee, J. L. Bullister, R. Wanninkhof, C. S. Wong, D. W. R. Wallace, B. Tilbrook, F. J. Millero, T.-H. Peng, A. Kozyr, T. Ono, and A. F. Rios. The ocean sink for anthropogenic CO_2. *Science*, 305:367–372, 2004.

A. H. Schooley. A simple optical method of measuring the statistical distribution of water surface slopes. *Journal of the Optical Society of America*, 44(37), 1954.

A. Schumacher. Stereophotogrammetrische Wellenaufnahmen. *Wissenschaftliche Ergebnisse der Deutschen Atlantischen Expedition auf dem Forschungs- und Vermessungsschiff Meteor*, 1925 - 1927, 1939.

A. Schumacher. Stereophotogrammetrische wellenaufnahmen mit schneller bildfolge. *Deutsche Hydrographische Zeitschrift*, 3(1-2):78–82, 1950.

A. Schumacher. Results of exact wave measurements (by stereophotogrammetry) with special reference to more recent theoretical investigations. In *Proceedings of the NBS Semicentennial Symposium on Gravity Waves held at the NBS on June 18-20, 1951*, pages 69–78, November 1952.

J. C. Scott. An optical probe for measuring water wave slopes. *Journal of Physics E Scientific Instruments*, 7:747–749, September 1974. doi: 10.1088/0022-3735/7/9/021.

O. H. Shemdin, H. M. Tran, and S. C. Wu. Directional measurements of short ocean waves with stereophotography. *J.Geophys.Res.*, 93:13891–13901, 1988.

D. Jr Stilwell. Directional energy spectra of the sea from photographs. *J.Geophys.Res.*, 74: 1974–1986, 1969.

G. G. Stokes. On the theory of oscillatory waves. *Trans. Camb. Philos. Soc.*, 8:441, 1849.

G. V. Sturm and F. Y. Sorrell. Optical wave measurement technique and experimental comparison with conventional wave height probes. *Appl.Opt.*, 12:1928–1934, 1973.

T. Takahashi, S.C. Sutherland, R. Wanninkhof, C. Sweeney, R.A. Feely, D.W. Chipman, B. Hales, G. Friederich, F. Chavez, C. Sabine, et al. Climatological mean and

decadal change in surface ocean pco2, and net sea-air co2 flux over the global oceans. *Deep Sea Research Part II: Topical Studies in Oceanography*, 56:554–577, 2009. doi: doi:10.1016/j.dsr2.2008.12.009.

V. I. Tatarskii. Multi-gaussian representation of the cox?munk distribution for slopes of wind-driven waves. *Journal of Atmospheric and Oceanic Technology*, 20(11):1697?1705, November 2003.

R. Tober, R.C. Anderson, and O. Shemdin. Laser instrument for detecting water ripple slopes. *Appl. Opt.*, 12:788–794, 1973.

G. R. Valenzuela. Theories for the interaction of electromagnetic and ocean waves - a review. *Boundary-Layer Meteorology*, 13:61–85, 1978.

S. Waas. Entwicklung eines verfahrens zur messung kombinierter höhen- und neigungsverteilungen von wasseroberflächenwellen mit stereoaufnahmen. Diplomarbeit, Institut für Umweltphysik, Fakultät für Physik und Astronomie, Univ. Heidelberg, 1988. IUP D-248.

S. Waas. *Entwicklung eines feldgängigen optischen Meßsystems zur stereoskopischen Messung von Wasseroberflächenwellen.* Dissertation, Institut für Umweltphysik, Fakultät für Physik und Astronomie, Univ. Heidelberg, 1992. URL `http://d-nb.info/930235711`.

S. Waas and B. Jähne. Combined slope-height measurements of short wind waves: first results from field and laboratory measurements. In L. Estep, editor, *Optics of the Air-Sea Interface: Theory and Measurements*, volume 1749 of *SPIE Proc.*, pages 295–306, 1992.

R. Wanninkhof, W. E. Asher, D. T. Ho, C. Sweeney, and W. R. McGillis. Advances in quantifying air-sea gas exchange and environmental forcing. *Annual Rev. Marine Sci.*, 1: 213–244, 2009. doi: 10.1146/annurev.marine.010908.163742.

F. J. Wentz. Cox and Munk's sea surface slope variance. *Journal of Geophysical Research*, 81:1607–1608, 1976. doi: 10.1029/JC081i009p01607.

J. Wu. Slope and curvature distribution of wind-disturbed water surface. *Journal of the Optical Society of America*, 61:852–858, July 1971.

C. Zappa, M. Banner, H. Schultz, A. Corrada-Emmanuel, L. Wolff, and J. Yalcin. Retrieval of short ocean wave slope using polarimetric imaging. *Meas. Sci. Technol.*, 19:055503 (13pp), 2008.

C. J. Zappa, W. E. Asher, and A. T. Jessup. Microscale wave breaking and air-water gas transfer. *Journal of Geophysical Research-Oceans*, 106(C5):9385–9391, 2001.

X. Zhang and C. S. Cox. Measuring the two-dimensional structure of a wavy water surface optically: A surface gradient detector. *Experiments in Fluids*, 17:225–237, August 1994. doi: 10.1007/BF00203041.

Danksagung: Ich bedanke mich herzlich bei Prof. Dr. Bernd Jähne, der diese Arbeit betreut und überhaupt erst ermöglicht hat. Ganz besonders möchte ich ihm dafür danken, dass ich im September 2009 an der SOLAS Open Science Conference in Barcelona teilnehmen durfte. Ein großer Dank geht auch an Prof. Dr. Ulrich Platt für die Übernahme der Zweitkorrektur.

Des weiteren möchte ich mich bei meinen Mitarbeitern in der Windkanal-Arbeitsgruppe für ihre Unterstützung und Hilfestellung bedanken, die mir meine Arbeit unendlich erleichterte. Ein ganz besonderer Dank geht an Roland Rocholz, der immer ein offenes Ohr für meine Probleme hatte und der mich mehr als einmal auf den richtigen Weg lenken konnte.

Ein großer Dank geht auch an Herrn Pfeiffer und sein Team in der Feinmechanik-Werkstatt des IUP für die fantastische Umsetzung der Pläne für die Feld-RSSG.

Erklärung: Ich versichere, dass ich diese Arbeit selbstständig verfasst habe und keine anderen als die angegebenen Quellen und Hilfsmittel benutzt habe.

Heidelberg, den 15. Juni 2010 .....

(Daniel Kiefhaber)